HOLCOMBE DEPARTMENT OF ELECTRICAL AND COMPUTER

ENGINEERING

CLEMSON UNIVERSITY

CLEMSON, SC 29634-0915

PROPAGATION THROUGH WIRE-LOADED CASCADED RECTANGULAR CAVITIES CONNECTED BY NARROW SLOTS

A technical report by

Anthony Q. Martin and Vivek Ramani
Holcombe Department of Electrical and Computer Engineering
Clemson University
Clemson, SC 29634-0915

For

U.S. Department of Defense

Under MURI Grant F49620-01-1-0436 from the U.S. Air Force Office of Scientific

Research

Report Documentation Page

Form Approved
OMB No. 0704-0188

1. REPORT DATE	2. REPORT TYPE	3. DATES COVERED
2004	**N/A**	**-**

4. TITLE AND SUBTITLE	5a. CONTRACT NUMBER
Propagation Through Wire-Loaded Cascaded Rectangular Cavities Connected	5b. GRANT NUMBER
	5c. PROGRAM ELEMENT NUMBER
6. AUTHOR(S)	5d. PROJECT NUMBER
	5e. TASK NUMBER
	5f. WORK UNIT NUMBER
7. PERFORMING ORGANIZATION NAME(S) AND ADDRESS(ES) **Holcombe Department Of Electrical And Computer Engineering Clemson University Clemson, SC 29634-0195**	8. PERFORMING ORGANIZATION REPORT NUMBER
9. SPONSORING/MONITORING AGENCY NAME(S) AND ADDRESS(ES)	10. SPONSOR/MONITOR'S ACRONYM(S)
	11. SPONSOR/MONITOR'S REPORT NUMBER(S)

12. DISTRIBUTION/AVAILABILITY STATEMENT
Approved for public release, distribution unlimited

13. SUPPLEMENTARY NOTES
The original document contains color images.

14. ABSTRACT

15. SUBJECT TERMS

16. SECURITY CLASSIFICATION OF:			17. LIMITATION OF ABSTRACT	18. NUMBER OF PAGES	19a. NAME OF RESPONSIBLE PERSON
a. REPORT	b. ABSTRACT	c. THIS PAGE			
unclassified	**unclassified**	**unclassified**	**UU**	**116**	

ABSTRACT

A theoretical and experimental study of signal propagation through a series of cascaded rectangular cavities connected by walls containing narrow slots and with thin-wire probes/posts inside the cavities is presented. Coupled integral equations are formulated in terms of the electric current on the probes and the equivalent magnetic current in the slots and a numerical solution technique based on the moment method is used to solve them.

The Ewald method is employed to accelerate the convergence of the free-space periodic Green's function appearing in the kernel of the integral equations. The Ewald splitting parameter is determined using a special method (D. Jackson, private communication) which allows for good accuracy in the summations over a wide band of frequencies. The need to further speed up the computation led to the usage of matrix interpolation techniques wherein matrix elements are computed by direct means at only a few frequencies and then interpolated at many interior frequencies. Numerical results for the input impedance of the probe and shielding effectiveness are presented for various values of cavity parameters.

The shielding effectiveness, a means of determining the influence of the transmission path (and environment) on the shape and magnitude of a transient exciting signal, is evaluated. It is hoped that this study will shed additional light on how the transmission path affects the characteristics of a signal which enters a complex electronic environment and reaches an interior point deep inside where a digital circuit may be located.

TABLE OF CONTENTS

Page

Table of Contents (Continued)

LIST OF FIGURES

List of Figures (Continued)

Figure Page

List of Figures (Continued)

Figure Page

List of Figures (Continued)

Figure Page

List of Figures (Continued)

Figure Page

List of Figures (Continued)

Figure Page

CHAPTER 2

ANALYSIS OF SLOT-COUPLED CASCADED RECTANGULAR CAVITIES

Coupled integral equations and a numerical solution technique based on the moment method for slot-coupled cascaded rectangular cavities are presented in this chapter. The cascaded rectangular cavities have thin-wire probes/posts present in them. Free-space periodic Green's functions are derived for the equivalent magnetic current in the slot and the electric current on the probe for a single rectangular PEC cavity. The integral equations for an arbitrary number of slot-coupled cascaded rectangular cavities are then developed as a general case.

1. INTRODUCTION

The two methods that are commonly used for electromagnetic analysis are the mode-theory formulation [1, 2] and the image-theory formulation [3], with the latter being employed in this work. The free-space periodic Green's function appearing in the kernel of the integral equations is obtained from the summation of the elements derived from image-theory analysis. The structure of primary interest is a series of slot-coupled cascaded rectangular cavities with an arbitrary number of sections that contain thin-wire probes/posts and which are flanked by infinite PEC screens at both ends. In general, a plane-wave or a current excitation may be used to excite the narrow slots, or a voltage

source may be used to excite the probes in the cavities. The analysis of this structure requires the solution of coupled integral equations which include the free space periodic Green's function as part of their kernels. The coupled integral equations are solved by the method of moments [4].

2. Analysis Of A Single Rectangular Cavity

To analyze the structure shown in Fig. 2-3 for the dipole excitation, one must first derive the Green's function for an $\hat{x}-$directed magnetic dipole and a $\hat{y}-$directed electric dipole in a rectangular PEC cavity of width $2a$, height $2b$, and depth c. The geometry for this structure is shown in Fig. 2-1.

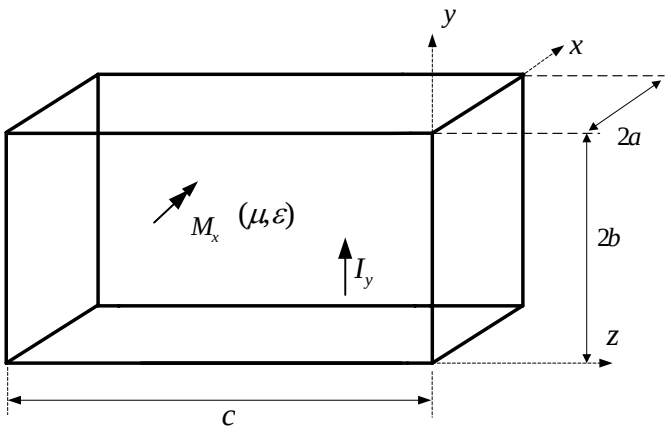

Fig 2-1. An $\hat{x}-$directed unity strength magnetic dipole and a $\hat{y}-$directed unity strength electric dipole inside a rectangular PEC cavity.

The electric vector potential Green's function for the $\hat{x}-$directed magnetic dipole located at a point (x', y', z') inside the cavity must satisfy the differential equation

$$(\nabla^2 + \beta^2)G_x(x, y, z) = -\varepsilon\,\delta(x - x')\delta(y - y')\delta(z - z')\,, \tag{2.1}$$

where

$$\beta = \omega\sqrt{\mu\varepsilon} \tag{2.2}$$

and the medium inside the cavity is characterized by (μ, ε). The boundary conditions on the cavity walls are

$$\frac{\partial}{\partial y} G_x(x, y, z) = 0 \qquad \text{for} \qquad x = \pm a, \tag{2.3}$$

$$\frac{\partial}{\partial y} G_x(x, y, z) = 0 \qquad \text{for} \qquad y = \pm b \tag{2.4}$$

and

$$\frac{\partial}{\partial z} G_x(x, y, z) = 0 \qquad \text{for} \qquad z = 0 \text{ and } z = c. \tag{2.5}$$

In the image-theory formulation [3, 5] the source is first imaged across the cavity walls as shown in Fig. 2-2. The rectangle shown in the figure with the dashed lines represents one unit cell and determines the periodicity of the structure in the x and y directions. The magnetic dipole shown in the rectangle with solid lines is the original dipole which is imaged along the x and y directions repeatedly to obtain the periodicity seen in the figure. The Green's function, which satisfies the differential equation given in (2.1), the boundary conditions given in (2.3), (2.4) and (2.5), and the radiation condition, can be obtained by summing the free-space Green's function for each dipole. The free space periodic Green's function for an $\hat{x}-$directed magnetic dipole located at a point (x', y', z') in a medium characterized by (μ, ε) is given as

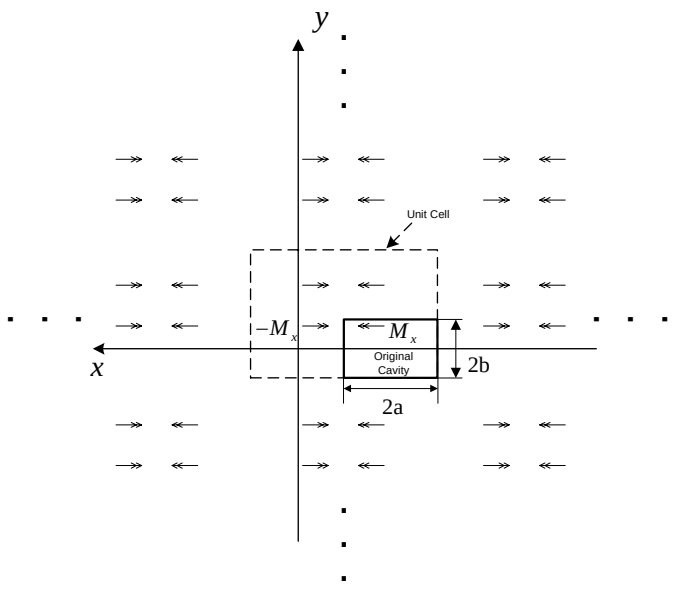

Fig. 2-2. Images of an $\hat{x}$ – directed magnetic dipole inside a rectangular PEC cavity.

$$G_x = \varepsilon \frac{e^{-j\beta R}}{4\pi R}, \tag{2.6}$$

where

$$R = \sqrt{(x-x')^2 + (y-y')^2 + (z-z')^2} \quad . \tag{2.7}$$

Thus, if all the contributions are counted, the image-theory Green's function for an $\hat{x}$ – directed magnetic dipole inside a rectangular PEC cavity is

$$G_x = \frac{\varepsilon}{4\pi} \sum_{m,n,p=-\infty}^{\infty} \left\{ \left(\frac{e^{-j\beta R_{mnp1}}}{R_{mnp1}} - \frac{e^{-j\beta R_{mnp2}}}{R_{mnp2}} - \frac{e^{-j\beta R_{mnp3}}}{R_{mnp3}} + \frac{e^{-j\beta R_{mnp4}}}{R_{mnp4}} \right) + \left(\frac{e^{-j\beta R_{mnp5}}}{R_{mnp5}} - \frac{e^{-j\beta R_{mnp6}}}{R_{mnp6}} - \frac{e^{-j\beta R_{mnp7}}}{R_{mnp7}} + \frac{e^{-j\beta R_{mnp8}}}{R_{mnp8}} \right) \right\}, \tag{2.8}$$

where the 8 contributions are a result of 8 magnetic dipoles in one unit cell as shown in Fig 2-4. The different signs on the contributions are due to the $\hat{x}$-directed and the $-\hat{x}$-directed magnetic dipoles, as shown in Fig. 2-2. Also,

$$R_{mnpi} = \sqrt{\left(\xi_i - mD_x\right)^2 + \left(\eta_i - nD_y\right)^2 + \left(\zeta_i - pD_z\right)^2}, \qquad i = 1, \ldots, 8 \tag{2.9}$$

and the terms ξ_i, η_i, and ζ_i are

$$\xi_1 = \xi_4 = \xi_5 = \xi_8 = x - x', \tag{2.10}$$

$$\xi_2 = \xi_3 = \xi_6 = \xi_7 = x + x' - 2a, \tag{2.11}$$

$$\eta_1 = \eta_2 = \eta_5 = \eta_6 = y - y', \tag{2.12}$$

$$\eta_3 = \eta_4 = \eta_7 = \eta_8 = y + y' - 2b, \tag{2.13}$$

$$\zeta_1 = \zeta_2 = \zeta_3 = \zeta_4 = z - z', \tag{2.14}$$

$$\zeta_5 = \zeta_6 = \zeta_7 = \zeta_8 = z + z' - 2c, \tag{2.15}$$

and D_x, D_y, and D_z are given by

$$D_x = 4a, \; D_y = 8b \text{ and } D_z = 4c. \tag{2.16}$$

The terms D_x, D_y, and D_z represent the periodicity of the structure in the x, y and z

directions, respectively. Similarly, the image-theory Green's function for a $\hat{y}-$directed electric dipole located at a point (x', y', z') inside a rectangular PEC cavity is written as

$$G_y(r,r') = \sum_{m,n,p=-\infty}^{\infty} \left\{ \left(\frac{e^{-j\beta R_{mnp1}}}{R_{mnp1}} - \frac{e^{-j\beta R_{mnp2}}}{R_{mnp2}} - \frac{e^{-j\beta R_{mnp3}}}{R_{mnp3}} + \frac{e^{-j\beta R_{mnp4}}}{R_{mnp4}} \right) - \left(\frac{e^{-j\beta R_{mnp5}}}{R_{mnp5}} - \frac{e^{-j\beta R_{mnp6}}}{R_{mnp6}} - \frac{e^{-j\beta R_{mnp7}}}{R_{mnp7}} + \frac{e^{-j\beta R_{mnp8}}}{R_{mnp8}} \right) \right\}, \tag{2.17}$$

where the terms have their usual meanings and the 8 contributions are a result of 8 electric dipoles in one unit cell as shown in Fig 2-4.

In Fig. 2-3(a), the structure under examination is a rectangular PEC cavity between two infinite PEC screens with narrow slots in them. Inside the cavity is a thin-wire probe which may connect via a 50Ω coaxial cable to a signal source having an internal impedance of 50Ω. The side view of the structure is illustrated in Fig. 2-3(b). As seen from the figure, the length of the thin-wire probe is h and its radius is r. The probe axis is located in the yz plane with d representing its displacement from the $z=0$ plane. The slots are centered on each face of the rectangular cavity and their lengths are $2L_1$ and $2L_2$, respectively, with their widths being $2w$. The width, height, and depth of the cavity shown in the figure is $2a$, $2b$ and c, respectively. The medium inside, in the left half-space where $z<0$, and in the right half-space where $z>c$, is characterized by (μ, ε).

The complete 3D unit cell due to imaging is shown in Fig. 2-4. In the figure, the cavity shown with solid lines is the original rectangular cavity and the cavities shown with dashed lines represent the image cavities. The electric current on the probe and the

magnetic current in the slot are imaged simultaneously. The resulting unit cell has 8 magnetic dipoles, as shown in Fig. 2-4, due to the images of slot current M_{x1} on the cavity wall. The images of the slot current on cavity wall 2, designated as M_{x2}, contribute to 4 magnetic dipoles in the unit cell. The current I_y on the probe has 8 contributions in the unit cell. A rectangular cavity with 2 narrow slots is pictured in Fig. 2-3 to show the presence of 8 magnetic dipoles due to wall 1 and 4 due to wall 2 in the same unit cell. The Green's function for an $\hat{x}-$ directed magnetic dipole on slot 2 inside a rectangular PEC cavity is presented in the next section.

The xy and xz plane imaging is shown in Fig. 2-5 for a single cavity which can be generalized to an arbitrary number of cascaded rectangular cavities. The rectangle in darker solid lines represents the original cavity and it is imaged about the xy and the xz planes successively.

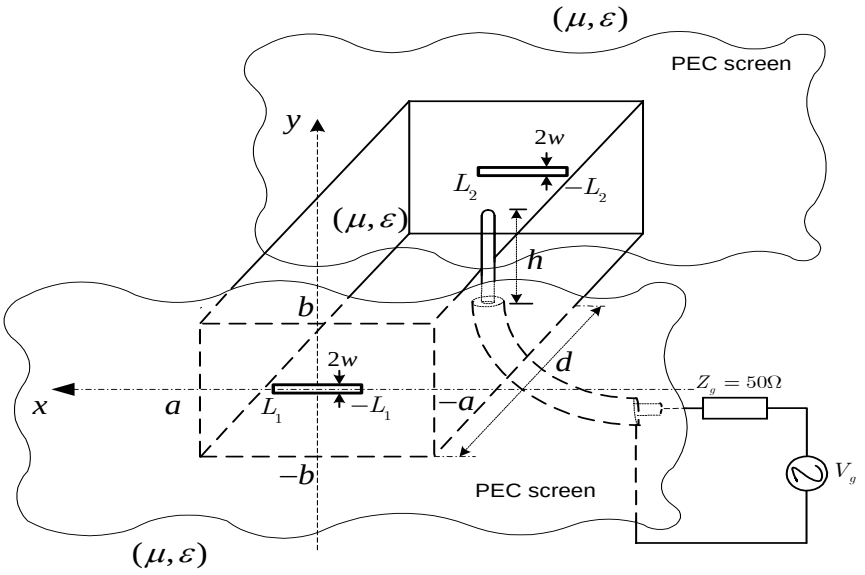

(a)

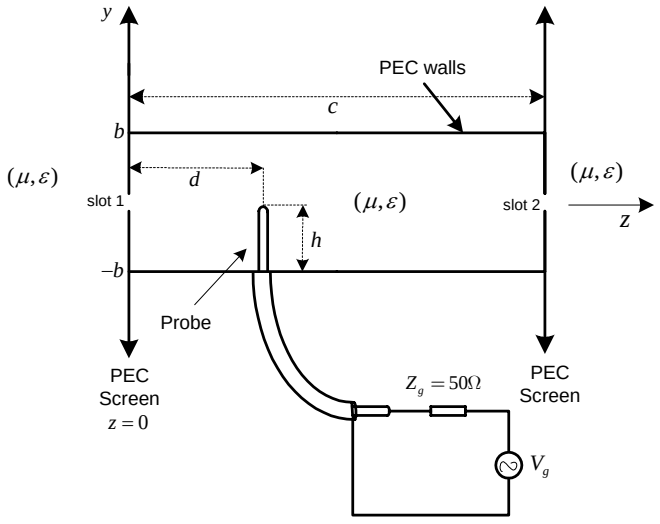

(b)

Fig. 2-3. A rectangular PEC cavity between two infinite PEC screens with narrow slots in them and with a thin-wire probe inside. (a) perspective view (b) side view

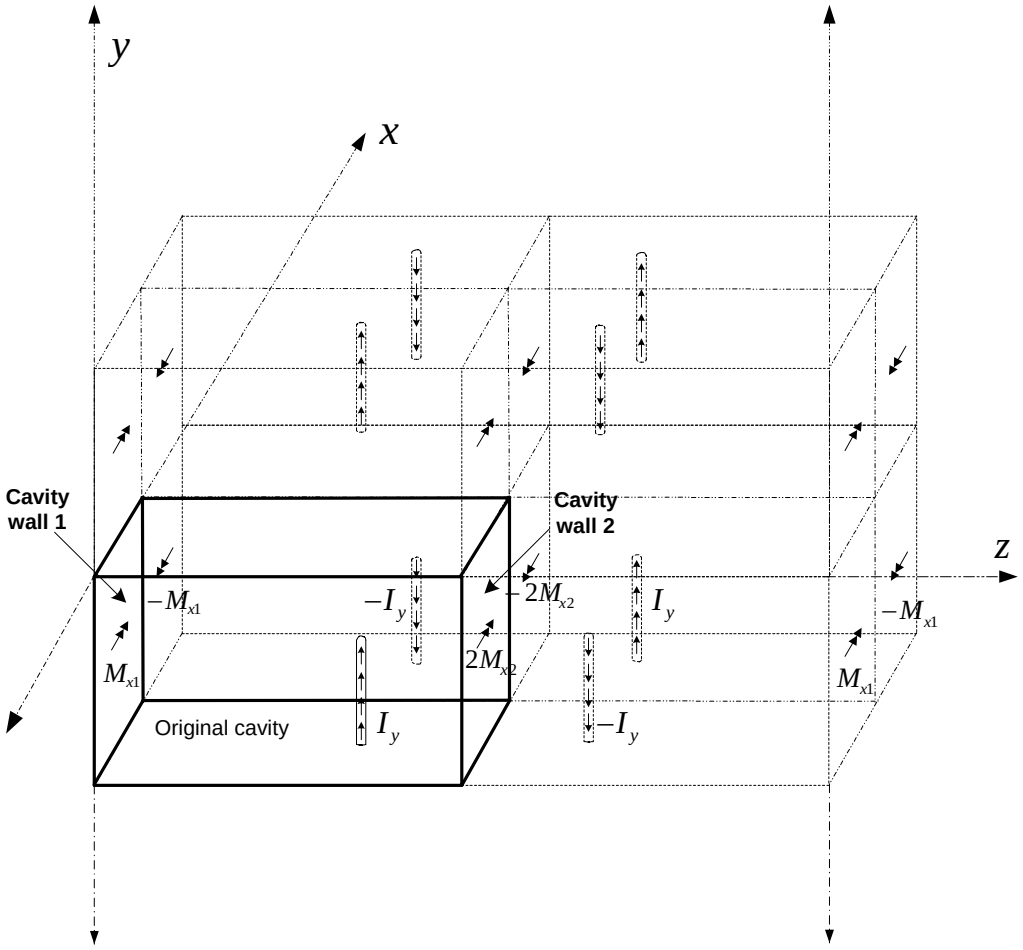

Fig. 2-4. Complete 3D unit cell of a rectangular PEC cavity with two slots and one probe.

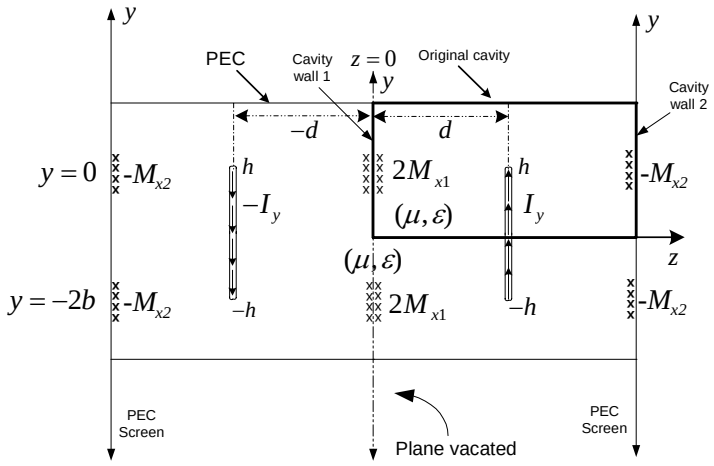

Fig. 2-5. Equivalent model for interior region with imaging about *xy* and *xz* planes (single rectangular PEC cavity with two slots and one probe) - side view

3. ARBITRARY NUMBER OF SLOT-COUPLED CASCADED RECTANGULAR CAVITIES

A general case of an arbitrary number J of slot-coupled cascaded rectangular cavities is pictured in Fig. 2-6. Each cavity has a thin-wire probe/post in it and any probe can be connected via a 50Ω coaxial cable to a signal source having an internal impedance of 50Ω. The last rectangular section is the J^{th} cavity and the sections between the first and the last rectangular cavity are denoted by j. The width, height, and depth of each cavity shown in the figure is $2a$, $2b$ and c, respectively. The length of the j^{th} thin-wire probe is h_j and its radius is r. The probe axes are located in the yz plane with d_1, …, $(j-1)*c+d_j$, ..., $(J-1)*c+d_J$ representing their displacements from the $z=0$ plane. The length of the j^{th} slot is $2L_j$ and its width is $2w$. The medium inside each cavity, in the left half-space where $z<0$, and in the right half-space where $z>(J*c)$ is characterized by (μ,ε).

The procedure followed in the previous section is utilized again and the general problem of an arbitrary number of slot-coupled cascaded rectangular cavities is broken down into single cavities. The treatment is essentially the same and the unit cell obtained due to image theory in Fig. 2-4 is used separately for each cavity. The procedure by which one may derive the coupled integral equations for a thin-wire behind an infinite PEC screen is discussed in [5]. In [3], Kustepeli describes the coupled integral equations for a narrow slot in an infinite PEC screen backed by a single rectangular PEC cavity with a thin-wire probe inside it.

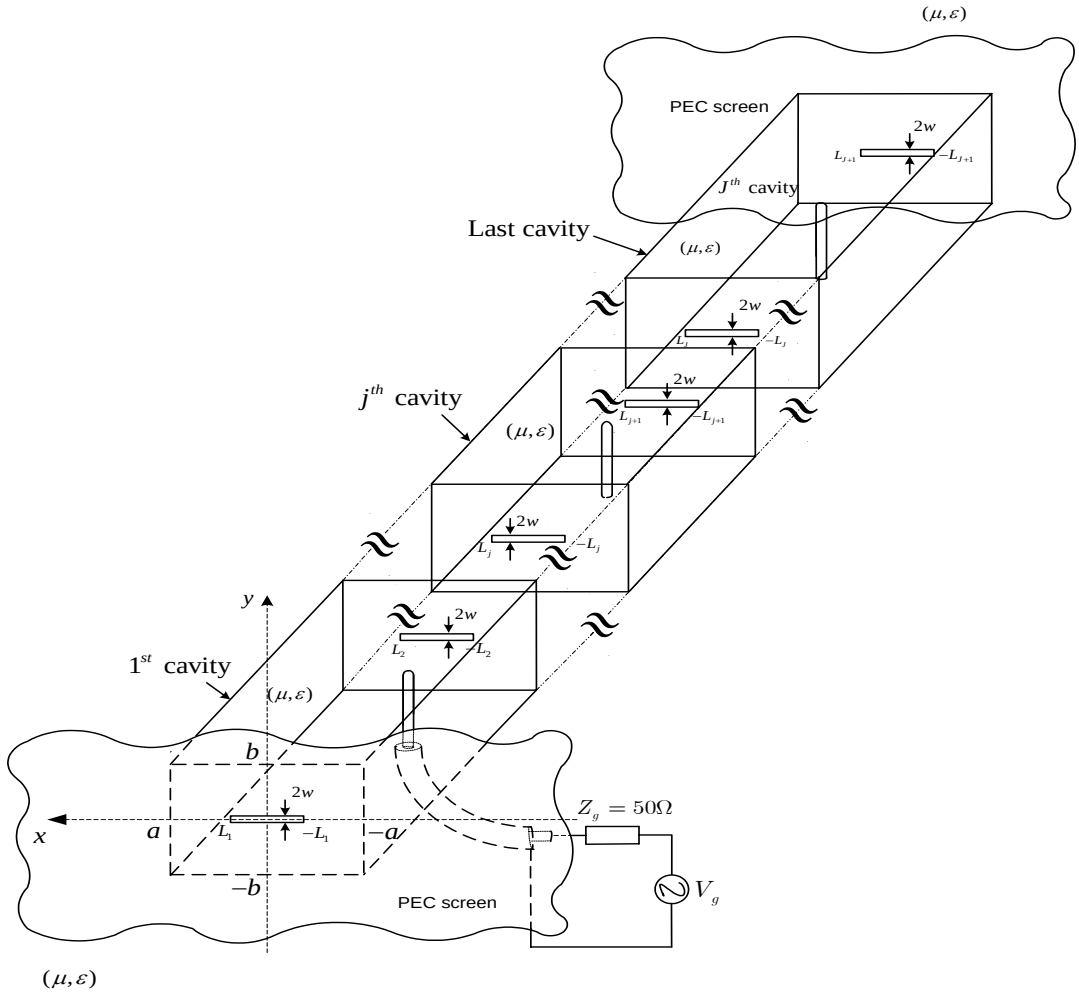

(a)

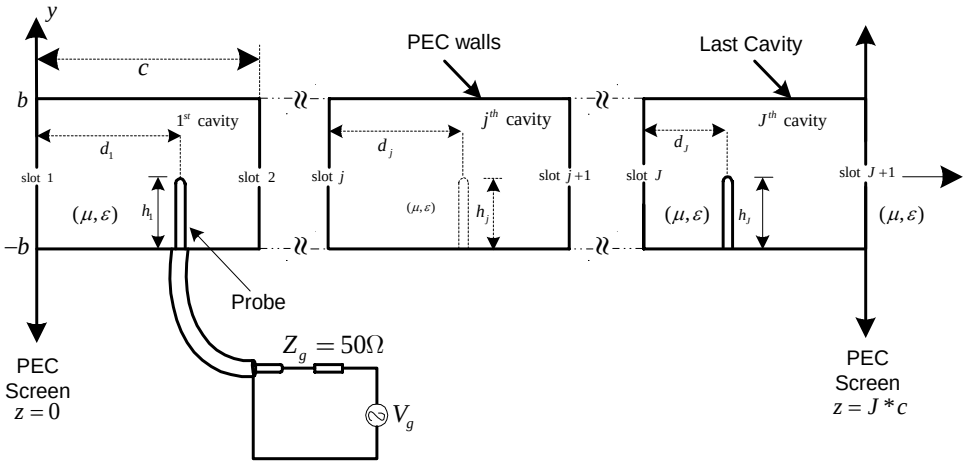

(b)

Fig. 2-6. Arbitrary number of slot-coupled cascaded rectangular cavities with thin-wire probes in them – (a) perspective view. (b) side view.

The formulation discussed in [3] has been extended in this work to an arbitrary number of slot-coupled cascaded rectangular cavities. As an aid in the formulation of the coupled integral equations for the structure of interest, the equivalent models for the interior and exterior regions of the structure are developed. The tangential magnetic field is then forced to be continuous in the apertures and the total tangential electric field on the thin-wire probes in each cavity is made zero. The resulting coupled integral equations derived for the electric current on the probes and the equivalent magnetic current in the slots are presented for the structure shown in Fig. 2-6. The equations (2.18) and (2.21) are the coupled integral equations for slot 1 and slot $J+1$ where the slot has been shorted and a short-circuit magnetic current is placed in its position. Equation (2.20) is the coupled integral equation for slot j where $1<j<J+1$. The total tangential electric field on the thin-wire probes is made zero and the resulting coupled integral equation is listed in (2.19).

$$\frac{1}{j2\pi\omega\mu}\left(\frac{d^2}{dx^2}+\beta^2\right)\int_{x'=-L_1}^{L_1} m_1(x')\{K'_{s_1}(x-x')+K_{cv_1}^{s_1}(x,x')\}dx'$$
$$+\frac{1}{4\pi}\int_{y'=-h_1}^{h_1} I_1(y')G_d^{p_1}(x,y')dy'$$
$$-\frac{1}{j2\pi\omega\mu}\left(\frac{d^2}{dx^2}+\beta^2\right)\int_{x'=-L_2}^{L_2} m_2(x')K_{cv_1}^{s_2}(x,x')dx'$$
$$=-H_{x_1}^{sc},\ \text{on slot 1.} \qquad (2.18)$$

$$\frac{1}{2\pi}\int_{-L_j}^{L_j}\int_{-w}^{w} m_j(x')\frac{1/\pi}{\sqrt{w^2-y'^2}}G_d^{s_j}(y,x',y')dy'dx'$$
$$+\frac{1}{j4\pi\omega\varepsilon}\left(\frac{d^2}{dy^2}+\beta^2\right)\int_{y'=-h_j}^{h_j} I_j(y')K_{cv_j}^{p_j}(y,y')dy'$$
$$-\frac{1}{4\pi}\int_{-L_{j+1}}^{L_{j+1}}\int_{-w}^{w} m_{j+1}(x')\frac{1/\pi}{\sqrt{w^2-y'^2}}G_d^{s_{j+1}}(y,x',y')dy'dx'$$
$$=-V_j\delta(y+b),\ \text{on probe}\ \ j, \qquad j=1,\ ...,\ J. \tag{2.19}$$

$$\frac{1}{j2\pi\omega\mu}\left(\frac{d^2}{dx^2}+\beta^2\right)\int_{x'=-L_{j-1}}^{L_{j-1}} m_{j-1}(x')K_{cv_{j-1}}^{s_{j-1}}(x,x')dx'$$
$$+\frac{1}{4\pi}\int_{y'=-h_{j-1}}^{h_{j-1}} I_{j-1}(y')G_d^{p_{j-1}}(x,y')dy'$$
$$-\frac{1}{j4\pi\omega\mu}\left(\frac{d^2}{dx^2}+\beta^2\right)\int_{x'=-L_j}^{L_j} m_j(x')\left\{K_{cv_{j-1}}^{s_j}(x,x')+2K_{cv_j}^{s_j}(x-x')\right\}dx'$$
$$-\frac{1}{4\pi}\int_{y'=-h_j}^{h_j} I_j(y')G_d^{p_j}(x,y')dy'$$
$$+\frac{1}{j4\pi\omega\mu}\left(\frac{d^2}{dx^2}+\beta^2\right)\int_{x'=-L_{j+1}}^{L_{j+1}} m_{j+1}(x')K_{cv_j}^{s_{j+1}}(x-x')dx'$$
$$=-H_{x_j}^{sc},\ \ \text{on slot}\ j, \qquad j=2,\ ...,\ J. \tag{2.20}$$

$$\frac{1}{j2\pi\omega\mu}\left(\frac{d^2}{dx^2}+\beta^2\right)\int_{x'=-L_{J+1}}^{L_{J+1}} m_{J+1}(x')\{K'_{s_{J+1}}(x-x')+K_{cv_{J+1}}^{s_{J+1}}(x,x')\}dx'$$
$$+\frac{1}{4\pi}\int_{y'=-h_J}^{h_J} I_J(y')G_d^{p_J}(x,y')dy'$$
$$-\frac{1}{j2\pi\omega\mu}\left(\frac{d^2}{dx^2}+\beta^2\right)\int_{x'=-L_J}^{L_J} m_J(x')K_{cv_J}^{s_J}(x,x')dx'$$
$$=-H_{x_{J+1}}^{sc},\ \ \text{on slot}\ \ J+1. \tag{2.21}$$

In equations (2.18-2.21), the axial variation of the magnetic current on slot j is given by $m_j(x)$ and the electric current on the thin-wire probe j is given by $I_j(y)$. In equation (2.19), the voltage at the center of probe j is given by V_j. The delta function, $\delta(y+b)$ in (2.19) specifies that V_j on probe j is located at the $y=-b$ plane. The short-circuit magnetic field, $H^{sc}_{x_j}$ in (2.18), (2.20) and (2.21) is the field at the location of slot j when it is shorted.

The contribution to the kernel due to slot 1, K'_{s_1} in (2.18) is written as

$$K'_{s_1}(x-x') = \frac{1}{2\pi}\int_{-\pi}^{\pi} \frac{e^{-jKR_{s_1}'}}{R_{s_1}'}, \tag{2.22}$$

where

$$R_{s_1}' = \sqrt{(x-x')^2 + 4(\frac{2w}{4})^2 \sin^2\frac{\alpha'}{2}} \tag{2.23}$$

In equation (2.21), $K'_{s_{J+1}}$ is the kernel due to slot $J+1$ and it can be defined like K'_{s_1} in (2.22). The third term of (2.20), $K^{s_j}_{cv_j}$ due to the presence of slot j in cavity j is written as

$$\begin{aligned} K^{s_j}_{cv_j} = & \int_{y'=-w}^{w} \frac{1/\pi}{\sqrt{w^2-y'^2}} (G^{s_j}(x,0,z;x',y',z') \\ & + G^{s_j}(x,0,z;x',-2b+y',z'))dy', \qquad j=1,\ ...,\ J+1. \end{aligned} \tag{2.24}$$

The Green's function $G^{s_j}_d$ in (2.19) is given by

$$G_d^{s_j}(y,x',y') = \frac{\partial}{\partial z} G^{s_j}(0,y,z;x',y',z') + \frac{\partial}{\partial z} G^{s_j}(0,y,z;x',-2b+y',z'), \qquad j=1,\ ...,\ J, \tag{2.25}$$

where G^{s_j} in (2.24) and (2.25) is equivalent to G_x in (2.8). In (2.20) $K_{cv_j}^{s_{j+1}}$ due to the presence of slot $j+1$ in cavity j is written as

$$K_{cv_j}^{s_{j+1}} = \int_{y'=-w}^{w} \frac{1/\pi}{\sqrt{w^2-y'^2}} (G^{s_{j+1}}(x,0,z;x',y',j*c) + G^{s_{j+1}}(x,0,z;x',-2b+y',j*c) + G^{s_{j+1}}(x,0,z;x',y',-j*c) + G^{s_{j+1}}(x,0,z;x',-2b+y',-j*c))dy', \quad j=1,\ ...,\ J, \tag{2.26}$$

and $G_d^{s_{j+1}}$ in (2.19) is written as

$$G^{s_{j+1}}(y,x',y') = \frac{\partial}{\partial z} G^{s_{j+1}}(0,y,z;x',y',j*c) + \frac{\partial}{\partial z} G^{s_{j+1}}(0,y,z;x',-2b+y',j*c) + \frac{\partial}{\partial z} G^{s_{j+1}}(0,y,z;x',y',-j*c) + \frac{\partial}{\partial z} G^{s_{j+1}}(0,y,z;x',-2b+y',-j*c), \quad j=1,\ ...,\ J. \tag{2.27}$$

In (2.26) and (2.27), $G^{s_{j+1}}$ is the image-theory Green's function for an $\hat{x}-$directed magnetic dipole inside a rectangular PEC cavity and is written as

$$G^{s_{j+1}}(r;r') = \sum_{m,n,p=-\infty}^{\infty} \left[\left(\frac{e^{-j\beta R_{mnp1b}}}{R_{mnp1b}} - \frac{e^{-j\beta R_{mnp2b}}}{R_{mnp2b}} - \frac{e^{-j\beta R_{mnp3b}}}{R_{mnp3b}} + \frac{e^{-j\beta R_{mnp4b}}}{R_{mnp4b}} \right) \right], \tag{2.28}$$

where the 4 contributions are as a result of 4 magnetic dipoles in one unit cell as shown in Fig 2-4 for the magnetic current on slot 2 and

$$R_{mnpib} = \sqrt{\left(\xi_{ib} - mD_x\right)^2 + \left(\eta_{ib} - nD_y\right)^2 + \left(\zeta_{ib} - pD_z\right)^2}, \qquad i=1,2,3,4. \tag{2.29}$$

where D_x, D_y, and D_z are defined in (2.16) and

$$\xi_{1b} = \xi_{4b} = x - x', \tag{2.30}$$

$$\xi_{2b} = \xi_{3b} = x + x' - 2a, \tag{2.31}$$

$$\eta_{1b} = \eta_{2b} = y - y', \tag{2.32}$$

$$\eta_{3b} = \eta_{4b} = y + y' - 2b, \tag{2.33}$$

and

$$\zeta_{1b} = \zeta_{2b} = \zeta_{3b} = \zeta_{4b} = z - z'. \tag{2.34}$$

The kernel due to the presence of the probe inside the cavity, $K_{cv_j}^{p_j}$, is written as

$$K_{cv_j}^{p_j}(y, y') = \frac{1}{2\pi}\int_{-\pi}^{\pi}(G^{p_j}(r, y, d_j; r\cos\phi, -b + y', d_j + r\sin\phi)$$
$$-G^{p_j}(r, y, d_j; r\cos\phi, -b + y', -d_j + r\sin\phi))d\phi, \qquad j = 1, \ ..., \ J, \tag{2.35}$$

and $G_d^{p_j}$ in (2.18) and (2.20) is written as

$$G_d^{p_j}(x, y') = \frac{\partial}{\partial z}G^{p_j}(x, o, z; 0, -b + y', d_j)$$
$$-\frac{\partial}{\partial z}G^{p_j}(x, o, z; 0, -b + y', -d_j), \qquad j = 1, \ ..., \ J. \tag{2.36}$$

In (2.35) and (2.36), G^{p_j} is the image-theory Green's function for a $\hat{y}-$directed electric dipole inside a rectangular PEC cavity and is similar to G_y in (2.17).

4. NUMERICAL SOLUTION

The coupled integral equations given in (2.18-2.21) are solved by the method of moments [4]. In this method the unknown magnetic currents $m_j(x)$ and the unknown electric currents $I_j(y)$ are expanded in terms of the pulse basis functions, each weighted by unknown coefficients m_{n_j} and i_{n_j}, respectively. The triangle functions are used for testing. Detailed information about expansion and testing procedures is given in [4, 7]. The resulting matrix equation is written as

$$\begin{bmatrix}
Y_{mn_1} & Y_{mn_{2,1}} & \cdots & 0 & 0 & 0 & \cdots & 0 & 0 & C_{mn}^{s_1p_1} & \cdots & 0 & \cdots & 0 \\
Y_{mn_{1,2}} & Y_{mn_2} & \cdots & 0 & 0 & 0 & \cdots & 0 & 0 & C_{mn}^{s_2p_1} & \cdots & 0 & \cdots & 0 \\
\vdots & \vdots & \vdots & \vdots & \vdots & \vdots & \vdots & \vdots & \vdots & \vdots & \vdots & \vdots & \vdots & \vdots \\
0 & 0 & \cdots & Y_{mn_{j-1}} & Y_{mn_{j,j-1}} & 0 & \cdots & 0 & 0 & 0 & \cdots C_{mn}^{s_{j-1}p_j} & \cdots & 0 \\
0 & 0 & \cdots & Y_{mn_{j-1,j}} & Y_{mn_j} & Y_{mn_{j+1,j}} & \cdots & 0 & 0 & 0 & \cdots C_{mn}^{s_jp_j} & \cdots & 0 \\
0 & 0 & \cdots & 0 & Y_{mn_{j,j+1}} & Y_{mn_{j+1}} & \cdots & 0 & 0 & 0 & \cdots C_{mn}^{s_{j+1}p_j} & \cdots & 0 \\
\vdots & \vdots & \vdots & \vdots & \vdots & \vdots & \vdots & \vdots & \vdots & \vdots & \vdots & \vdots & \vdots & \vdots \\
0 & 0 & \cdots & 0 & 0 & 0 & \cdots & Y_{mn_J} & Y_{mn_{J+1,J}} & 0 & \cdots & 0 & \cdots & C_{mn}^{s_Jp_J} \\
0 & 0 & \cdots & 0 & 0 & 0 & \cdots & Y_{mn_{J,J+1}} & Y_{mn_{J+1}} & 0 & \cdots & 0 & \cdots & C_{mn}^{s_{J+1}p_J} \\
C_{mn}^{p_1s_1} & C_{mn}^{p_1s_2} & \cdots & 0 & 0 & 0 & \cdots & 0 & 0 & Z_{mn}^{p_1} & \cdots & 0 & \cdots & 0 \\
\vdots & \vdots & \vdots & \vdots & \vdots & \vdots & \vdots & \vdots & \vdots & \vdots & \vdots & \vdots & \vdots & \vdots \\
0 & 0 & \cdots & C_{mn}^{p_js_{j-1}} & C_{mn}^{p_js_j} & C_{mn}^{p_js_{j+1}} & \cdots & 0 & 0 & 0 & \cdots & Z_{mn}^{p_j} & \cdots & 0 \\
\vdots & \vdots & \vdots & \vdots & \vdots & \vdots & \vdots & \vdots & \vdots & \vdots & \vdots & \vdots & \vdots & \vdots \\
0 & 0 & \cdots & 0 & 0 & 0 & \cdots & C_{mn}^{p_Js_J} & C_{mn}^{p_Js_{J+1}} & 0 & \cdots & 0 & \cdots & Z_{mn}^{p_J}
\end{bmatrix}
\begin{bmatrix} m_{n_1} \\ m_{n_2} \\ \vdots \\ m_{n_{j-1}} \\ m_{n_j} \\ m_{n_{j+1}} \\ \vdots \\ m_{n_J} \\ m_{n_{J+1}} \\ i_{n_1} \\ \vdots \\ i_{n_j} \\ \vdots \\ i_{n_J} \end{bmatrix}
=
\begin{bmatrix} I_{m_1} \\ I_{m_2} \\ \vdots \\ I_{m_{j-1}} \\ I_{m_j} \\ I_{m_{j+1}} \\ \vdots \\ I_{m_J} \\ I_{m_{J+1}} \\ V_{m_1} \\ \vdots \\ V_{m_j} \\ \vdots \\ V_{m_J} \end{bmatrix}, \quad (2.37)$$

where Y_{mn_i}, $Y_{mn_{i,i+1}}$, and $Y_{mn_{i+1,i}}$ are the admittance terms due to the slots. The elements of the sub-matrices representing coupling from the probe to the narrow slot are given by $C_{mn}^{s_i p_i}$ and $C_{mn}^{p_i s_i}$ represents the slot-to-probe coupling terms. The impedance sub-matrix term for the probe is $Z_{mn}^{p_i}$. The expression for the elements of the admittance sub-matrix Y_{mn_i} is given by

$$Y_{mn_i} = Y_{mn_i}^{s_i} + Y_{mn_i}^{cv_i}, \quad i = 1 \text{ or } J, \tag{2.38}$$

where

$$Y_{mn_i}^{s_i} = \frac{1}{j2\pi\omega\mu\Delta_{s_i}} \int_{x_n-\Delta_{s_i}/2}^{x_n+\Delta_{s_i}/2} \Big\{ K'_{s_i}(x_{m+1} - x') - 2(1-(\beta\Delta_{s_i})^2/2) K'_{s_i}(x_m - x') + K'_{s_i}(x_{m-1} - x') \Big\} dx'. \tag{2.39}$$

In (2.39) x_m and x_n can be determined from

$$x_p = -L_i + p\Delta_{s_i}, \quad p = 1, 2, ..., N \tag{2.40}$$

with p standing for m or n. The sub-domain segment length Δ_{s_i} is given by

$$\Delta_{s_i} = \frac{2L_i}{(N+1)} \tag{2.41}$$

In (2.40) and (2.41), N is the number of basis functions used to approximate the magnetic current in the slot. One can write $Y_{mn_i}^{cv_i}$ as

$$Y_{mn_i}^{cv_i} = \frac{1}{j2\pi\omega\mu\Delta_{s_i}}\left\{S_{m+1,n} - 2(1-(\beta\Delta_{s_i})^2/2)S_{mn} + S_{m-1,n}\right\} \tag{2.42}$$

where

$$S_{mn} = \int_{x_n-\Delta_{s_i}/2}^{x_n+\Delta_{s_i}/2} K_{cv_i}^{s_i}(x_m, x')dx'. \tag{2.43}$$

The expression for the elements of the admittance sub-matrix $Y_{mn_{i+1,i}}$ is given by

$$Y_{mn_{i+1,i}} = Y_{mn_{i+1}}^{cv_i}, \quad i = 1, \ldots, J, \tag{2.44}$$

where $Y_{mn_{i+1}}^{cv_i}$ and elements of the sub-matrix $Y_{mn_{i,i+1}}$ appearing in (2.37) are defined like $Y_{mn_i}^{cv_i}$ of (2.42).

In (2.37), the elements of the sub-matrix $C_{mn}^{s_i p_i}$ representing the coupling from the probe to the slot is given by

$$C_{mn}^{s_i p_i} = \frac{1}{4\pi}\int_{x_m-\Delta_{s_i}/2}^{x_m+\Delta_{s_i}/2}\int_{y_n-\Delta_{w_i}/2}^{y_n+\Delta_{w_i}/2} G_d^{p_i}(x, y')dy'dx, \qquad i = 1, \ldots, J, \tag{2.45}$$

and

$$y_n = -h_i + n\Delta_{w_i}, \quad n = 1, 2, \ldots, P. \tag{2.46}$$

The width of a pulse basis function used to expand the electric current on the probe is defined as

$$\Delta_{w_i} = \frac{2h_i}{(P+1)} \tag{2.47}$$

where P in (2.46) and (2.47) is the number of unknowns used to expand the current. The elements of the sub-matrix $C_{mn}^{s_{i+1}p_i}$ are defined like $C_{mn}^{s_i p_i}$ in (2.45).

In (2.37), the elements of the impedance sub-matrix $Z_{mn}^{p_i}$ is written as

$$Z_{mn}^{p_i} = \frac{1}{j4\pi\omega\varepsilon\Delta_{w_i}}\left\{T_{m+1,n} - 2(1-(\beta\Delta_{w_i})^2)T_{mn} + T_{m-1,n}\right\}, \quad i = 1, \ ..., \ J, \tag{2.48}$$

where

$$T_{mn} = \int_{y_n-\Delta_{w_i}/2}^{y_n+\Delta_{w_i}/2} K_{cv_i}^{p_i}(y, y')dy'. \tag{2.49}$$

The expression for the elements of the sub-matrix $C_{mn}^{p_i s_i}$ appearing in (2.37) representing the coupling from the slot to the probe is given by

$$C_{mn}^{p_i s_i} = \frac{1}{2\pi}\int_{y_m-\Delta_{w_i}/2}^{y_m+\Delta_{w_i}/2}\int_{x_n-\Delta_{w_i}/2}^{x_n+\Delta_{w_i}/2}\int_{-w}^{w}\frac{1/\pi}{\sqrt{w^2-y'^2}}G_d^{s_i}(y, x', y')dy'dx'dy, \qquad i = 1, \ ..., \ J. \tag{2.50}$$

The elements of the sub-matrix $C_{mn}^{p_i s_{i+1}}$ are defined like $C_{mn}^{p_i s_i}$ in (2.50).

Finally, the elements of the excitation vector in (2.37) are given by

$$V_{m_i} = \begin{cases} -V, & m = P*(i+J) + \dfrac{P+1}{2} \\ 0, & \textit{otherwise.} \end{cases} \tag{2.51}$$

For plane-wave excitation of the slot, the term I_{m_i} of (2.37) is given by

$$I_{m_i} \cong \Delta_{s_i} H_{x_i}^{sc}(x_m), \quad m = (i-1)*P \; + \; (1, \; ..., \; P) \tag{2.52}$$

The approximation [5] employed in (2.52) is a very good one, provided $H_{x_i}^{sc}$ does not vary rapidly over an interval of $2\Delta_{s_i}$.

5. CONCLUSIONS

In this chapter coupled integral equations and a numerical solution technique based on the moment method for slot-coupled cascaded rectangular cavities are presented. Free-space periodic Green's functions for a magnetic dipole and an electric dipole in a rectangular PEC cavity are derived and coupled integral equations for an arbitrary number of slot-coupled cascaded rectangular cavities are then presented as a general case. In this chapter, a general solution is described as a precursor to a numerical solution for single, double, and triply cascaded rectangular cavities which are discussed in detail in Chapter 5.

REFERENCES

[1] C. L. Freeman, "Analysis and Design of Stripline-Fed Slot Antennas," Clemson University, Dissertation, May 1996.

[2] S. Hashemi-Yeganeh and C. Brichter, "Theoretical and Experimental Studies of Cavity-Backed Slot Antenna Excited by a Narrow Strip," *IEEE Trans. Antennas Propagat.*, vol. 41, pp. 236-241, February 1993.

[3] A. Kustepeli, "Analysis and Implementation of the Ewald Method for Waveguide and Cavity Structures," Clemson University, Dissertation, December 1999.

[4] R. F. Harrington, Field Computation by Moment Methods (MacMillan, New York, 1968).

[5] C. M. Butler and K. R. Umashankar, “Electromagnetic Excitation of a Wire Through an Aperture-Perforated Conducting Screen,” *IEEE Trans. Antennas Propagat.*, vol. 24, pp. 456-462, July 1976.

[6] A. Kustepeli and A. Q. Martin, “Fields and Currents due to a Modulated Laser Beam Exciting an Array of Narrow Slots,” *in Proc., IEEE Antennas Propagat. Soc. Int. Symp.*, Montreal, Canada, July 1997, pp. 1240-1243.

[7] D. R. Wilton and C. M. Butler, “Effective Methods for Solving Integral and Integro-Differential Equations,” Electromagnetics, vol. 1, pp. 289-308, July-Sept. 1981.

CHAPTER 3

EWALD METHOD AND DETERMINATION OF SPLITTING PARAMETER

The free-space periodic Green's function appears as the kernel of the integral equations formulated for slot-coupled cascaded rectangular cavities. The Ewald method [1, 2] can be used to efficiently accelerate the convergence of the infinite series encountered in the calculation of matrix elements obtained by employing the method of moments for the numerical solution of the integral equations. In this method, the free-space periodic Green's function is expressed as the sum of "spectral" and "spatial" series. Each of these series possesses Gaussian decay, leading to a series representation that typically has a very fast convergence rate. The spectral and spatial series are written in terms of the complementary error function, involving a splitting parameter E. The method of determining the splitting parameter and numerical results for the different choices of the splitting parameter are presented in this chapter.

1. INTRODUCTION

The Ewald method was first developed and used in 1921 by P.P. Ewald [1] to evaluate the summations occurring in crystal lattice theory. In the evaluation of the free-space periodic Green's function for two-dimensional and three-dimensional cases with the Ewald method, the spectral and the spatial series, which are written in terms of the

complementary error function, involve a splitting parameter E. In [9] it is stated that E is an arbitrary number with an optimum value, E_{opt}, given to balance the convergence rate between these two series, thereby minimizing the total number of terms needed for the calculation. If E is increased beyond E_{opt}, then successive terms in the spatial series decay faster while successive terms in the spectral series decay more slowly. In studies involving the Ewald method [9, 11], the E_{opt} value is generally used to sum the spectral and the spatial series arising in the analysis of structures having small periodic spacing. Although it is stated in [9] that the splitting parameter is arbitrary, in [8], Kustepeli and Martin have shown that one cannot get correct results even when $E = E_{opt}$ for structures having large periodic spacing. Therefore, the splitting parameter should always be chosen carefully.

One can apply the Ewald method in calculating the free-space periodic Green's function due to three-dimensional periodic arrays [1]. For the three-dimensional case in [10], the value of E used in the computations is determined by examining only the convergence of the spatial series. For two-dimensional arrays, the choice of this parameter is very important as in the three-dimensional case, to balance the convergence rate in the analysis of structures with small periodic spacing and to obtain correct values in the analysis of structures having large periodic spacing. One can also use the Ewald method for the three-dimensional case after applying image-theory to the structure.

2. Determination of Splitting Parameter

In [8], Kustepeli and Martin present an expression for E_{opt} which can be used in the calculation of free-space periodic Green's function for the three-dimensional case

having small periodic spacing. Results obtained by the Ewald method are compared with those obtained by the well-known Shanks' transform [4, 5] computed using Wynn's ε-algorithm [6]. One of the most effective means for evaluating the Green's function given in (2.6) of the previous chapter is the Ewald Method [1]. In this method, the Green's function is expressed as the summation of two series such that

$$G = G_1 + G_2 \ . \tag{3.1}$$

In (3.1), G_1 and G_2 utilize the complementary error function, $erfc(z)$. By virtue of the presence of the complementary error function in these series, a very rapid convergence rate, resulting from the Gaussian decay found in the terms, is achieved. Since Gaussian decay is involved in each, the value of the summation is generally obtained in a very small number of terms if E is properly chosen. For the three-dimensional case, the Green's function in (2.6) is expressed as a sum of two series as given in (3.1). The spectral series G_1 is written as [3, 8]

$$G_1 = \frac{1}{4D_xD_yD_z} \sum_{m,n,p=-\infty}^{\infty} e^{-j2\pi\left(\frac{m\xi}{D_x}+\frac{n\eta}{D_y}+\frac{p\zeta}{D_z}\right)} \frac{e^{-\alpha_{mnp}^2/E^2}}{\alpha_{mnp}^2} \ , \tag{3.2}$$

where

$$\alpha_{mnp}^2 = \left(\frac{m\pi}{D_x}\right)^2 + \left(\frac{n\pi}{D_y}\right)^2 + \left(\frac{p\pi}{D_z}\right)^2 - \frac{k^2}{4} \tag{3.3}$$

and D_x, D_y and D_z are given in (2.16). The spatial series G_2 is given by [3, 8] as

$$G_2 = \frac{1}{8\pi} \sum_{m,n,p=-\infty}^{\infty} \frac{1}{R_{mnp}} \left[e^{jkR_{mnp}} \, erfc\left(R_{mnp}E + \frac{jk}{2E} \right) + e^{-jkR_{mnp}} \, erfc\left(R_{mnp}E - \frac{jk}{2E} \right) \right], \tag{3.4}$$

which can also be written as

$$G_2 = \frac{1}{4\pi} \sum_{m,n,p=-\infty}^{\infty} \frac{1}{R_{mnp}} \, \mathrm{Re}\left(e^{jkR_{mnp}} \, erfc\left(R_{mnp}E + \frac{jk}{2E} \right) \right), \tag{3.5}$$

where R_{mnp} is defined in (2.9). The optimum splitting parameter [3, 8] used to balance the convergence rates of G_1 and G_2 for the three-dimensional (3D) array is

$$E = \left(\pi^2 \frac{1/D_x^2 + 1/D_y^2 + 1/D_z^2}{D_x^2 + D_y^2 + D_z^2} \right)^{\frac{1}{4}}. \tag{3.6}$$

The complementary error function appearing in the equations (3.4) and (3.5) is given by [3, 8]

$$erfc(z) = 1 - erf(z) = \frac{2}{\sqrt{\pi}} \int_z^{\infty} e^{-t^2} dt \tag{3.7}$$

where $erf(\cdot)$, the error function, is given by

$$erf(z) = \frac{2}{\sqrt{\pi}} \int_0^{z} e^{-t^2} dt \ . \tag{3.8}$$

By using the following relation,

$$erfc(z) = e^{-z^2}\ w(jz)\ , \tag{3.9}$$

the complementary error function appearing in the equations (3.4) and (3.5) is calculated. The function $w(\cdot)$ in (3.9) is utilized to compute the complementary error function for a complex argument. This function, which was first devised and tabulated by Faddeyeva and Terent'ev [12], can be computed using a code written by Poppe and Wijers [13, 14].

The method explained in [8] to determine E / E_{opt} involves a splitting parameter which is said to be dependent on periodic spacing of a structure alone and the choice of which is more or less arbitrary. Jackson suggested a method [7] wherein the splitting parameter is not treated as arbitrary and is said to be dependent on periodic spacing, the number of significant figures lost in the calculation of the Green's function and the frequency.

The "optimum" E parameter, E_{opt}, that results in the same asymptotic rate of decay for G_1 and G_2 is given in (3.6). At high frequencies, one gets very large nearly-equal-in-magnitude numbers of opposite signs for the first several terms of G_1 and G_2. These terms largely cancel one another, resulting in a sum that is of moderate value. However, this cancellation generally results in an apparent convergence to incorrect values and a loss of significant figures. To avoid this problem, one needs to limit the size of the largest terms in both series. Jackson [7] devised a method for choosing E that is larger than the optimum, which solves this problem.

The goal is to limit the size of the largest term relative to that of the overall Green's function. The largest terms in each series come from the $(0,0,0)$ terms. One chooses a limit of

$$|G_{1,000}| \; < \; 10^{d} \, |G| \tag{3.10}$$

and

$$|G_{2,000}| \; < \; 10^{d} \, |G|, \tag{3.11}$$

where G_1 and G_2 have their usual meanings, the subscript (0,0,0) refers to the first term of the series ($m = n = p = 0$) and the parameter "d" indicates the significant figures lost in the calculation of the Green's function. The magnitude of the overall Green's function is approximated as

$$|G| \; \approx \; \frac{1}{4\pi \mathrm{R}_{000}}. \tag{3.12}$$

This approximation is a reasonable one unless the distance between the source and observation points becomes comparable to the distance between the source point and the boundary of the unit cell (so that image terms are important). Even then, the above estimate is probably correct to within an order of magnitude.

In Jackson's method one uses the asymptotic form of the complementary error function (valid at high frequencies) and using (3.10) writes G_1 of (3.2) as

$$\frac{e^{\left(\frac{-\alpha_{000}}{E}\right)^2}}{\alpha_{000}^2}\left(\frac{1}{4D_x D_y D_z}\right) < 10^{d} \, \frac{1}{4\pi R_{000}}. \tag{3.13}$$

One can define

$$x_1 \equiv -\frac{\alpha_{000}}{E}, \tag{3.14}$$

then one gets

$$e^{x_1^2} = c_1, \tag{3.15}$$

where

$$c_1 = 10^d \left[\left(\frac{\alpha_{000}^2 D_x D_y D_z}{\pi R_{000}} \right) \right]. \tag{3.16}$$

An accurate solution to the transcendental equation in (3.15) is given by

$$x_1 = \sqrt{\ln(c_1) + \ln\left(\sqrt{(c_1) + \ln\left(\sqrt{(c_1) + \ln\left(\sqrt{\ln(c_1)} \right)} \right)} \right)}. \tag{3.17}$$

The inequality in (3.13) has to be maintained and hence the restriction that

$$E > -\frac{\alpha_{000}}{x_1}, \tag{3.18}$$

rendering (3.13) true.

The analysis for the G_2 series is similar using Jackson's method. One uses the asymptotic form of the complementary error function (valid at high frequencies) and writes

$$\frac{e^{\left(\frac{k}{2E}\right)^2}}{\sqrt{\pi}\left(\frac{k}{2E}\right)}\left(\frac{2}{8\pi R_{000}}\right) < 10^d \frac{1}{4\pi R_{000}}. \tag{3.19}$$

One can write

$$x_2 \equiv \frac{k}{2E}, \tag{3.20}$$

then (3.19) becomes

$$\frac{e^{x_2^2}}{x_2} = c_2, \tag{3.21}$$

where

$$c_2 = 10^d[\sqrt{\pi}]. \tag{3.22}$$

The solution to the transcendental equation in (3.21) is given by

$$x_2 = \sqrt{\ln(c_2) + \ln\left(\sqrt{(c_2) + \ln\left(\sqrt{(c_2) + \ln\left(\sqrt{\ln(c_2)}\right)}\right)}\right)}. \tag{3.23}$$

The inequality in (3.19) has to be maintained and hence the restriction that

$$E > \frac{k}{2x_2}. \tag{3.24}$$

Jackson's method thus chooses an overall E by comparing (3.6), (3.18) and (3.24) and writing

$$E = \max\left(E_{opt}, \frac{-\alpha_{000}}{x_1}, \frac{k}{2x_2} \right). \tag{3.25}$$

Kustepeli and Martin [8] and Jackson [7] have shown that $E = E_{opt}$ may not be sufficient for large periodic spacing and E has to be increased beyond this value to achieve accurate results. The reason $E \leq E_{opt}$ does not work for larger periodic spacing can be explained as follows. For large arguments the complementary error function behaves as $\exp(-z^2)/z$ which is the reason for using this method for the calculation of the free-space periodic Green's function. For large periodic spacing, E_{opt} given by (3.6) becomes small, and the imaginary part of the argument of $erfc(\cdot)$ becomes large and dominant for the first several terms of the series. As a consequence, $erfc(\cdot)$ becomes very large and, therefore, one gets very large numbers for the first several terms of these series. Similar comments can be made for the series G_1 of (3.2) that includes the Gaussian function directly. Gaussian decay is again achieved for terms with large indices, and the two series G_1 and G_2 converge to very large nearly-equal-in-magnitude numbers of opposite signs. Since the values of the spectral and the spatial sums are very, very large but have opposite signs, accuracy is seriously compromised when adding the sums of the two series because of finite precision. The result is the apparent convergence to incorrect values. By increasing E beyond E_{opt} by a sufficient amount, one obtains small values for the imaginary part of the argument of the complementary error function and small

positive values for $-\alpha_{mnp}^2 / E^2$ in (3.2) for the first several terms of the series. As a result, one avoids the inaccuracy resulting from adding numbers of nearly equal magnitude but of opposite sign, and a correct sum is obtained for G. Thus a value for E is chosen that is the maximum of (3.6), (3.18) and (3.24).

3. RESULTS

The following section compares Jackson's method [7] of determining E with an arbitrary method of determining E and presents comparative results for the same. The geometry chosen for this analysis is shown in Fig. 3-1. As shown in the Fig. 3-1(a), the structure under examination is a narrow slot in an infinite PEC screen backed by a rectangular cavity with a thin-wire probe present inside the cavity. The side view of this structure is illustrated in Fig. 3-1(b). The length of the thin-wire probe is h with its radius specified as r. The probe axis is located in the yz plane with d representing its displacement from the $z = 0$ plane. The slot length is $2L$ and its width is $2w$. The width, height, and depth of the cavity shown in the figure are $2a,\ 2b \text{ and } c$, respectively. The medium inside the cavity and in the left half-space where $z < 0$ is characterized by (μ, ε). The probe is connected via a 50Ω coaxial cable to a signal source having an internal impedance of 50Ω. The structure parameters are shown in Table 3.1.

The real and imaginary parts of the input impedance of the thin-wire probe for the structure given in Table 3.1 in the frequency range between 6 GHz and 12 GHz are shown in Fig. 3-2. In this figure, the measured data from [3] is compared with the numerical results obtained by using Jackson's method and $E = E_{opt}$. The figure shows that the numerical results begin to fail when the frequency is increased while $E = E_{opt}$.

As shown in the figure, the real part of the computed input impedance becomes even negative for some frequencies when $E = E_{opt}$; in addition, the results for the imaginary part are not even in the range of the figure above 10.4 GHz, showing a large error in the computation of these values. Since the value of the splitting parameter is not appropriate for the calculation of the matrix elements, error occurs in the calculation of the probe current and input impedance. The correct values of the matrix elements can be obtained by increasing the splitting parameter by a sufficient amount, which results in the correct values for the probe current and hence the input impedance. As shown in the figure, by using the Jackson's method, one can get very good agreement between the measured [3] and the numerical results. Thus one can conclude from Fig 3-2, the optimum splitting parameter ($E = E_{opt}$) may not be suitable for some structures. Therefore, the splitting parameter should be chosen carefully and one may use Jackson's method to determine the E parameter without the need for guess work or trail and error.

Variation of E / E_{opt} with Jackson's E is smooth in the entire frequency range as shown in Fig. 3-3 compared to the arbitrary usage of $E = E_{opt}$ and $E = 2 * E_{opt}$. The other major consideration for employing Jackson's method was CPU time reduction. CPU times for numerical results obtained by using $E = E_{opt}$ and $E = 2 * E_{opt}$ were compared to results obtained by using Jackson's E. As shown in Fig. 3-4, cumulative computation time is least for $E = E_{opt}$ and it increases as the multiplication factor increases. Also, cumulative CPU time for Jackson's method is between $E = E_{opt}$ and $E = 2 * E_{opt}$ in the frequency range of interest. Thus, Jackson's method is best suited in terms of CPU time and accuracy of results.

TABLE 3.1
STRUCTURE PARAMETERS

Parameter[*]	**Structure A**
Cavity width, $2a$	22.86
Cavity height, $2b$	10.16
Cavity depth, c	41.275
Slot length, $2L$	15.0
Slot width, $2w$	0.5
Probe length, h	6.35
Probe radius, r	0.254
Probe position, d	17.4625

[*] All parameters are in millimeters.

TABLE 3.2
RESONANT FREQUENCIES[**]

	Structure A
TE_{101}	7.50
TE_{102}	9.79
TE_{103}	12.72
TE_{201}	13.61
TE_{104}	15.94
Probe half-wave resonance	11.81
Slot half-wave resonance	10.00

[**] All frequencies are in GHz.

Structure A

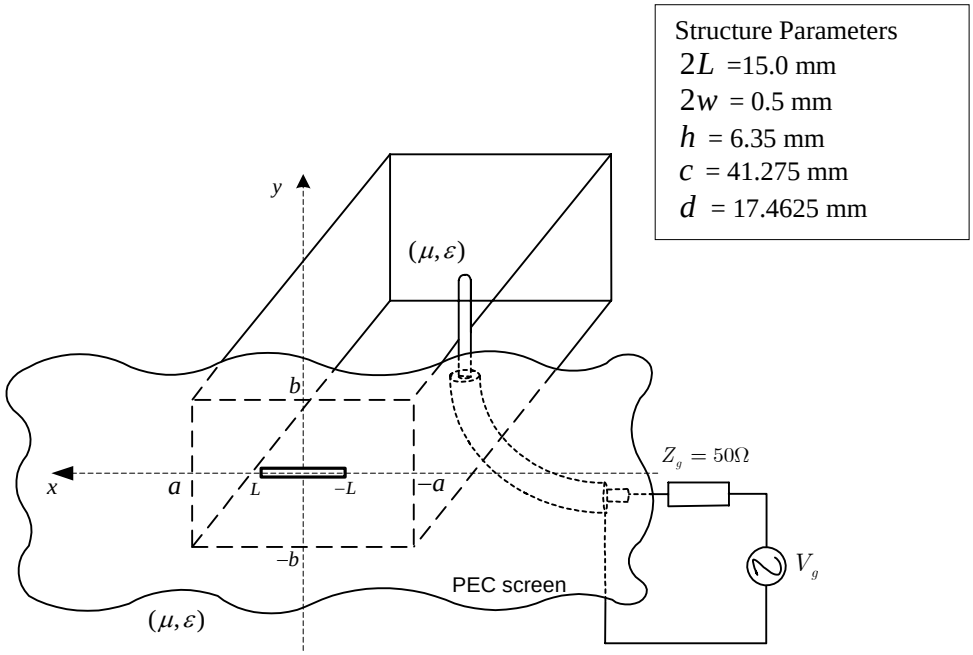

(a)

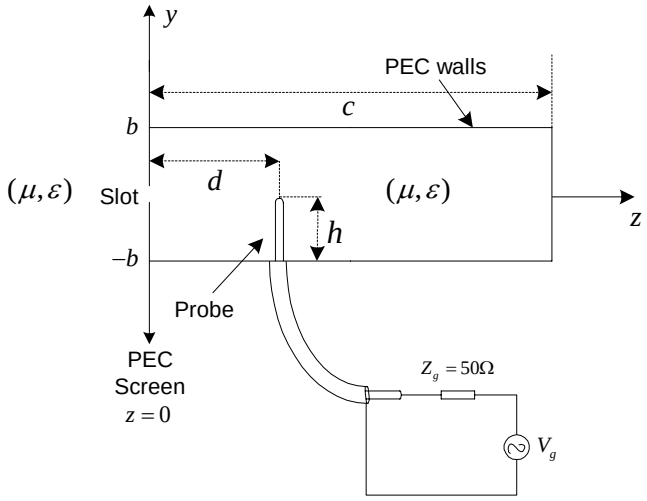

(b)

Fig. 3-1. A narrow slot in an infinite PEC screen backed by a rectangular cavity with a thin-wire probe in it – (a) perspective view. (b) side view.

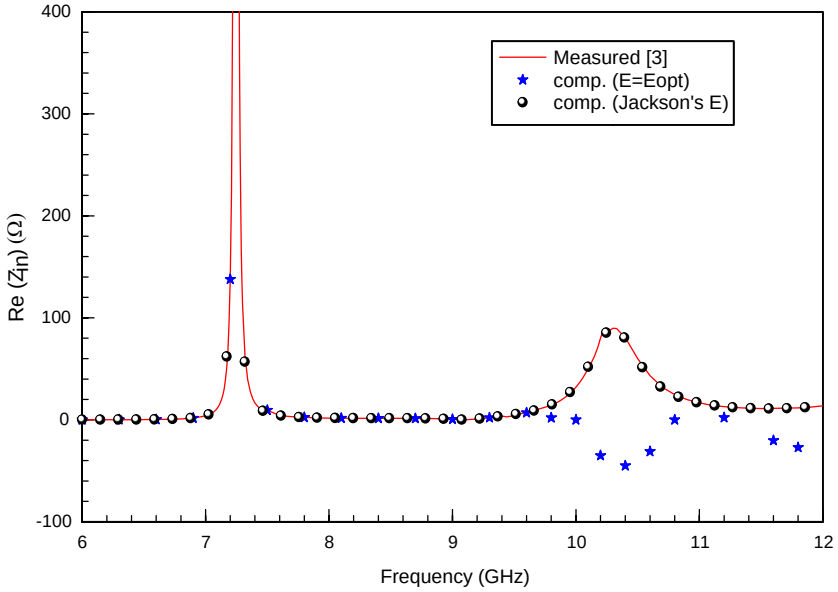

(a)

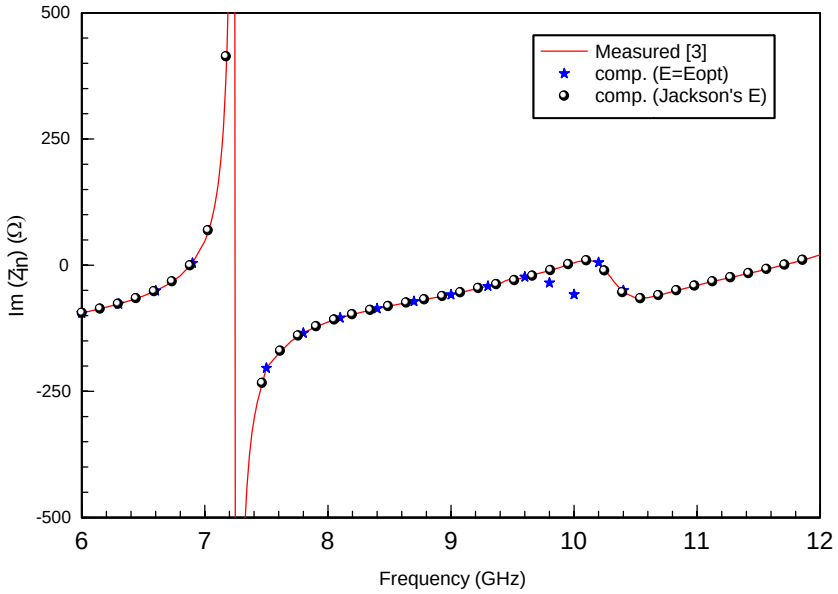

(b)

Fig. 3-2 - Input impedance at the base of the probe for Structure A (a) Real part of impedance. (b) Imaginary part of impedance.

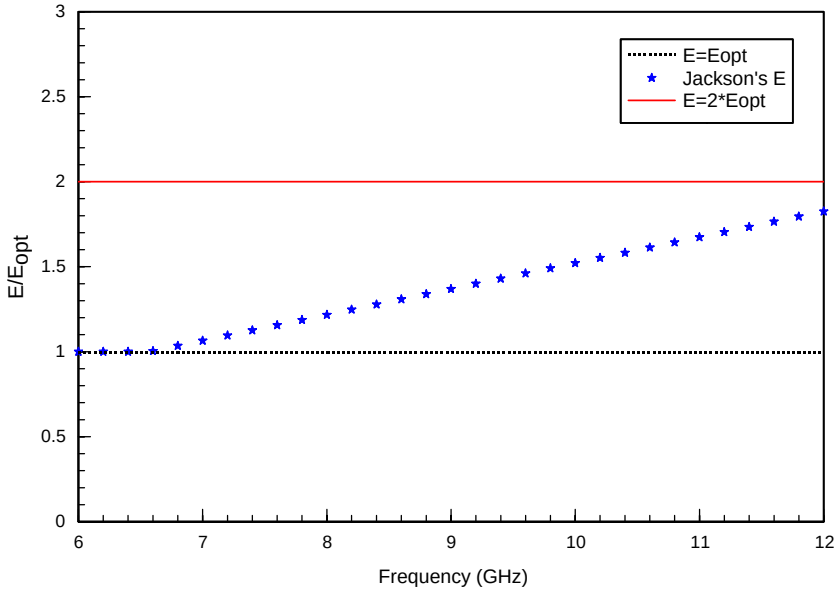

Fig. 3-3. Variation of E / E_{opt} with frequency for structure A.

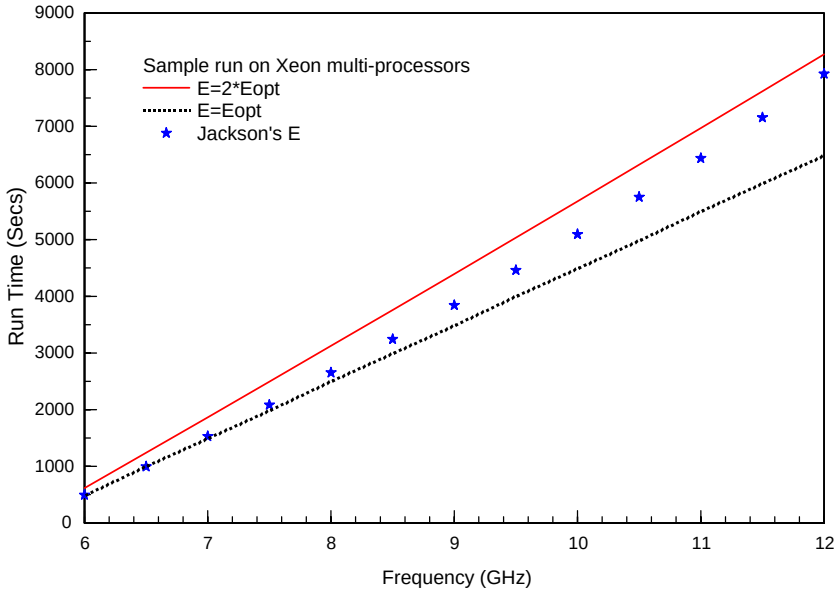

Fig. 3-4. Cumulative CPU time vs. frequency in computing input impedance at the base of the probe for structure A.

4. CONCLUSIONS

In this chapter a discussion of the Ewald method [1, 2] which is used to efficiently accelerate the convergence of the infinite series encountered in the calculation of matrix elements obtained by employing the method of moments for the numerical solution of the integral equations is discussed. Also, Jackson's method of determining the splitting parameter in the Ewald method has been discussed and results showing the accuracy and efficiency of this approach compared to an arbitrary method of choosing E have been detailed. Expressions for choosing the correct E parameter are arrived at after going through formulations from Jackson's method. The results obtained by using Jackson's method are compared to the measured results [3] and accuracy is established.

REFERENCES

[1] P. P. Ewald, "Die Berechnung Optischer und Electrostatischer Gitterpotentiale," Annelen der Physik, vol. 64, pp. 254-287, 1921.

[2] P. P. Ewald, "Theorie der Dispersion, Reflexion und Brechung," Annelen der Physik, vol. 49, pp. 1-38, 1916.

[3] A. Kustepeli, "Analysis and Implementation of the Ewald Method for Waveguide and Cavity Structures," Clemson University, Dissertation, December 1999.

[4] D. Shanks, "Non-linear Transformations of Divergent and Slowly Convergent Sequences," J. Math. and Physics, vol. 34, pp. 1-42, 1955.

[5] S. Singh, W. F. Richards, J. R. Zinecker, and D. R. Wilton, "Accelerating the Convergence of Series Representing the Free Space Periodic Green's Function," IEEE Trans. Antennas Propagat., vol 38, pp. 1958-1962, December 1990.

[6] P. Wynn, "On a Device for Computing the $e_m(S_n)$ Transformation," Math. Tables and Aids to Comp., vol 10, pp. 91-96, 1956.

[7] D. Jackson (private communication).

[8] A. Kustepeli and A. Q. Martin, "On the splitting parameter in the Ewald Method," *IEEE Microwave and Guided Wave Letters*, vol. 10, No. 5, pp. 168-170, May 2000.

[9] K. E. Jordan, G. R. Richter, and P. Sheng, “An Efficient Numerical Evaluation of the Green’s Function for the Helmholtz Operator on Periodic Structures,” J. Comp. Physics, vol. 63, pp. 222-235, 1986.

[10] M. J. Park, J. Park, and S. Nam, “Efficient Calculation of the Green’s Function for the Rectangular Cavity,” IEEE Microwave and Guided Wave Letters, vol. 8, pp. 124-126, March 1998.

[11] D. R. Wilton, D. R. Jackson, and N. J. Champagne, “Efficient Computation of periodic Green’s Functions in Layered Media Using the Ewald Method,” in Dig. URSI Nat. Radio Science Meet., Boulder, CO, January 1998, p. 311.

[12] V. N. Faddeyeva and N. M. Terent’ev, Tables of Values of the Function $w(z) = \exp(-z^2)\left(1 + \frac{2i}{\sqrt{\pi}} \int_0^{\pi} \exp(t^2)dt\right)$ for Complex Argument (Gosud. .Izdat. Teh. - Teor. Lit., Moscow 1954, English Translation by D.G. Fry, Pergamon Press, New York, 1961).

[13] G. P. M. Poppe and C. M. J. Wijers, “More Efficient Computation of the Complex Error Function,” ACM Trans. Math. Software, vol. 16, pp. 38-46, 1990.

[14] G. P. M. Poppe and C. M. J. Wijers, “Algorithm 680 - More Efficient Computation of the Complex Error Function,” ACM Trans. Math. Software, vol. 16, pp. 47, 1990.

CHAPTER 4

EFFICIENT MODELING USING MATRIX INTERPOLATION METHODS

The free-space periodic Green's function appears as the kernel of the integral equations formulated for slot-coupled cascaded rectangular cavities. One usually encounters extremely slowly convergent series in the calculation of the matrix elements occurring in the method of moments (MoM) numerical solution of these integral equations. One is thus left with a computationally heavy task of computing the matrix elements. One approach that is useful for this task is to employ matrix interpolation techniques (MITs) to compute the elements of the system matrix to reduce the overall computation time. In this chapter a discussion of the MIT and, in particular, the ratio of polynomials (ROPs) method [1] is provided and numerical results are given to establish the accuracy and efficiency of this approach compared to direct computations.

1. INTRODUCTION

An investigation of an efficient method for the computation of the broadband performance of slot-coupled cascaded rectangular cavities using frequency interpolation [1, 3] of the MoM matrix is presented. In the evaluation of cascaded cavities for obtaining wideband data, the MoM numerical solution can take a very, very long time since the system matrix has to be computed separately for each new frequency. With an

interpolation method, the elements of only a few matrices at relatively large frequency intervals are directly computed. These matrices are then used to interpolate the elements of the system matrix at many intermediate frequencies. Interpolation reduces the time [1, 3] required to compute the cavity performance over a wide frequency band.

Two methods that are commonly used for electromagnetic analysis are the finite-difference time-domain (FDTD) method [4, 5] and the method of moments (MoM) [6, 7, 8]. FDTD predicts performance over a wide band of frequencies in one simulation. The frequency-domain MoM approach computes the system matrix one frequency at a time and requires the computation of many frequency points for broadband performance evaluation. This can take a long time in situations where each matrix element requires a large amount of CPU time since the system matrix will have to be recomputed for each new frequency point. Popular methods of reducing the computation time and significantly speeding up the overall simulation process rely on the use of numerical and geometrical approximations to quickly fill the system matrix or efficient matrix inversion and solution algorithms [7, 8].

The $[Z]$ interpolation method was originally proposed by Newman and Forrai [9] for the scattering analysis of a microstrip patch. Newman [3] also used it for the impedance analysis of a straight dipole antenna and flat square plate. In [1, 2] Virga and Rahmat-Samii discuss $[Z]$ and $[Y]$ interpolation methods that involve simple interpolation functions which require only a few coefficients and which can be applied to a wide variety of geometrical configurations. The technique is also independent of excitation and imposes few restrictions on geometry. Their work expanded the utilization of $[Z]$ interpolation to the wideband performance evaluation of complex antennas and

also investigates a comparable $[Y]$ interpolation approach. The methods are applied in the context of a triangular surface patch MoM formulation [2]. In [1], the $[Z]$ and $[Y]$ interpolation techniques are compared and the accuracy and computational efficiency of the two methods are discussed along with the implementation guidelines.

Generally, the elements of $[Z]$ and $[Y]$ calculated in free-space vary slowly with frequency while the elements calculated in the presence of the rectangular cavity fluctuate rapidly with frequency. The elements of $[Z]$ and $[Y]$ calculated in the presence of the rectangular cavity strongly depend upon the overall behavior of the entire structure. The elements of $[Z]$ and $[Y]$ in free-space can be evaluated over a frequency range by simple and low-order interpolation functions, such as a quadratic polynomial. In contrast, the interpolation of elements in the presence of the rectangular cavity over a frequency range requires interpolation functions such as the ratio of two n^{th} order polynomials to accurately capture the frequency behavior. The interpolation method used to compute the system matrix discussed in Chapter 2 of this report is outlined in the next section.

2. METHODOLOGY – RATIO OF POLYNOMIALS INTERPOLATION

The ROPs interpolation method utilized here focuses on matrix interpolation methods that:

- are easily implemented in an existing method-of-moments computer code, thus requiring no significant code modifications;
- accurately constructs the surface current, impedance, etc.;
- utilizes simple interpolation functions that require only a few coefficients;
- apply to a wide variety of configurations;

- impose few restrictions on the geometry modeling;
- are independent of excitation.

Each element of the matrix is approximated by the ratio of two polynomials [1] given as

$$C_{mn}(f) = \frac{a_{mn,0} + a_{mn,1} f + a_{mn,2} f^2 + ... + a_{mn,p} f^p}{1 + b_{mn,1} f + b_{mn,2} f^2 + ... + b_{mn,d} f^d}, \tag{4.1}$$

where f denotes the frequency, p denotes the order of the numerator polynomial, d denotes the order of the denominator polynomial, and $a_{mn,i}$ and $b_{mn,i}$ are the mn^{th} elements of the complex coefficient matrices $[a_i]$ and $[b_i]$, respectively. When the numerator and the denominator have the same or nearly the same degree, the ratio of polynomials representation of matrix element C_{mn} is often better than a polynomial approximation [10]. In this approach $p + d + 1$ coefficient matrices are computed.

The C_{mn} matrix interpolation begins by defining the order of the polynomials in (4.1). Next, $p + d + 1$ frequencies within the frequency range of interest are chosen. A N x N matrix is computed at each selected frequency f. The elements of these matrices are then used to determine the $p + d + 1$ complex coefficient matrices as shown in (4.4). The mn^{th} element of each coefficient matrix is then substituted into (4.1) to compute the corresponding elements of the C_{mn} matrix at each intermediate frequency.

The C_{mn} matrix elements are highly dependent upon the resonant characteristics of the structure. The choices of the polynomial orders in the numerator and denominator depend upon the proximity of adjacent structure resonances and the overall evaluation frequency range. Since one typically does not know the location of the resonances

beforehand, there is no convenient way to quickly determine the order of the numerator and denominator polynomials. In this work, the same order for the numerator and the denominator polynomials is used. Equation (4.1) can be rewritten as

$$\begin{aligned} &C_{mn}(f)+C_{mn}(f)b_{mn,1}f+C_{mn}(f)b_{mn,2}f^2+...+C_{mn}(f)b_{mn,d}f^d \\ &=a_{mn,0}+a_{mn,1}f+a_{mn,2}f^2+...+a_{mn,p}f^p. \end{aligned} \tag{4.2}$$

The unknowns, $a_{mn,i}$, $i=0,\ ...,\ p$, and $b_{mn,i}$, $i=1,\ ...,\ d$, are then calculated as a solution of the matrix equation where f is the selected frequency within the band that is chosen for direct evaluation. The matrix equation is of the form

$$[A][x]=[B] \tag{4.3}$$

where $[x]$ is the unknown column matrix. The complete equation is shown in (4.4).

$$\begin{bmatrix} 1 & f_1 & f_1^2 & f_1^3 & f_1^4 & -C_{mn,f_1}f_1 & -C_{mn,f_1}f_1^2 & -C_{mn,f_1}f_1^3 & -C_{mn,f_1}f_1^4 \\ 1 & f_2 & f_2^2 & f_2^3 & f_2^4 & -C_{mn,f_2}f_2 & -C_{mn,f_2}f_2^2 & -C_{mn,f_1}f_2^3 & -C_{mn,f_1}f_2^4 \\ 1 & . & & & & & & & \\ 1 & . & . & . & & & & . & \\ 1 & f_p & . & . & & & & . & \\ 1 & . & . & . & & & & . & \\ 1 & . & & & & & & & \\ 1 & f_{d-1} & f_{d-1}^2 & . & . & . & & & \\ 1 & f_d & f_d^2 & f_d^3 & f_d^4 & -C_{mn,f_d}f_d & -C_{mn,f_d}f_d^2 & -C_{mn,f_d}f_d^3 & -C_{mn,f_d}f_d^4 \end{bmatrix} \begin{bmatrix} a_{mn,0} \\ . \\ . \\ a_{mn,p-1} \\ a_{mn,p} \\ b_{mn,1} \\ . \\ . \\ b_{mn,d} \end{bmatrix} = \begin{bmatrix} C_{mn,f_1} \\ C_{mn,f_2} \\ \\ . \\ . \\ . \\ \\ \\ C_{mn,f_d} \end{bmatrix}. \tag{4.4}$$

The flow chart in Fig. 4-1 shows the polynomial interpolation method as applied to a narrow slot in an infinite PEC screen backed by a rectangular cavity with a thin-wire probe in it. The slot and the probe terms in the presence of the rectangular cavity are

computed by the direct MoM as their resonance behavior is not captured with a 10^{th}-order polynomial interpolation method (see Fig. 4-2) and it is advantageous to use the direct computation instead. The slot and the probe terms in the presence of the rectangular cavity vary rapidly with frequency and hence it is difficult to approximate these terms with the 10^{th} order interpolation method. The coupling terms and the slot self-terms are, however, computed by the use of the ROPs technique. Eventually all the matrix elements are assembled together for impedance calculations.

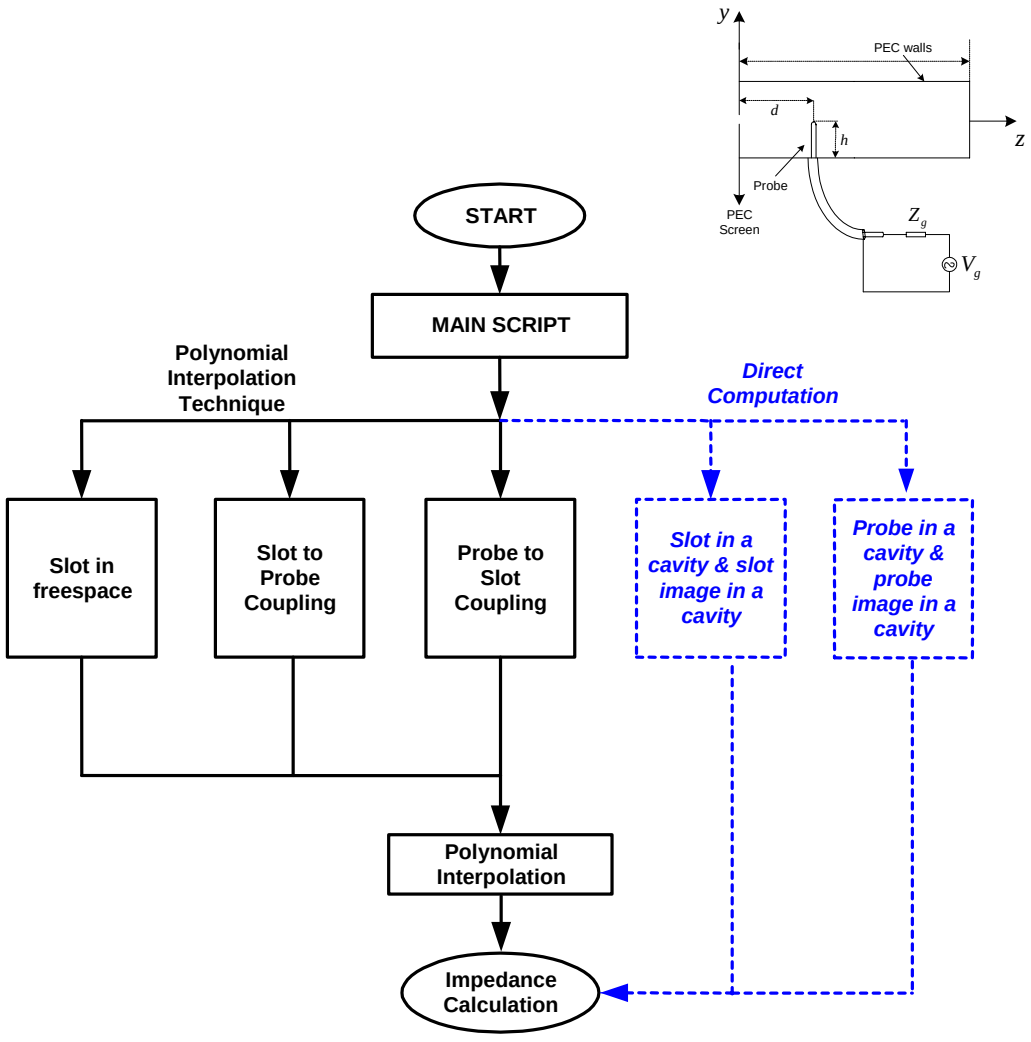

Fig. 4-1. Matrix interpolation methodology – ROPs technique as applied to a narrow slot in an infinite PEC screen backed by a rectangular cavity

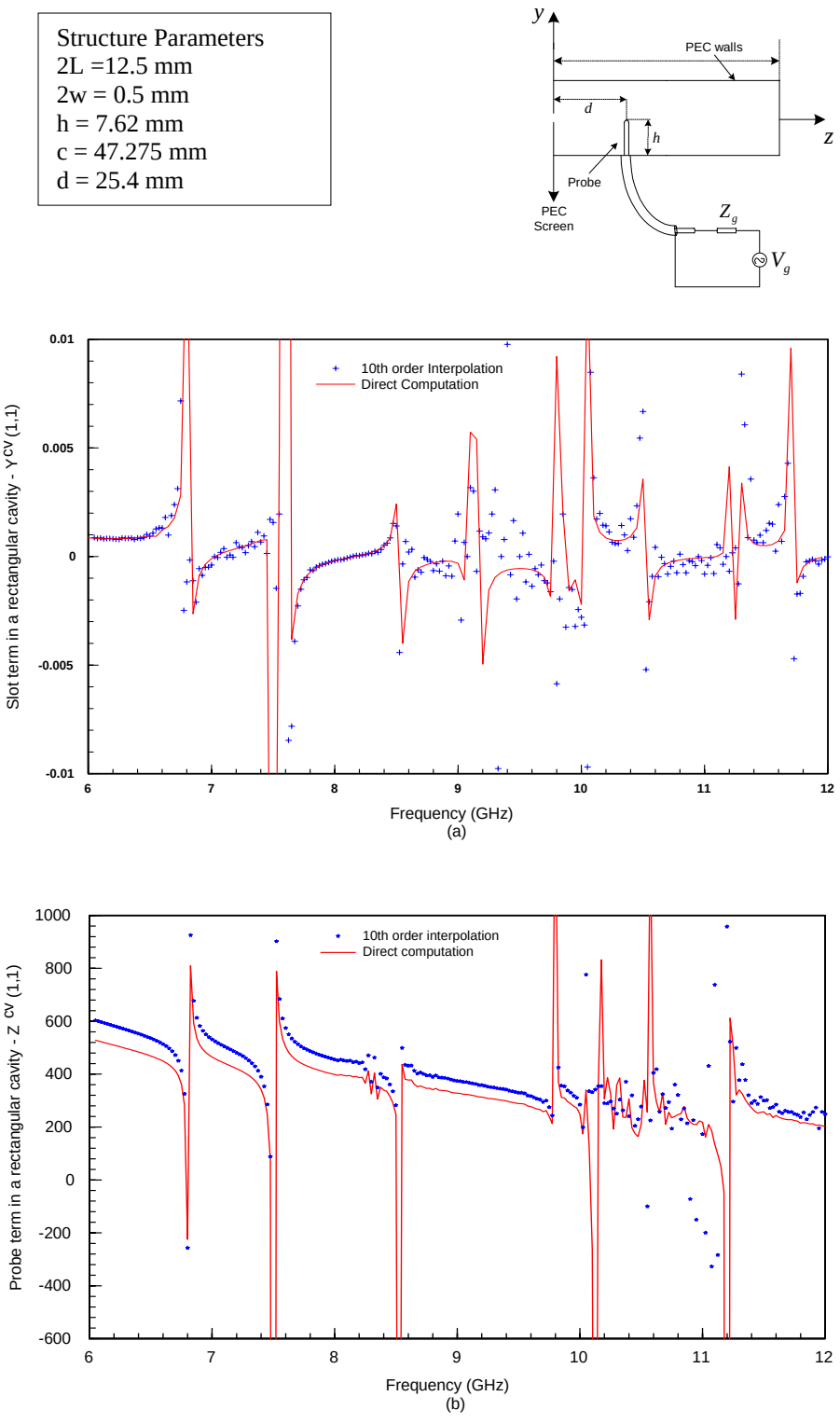

Fig. 4-2. (a) Slot term ($Y_{1,1}^{cv}$) in a rectangular cavity for the structure shown in Fig. 4-4. (b) Probe term ($Z_{1,1}$) in a rectangular cavity for the structure shown in Fig. 4-4. (Single matrix element computed by direct MoM and ROPs interpolation)

3. RESULTS

To investigate the accuracy of the matrix interpolation technique, the antenna input impedance is illustrated in Fig. 4-3 for a dipole antenna of length $L = 0.5\ \mathrm{m}$ over a range from 200 to 1400 MHz, with 1st -order, 2nd -order and 4th -order polynomial interpolations. The antenna is subdivided into 20 equal segments in length of about 0.12λ at 1400 MHz where $N = 19$ basis functions are used. The results show close agreement between the direct MoM and 2nd and 4th-order interpolations. The 4th-order interpolation curve in Fig. 4-3 provides very accurate data in the sense that the error in interpolating $[Z_{mn}]$ is negligible. However, some error is observable in the 2nd and 1st-order cases. The deviation from the direct MoM results around 640 MHz and 1120 MHz is a good measure of the interpolation error. The 4th-order interpolation data also shows some deviations, but they are much smaller.

One may use the polynomial interpolation technique for the analysis of probes and slots in rectangular cavities, the results of which are discussed in detail here. As shown in Fig. 4-4, the structure under examination is a narrow slot in an infinite PEC screen backed by a rectangular cavity with a thin-wire probe present inside the cavity. The length of the thin-wire probe is h and its radius is r. The probe axis is located in the yz plane with d representing its displacement from the $z = 0$ plane. The slot length is $2L$ and its width is $2w$. The width, height, and depth of the cavity shown in the figure are $2a,\ 2b \text{ and } c$, respectively. The medium inside the cavity and in the left half-space is characterized by (μ, ε). The probe is connected via a 50Ω coaxial cable to a signal source having an internal impedance of 50Ω.

Fig. 4-5(a) and Fig. 4-5(b) show that the slot self-coupling elements can be interpolated to an accurate approximation through the ratio of polynomials interpolation method. One may use the 10th-order ROPs approximation to compute the slot self-coupling terms $Y^s_{1,1}$ and $Y^s_{2,3}$. The agreement between the direct MoM and the interpolated results is excellent throughout the frequency range of $6\ \mathrm{GHz}$ to $12\ \mathrm{GHz}$.

Fig. 4-6 and Fig. 4-7 show the probe-to-slot coupling elements $C^{sp}_{1,4}$ and $C^{sp}_{2,6}$, which are similar to $C^{s_i p_i}_{m,n}$ defined in (2.47). One again sees good agreement between the direct MoM and the 10th-order polynomial interpolated results. To understand and explain these results, the ROPs representation was used to investigate how accurately it can compute a single matrix element. The coefficients for the 10th-order ROPs approximation were computed by evaluating matrix elements at 21 frequencies. Fig. 4-6 shows that 6th-order ROPs capture the behavior of the $C^{sp}_{1,4}$ term really well at the lower end of the frequency spectrum but does not at the higher frequencies. Fig. 4-8 shows the slot-to-probe coupling term $C^{ps}_{4,1}$, which is similar to $C^{p_i s_i}_{m,n}$ defined in (2.52), calculated by direct MoM and interpolation techniques. Again the agreement is excellent throughout the frequency range.

The real and imaginary parts of the input impedance of the thin-wire probe in the frequency range between $6\ \mathrm{GHz}$ and $12\ \mathrm{GHz}$ are shown in Fig. 4-9 for structure A of Table 4.1. Numerical results are obtained by using the direct MoM and 10th-order ROPs interpolation. Examining the figure, the TE_{101} mode is seen to be excited near $7.3\ \mathrm{GHz}$ in both methods, which is very close to the resonant frequency of this mode ($7.5\ \mathrm{GHz}$). The TE_{102} mode is the second mode excited for this structure with its excitation

occurring near 10.3 GHz. Since the probe is located at $d \cong c/2$, the change seen in the input impedance because of the excitation of this mode is not as drastic as the excitation of the TE_{101} mode. The direct MoM results and interpolated results show complete agreement throughout the frequency range.

Fig. 4-10 shows the real and imaginary parts of the input impedance of the thin-wire probe for structure B of Table 4.1 in the frequency range between 6 GHz and 12 GHz. Data from direct MoM is compared with the numerical results obtained by using 10^{th}-order ROPs. The agreement between the two methods is very good over the entire frequency range. Examining the figure, the TE_{101} mode is excited at about 7.27 GHz in both the methods and since the wire is located at $d \cong c/2$, the TE_{102} mode is excited slightly.

Fig. 4-11 shows the cumulative computation time for direct MoM and that for the interpolation. The bulk time in the interpolated method is utilized in the calculation of the 21 selected frequencies and the interpolation procedure, in comparison, is a fast process. Examining the figure, approximately 21000 seconds were required for the computation of matrix elements at the 21 selected frequencies and the frequency sweep over the range from 6 GHz to 12 GHz was a much faster process. In contrast, the calculation of matrix elements in the direct method is a computationally very heavy task. The time advantage in the ROPs method is apparent from the figure.

The [Y] matrix interpolation and coupling matrix interpolation methodologies have been used with the method of moments in order to significantly reduce the computation time required for the wideband performance evaluation of slot-coupled cascaded rectangular cavities. These interpolation methods do not require a prior

knowledge of cavity resonance characteristics. The results included a comparison of the time savings of the interpolation method over the direct MoM approach. Sometimes large-order polynomials are required to accurately reproduce the elements via matrix interpolation and still they have a good time advantage over the direct method. Higher-order polynomials for matrix interpolation require the storage of more coefficients than the lower-order matrix interpolation techniques and require more computation time. The advantage of a particular interpolation method such as ROPs technique to simple interpolation techniques such as the quadratic interpolation is based upon the general resonant nature of the cavity to be modeled. When many resonances occur within a particular frequency range, ROPs matrix interpolation is faster and requires less computational resources than the direct method. The results presented in this chapter demonstrate the applicability of the ROPs matrix interpolation methods.

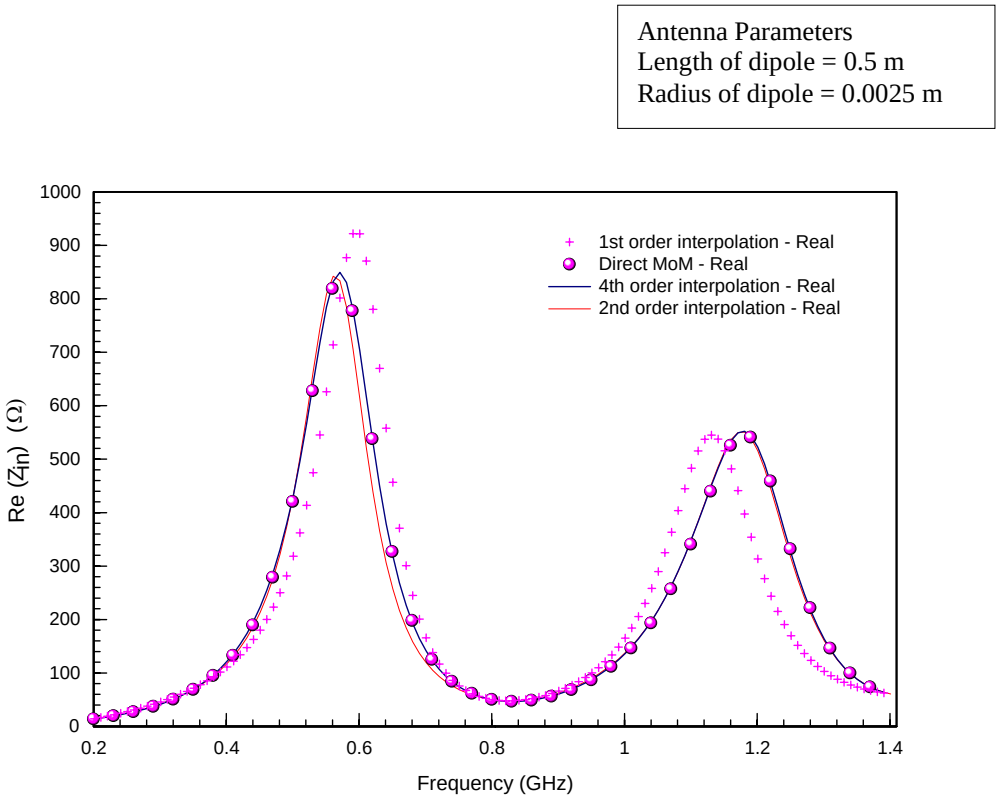

Fig. 4-3. Dipole antenna input impedance using polynomial interpolation technique. (a) real part of impedance. (b) imaginary part of impedance.

TABLE 4.1
STRUCTURE PARAMETERS

Parameter*	**Structure A**	**Structure B**
Cavity width, $2a$	22.86	22.86
Cavity height, $2b$	10.16	10.16
Cavity depth, c	47.625	41.275
Slot length, $2L$	12.5	15.0
Slot width, $2w$	0.5	0.5
Probe length, h	7.62	6.35
Probe radius, r	0.254	0.254
Probe position, d	25.4	17.4625

*All parameters are in millimeters

TABLE 4.2
RESONANT FREQUENCIES**

	Structure A	**Structure B**
TE_{101}	7.27	7.50
TE_{102}	9.09	9.79
TE_{103}	11.50	12.72
TE_{201}	13.49	13.61
TE_{104}	14.20	15.94
Probe half-wave resonance	9.84	11.81
Slot half-wave resonance	12.00	10.00

*All frequencies are in GHz.

Structure Geometry

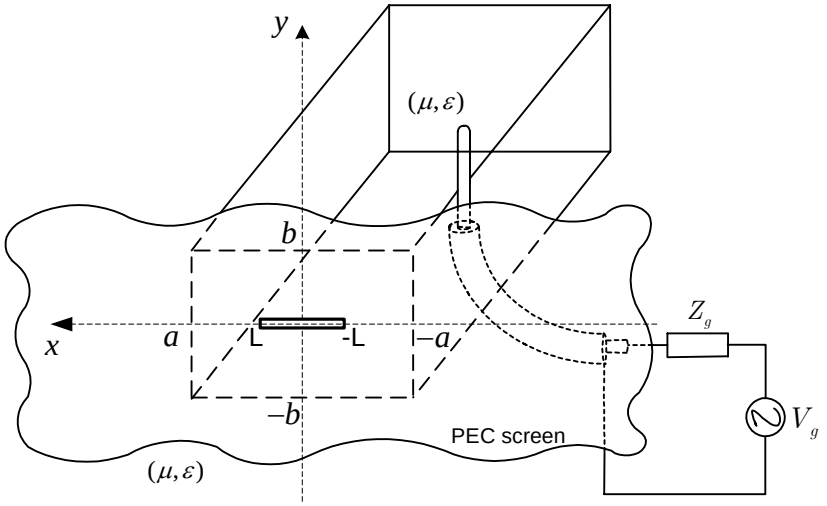

(a)

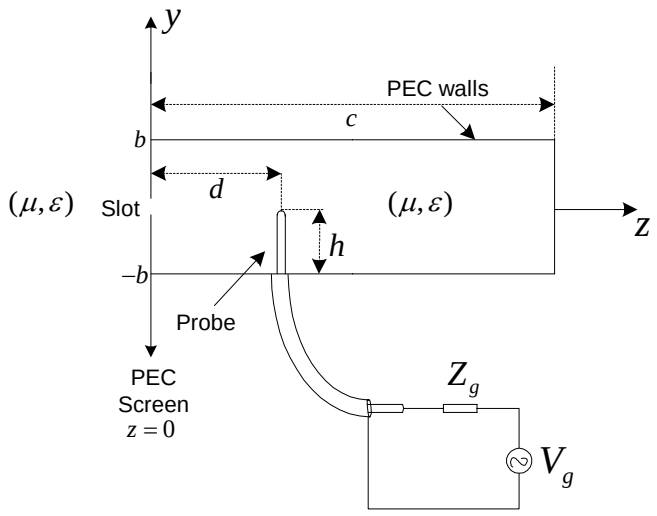

(b)

Fig. 4-4. A narrow slot in an infinite PEC screen backed by a rectangular cavity with a thin-wire probe in it – (a) perspective view. (b) side view.

Structure A Parameters
2L =12.5 mm
2w = 0.5 mm
h = 7.62 mm
c = 47.275 mm
d = 25.4 mm

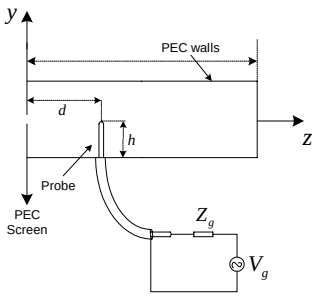

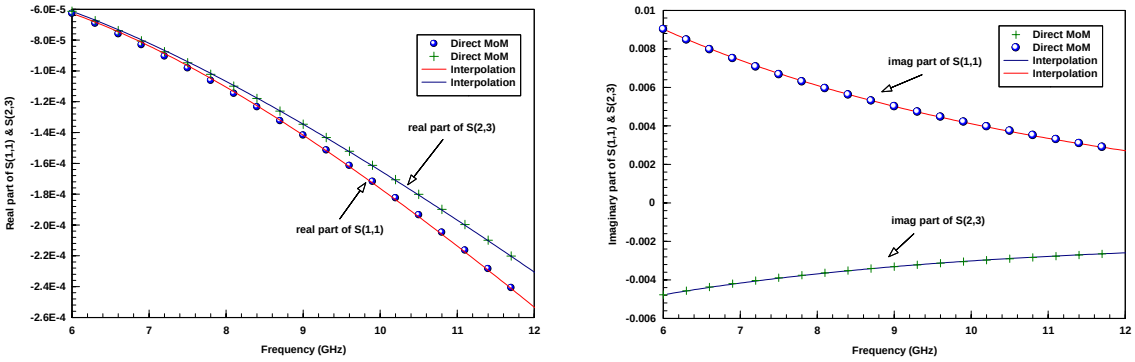

(a) (b)

Fig. 4-5. Slot self-coupling elements- $Y^s_{1,1}$, $Y^s_{2,3}$ - (a) real part (b) imaginary part

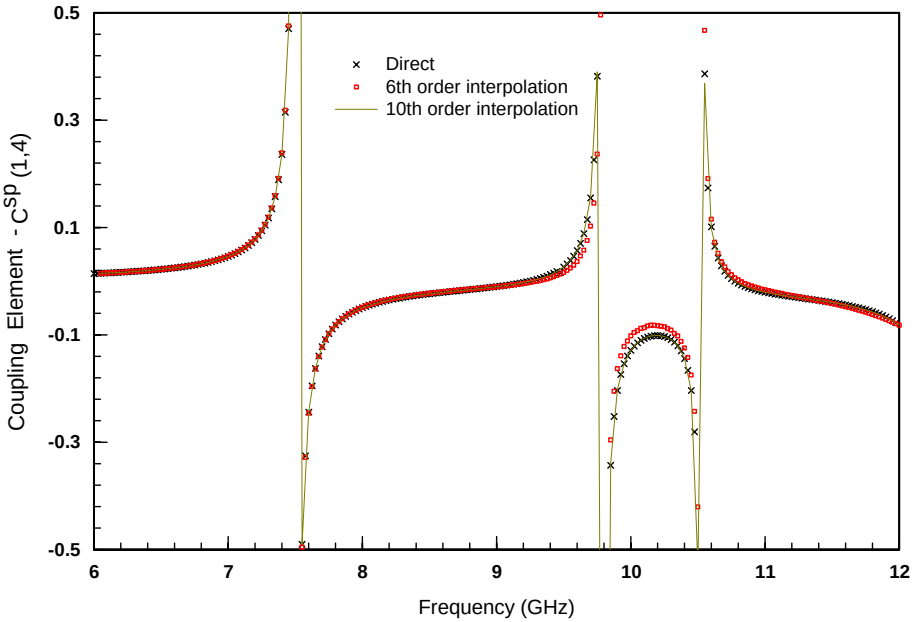

Fig. 4-6. Coupling element from probe to slot - $C^{sp}_{1,4}$ (single matrix element computed by direct MoM and ROPs interpolation)

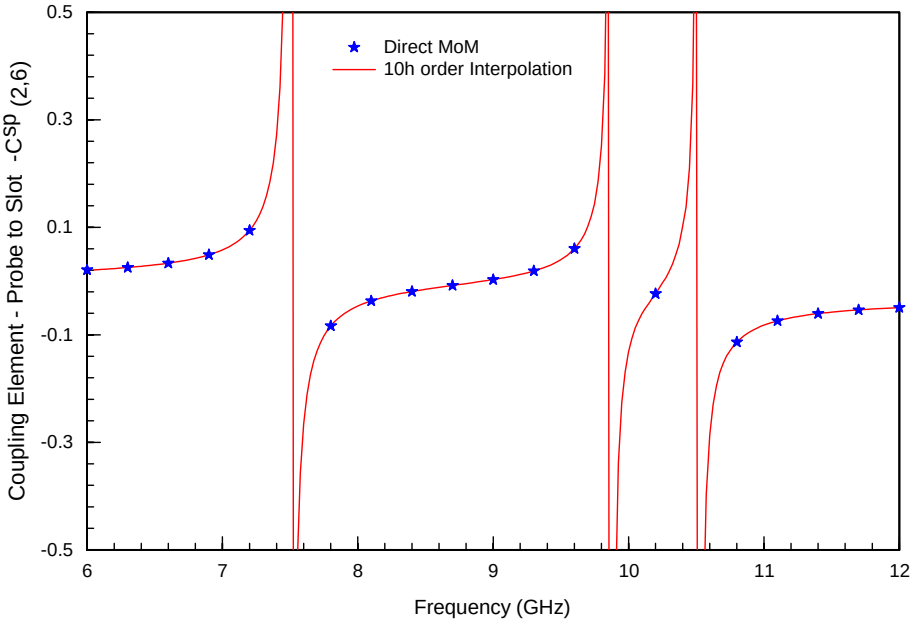

Fig. 4-7 Coupling element from probe to slot - $C^{sp}_{2,6}$ (single matrix element computed by direct MoM and ROPs interpolation)

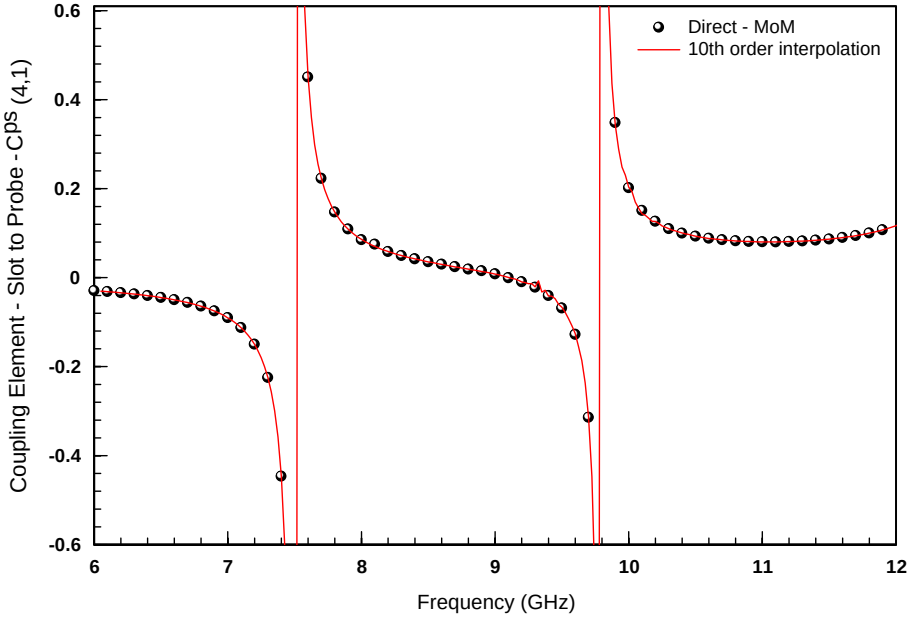

Fig. 4-8 Coupling element from slot to probe - $C^{ps}_{4,1}$ (single matrix element computed by direct MoM and ROPs interpolation)

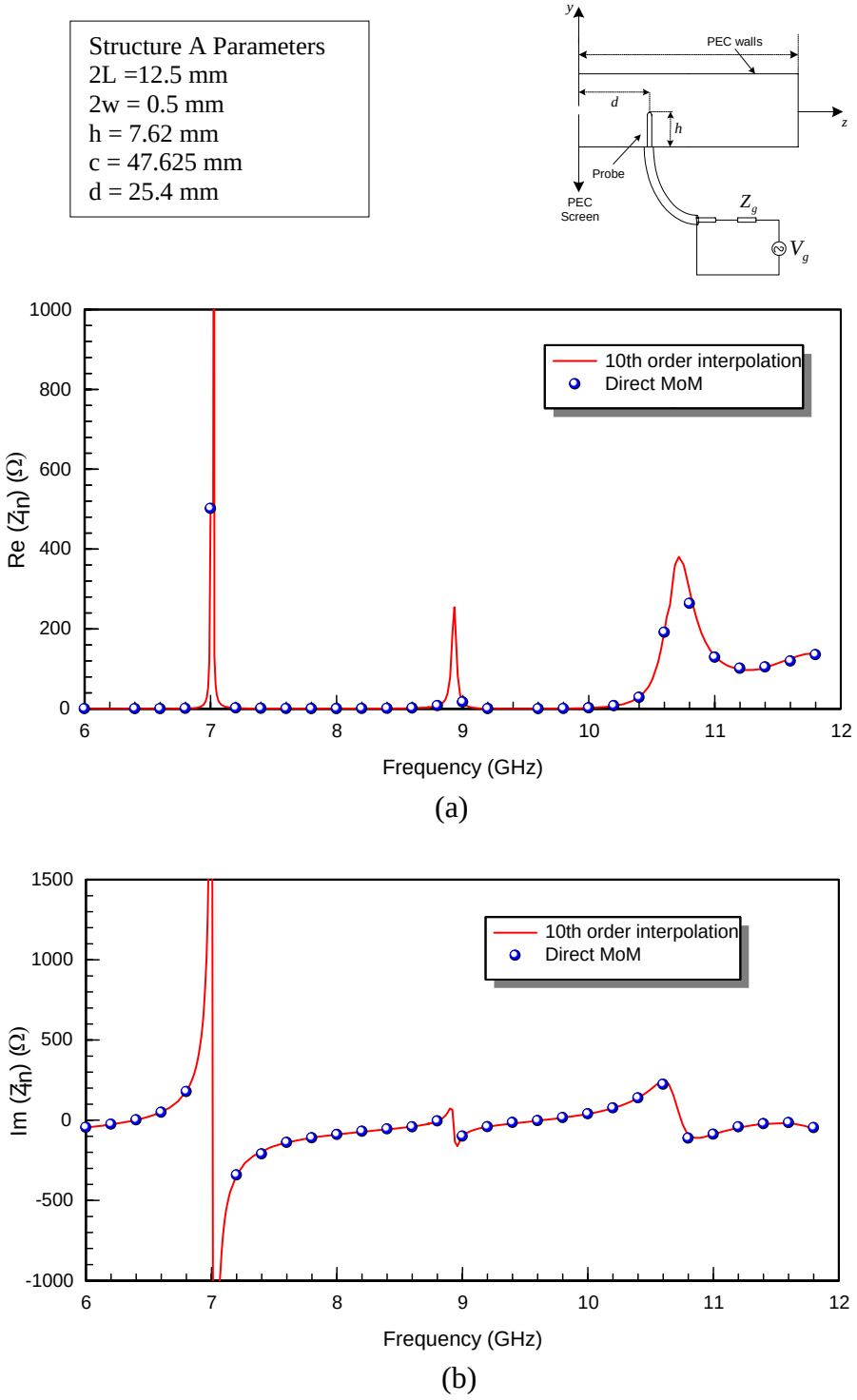

Fig. 4-9. Input impedance of the thin-wire probe inside a slotted cavity. (a) real part of input impedance. (b) imaginary part of input impedance. (30 frequency points computed for direct MoM)

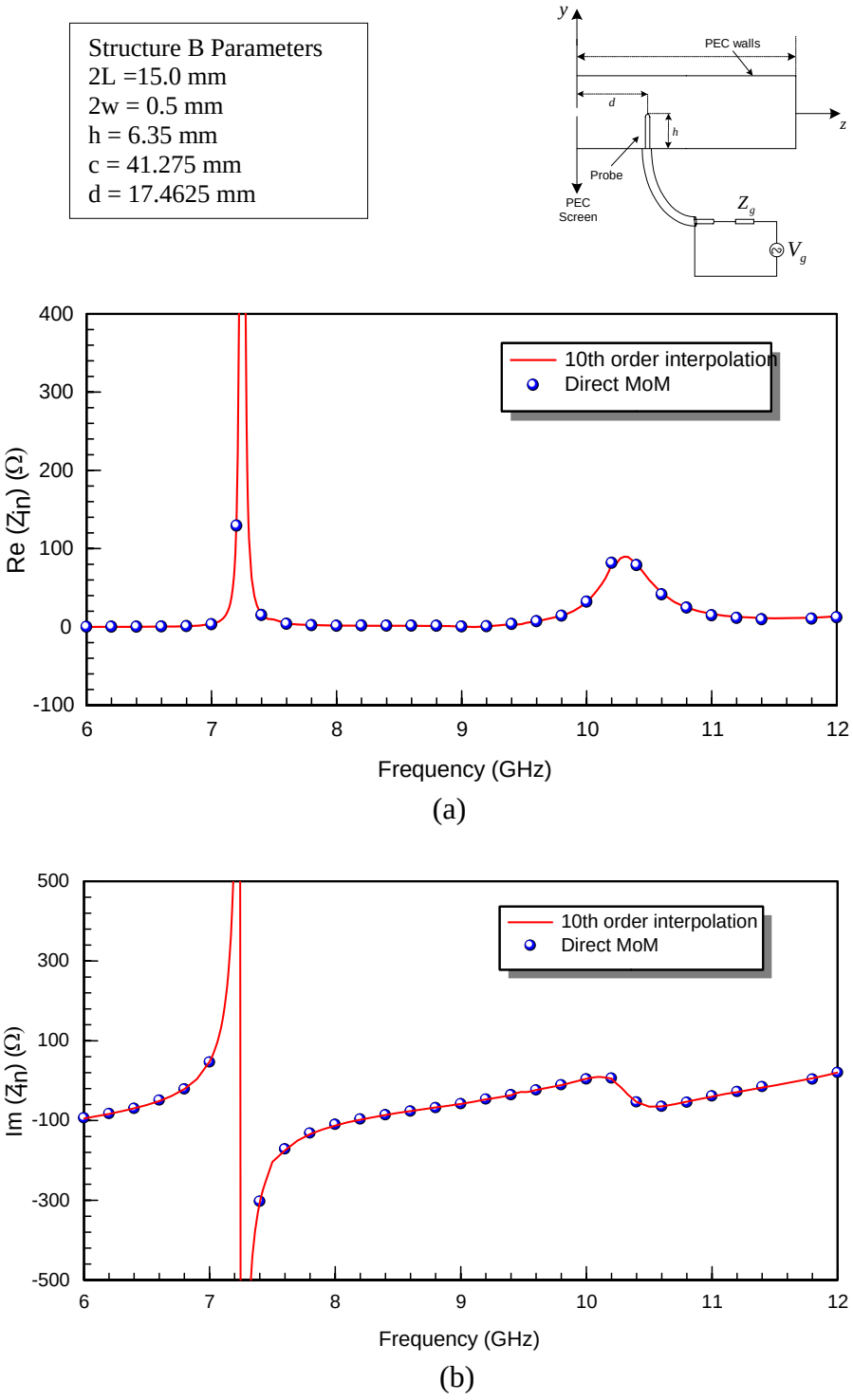

Fig. 4-10. Input impedance of the thin-wire probe inside a slotted cavity. (a) real part of input impedance. (b) imaginary part of input impedance. (30 frequency points computed for direct MoM)

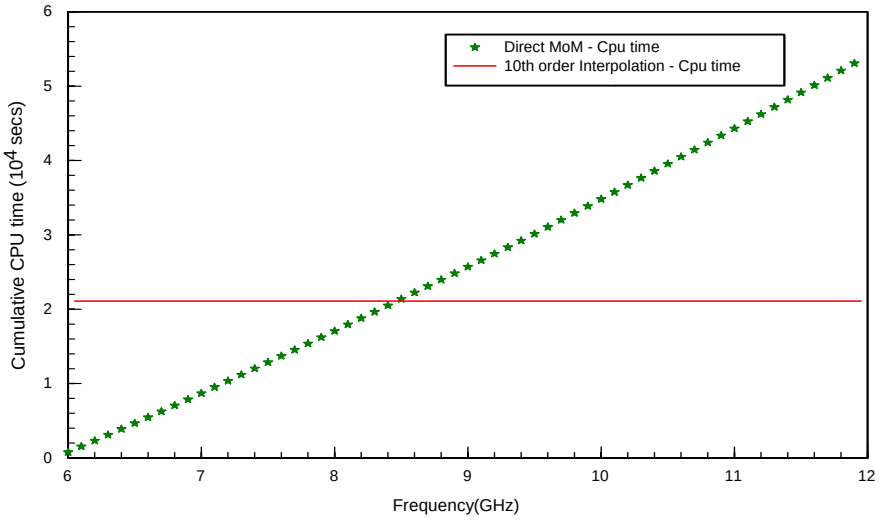

Fig. 4-11. Cumulative CPU time for direct method (MoM) and polynomial interpolation method for structure A. (60 frequency points computed for direct MoM and ROPs interpolation)

4. CONCLUSIONS

In this study an investigation of an efficient method for the computation of the broadband characteristics of slot-coupled cascaded rectangular cavities using frequency interpolation of MoM matrix is presented. The ROPs method of MoM matrix interpolation significantly reduced the computation time required for the wideband performance evaluation of cavity responses. Good agreement showing the efficiency and the accuracy of the ROPs method is observed in the results obtained by the ROPs matrix interpolation method and the results obtained by the direct MoM. Data included the CPU time comparison between the two methods.

APPENDIX: USE OF XEON MULTI-PROCESSORS TO REDUCE CPU TIME

The numerical solution of the cavity problem involves computation of very slowly convergent infinite series in the calculation of the matrix elements occurring in the method of moments (MoM) solution of integral equations, hence the enormous time required to compute the matrix elements. This led to the farming of codes on Xeon multi-processors, wherein the original FORTRAN code is fed into different Xeon processors simultaneously through the use of PBS (portable batch system) scripts. The main script controls the feeding of the sub-codes through the queue command and also assembles the results at the end of the runs. The full process is illustrated in the flow chart in Fig. 4-12. The computationally heavy segment of the FORTRAN code involves the calculation of matrix elements. The main script submits the '*n*' subordinate scripts one after the other into the queue and the subordinate scripts are submitted to the different nodes for separate calculations. The main script also assembles all the resultant elements into a complete

matrix file. An important criterion is the synchronization of all 'n' sub-scripts such that the next stage of computation starts after all 'n' codes exit successfully. The entire (n,n) matrix file is depicted in Fig. 4-13 along with the method of splitting them into 21 ($n=21$) different segments to be fed into various nodes. The Y_1 and Y_1^c terms in the figure are the admittance terms due to slot 1, and, Y_2 and Y_2^c are the admittance terms due to slot 2. The elements of the sub-matrices representing the coupling from the probe to slot 1 are given by C^{s1p} and the coupling from probe to slot 2 is given by C^{s2p}. C^{ps1} represents the slot 1 to probe coupling term and C^{ps2} represents the slot 2 to probe coupling term. Z is the impedance sub-matrix term for the probe.

The CPU time results, Fig. 4-14, for the performance of parallel codes in Xeon multi-processors are compared with a run in an Alpha system of dual processors (serial) for structure A parameters. The results show a massive improvement in cumulative CPU time when run on Xeons due to the farming across multiprocessors, an improvement of nearly 94% from the serial case for a wideband evaluation between $6\ \mathrm{GHz}$ and $12\ \mathrm{GHz}$.

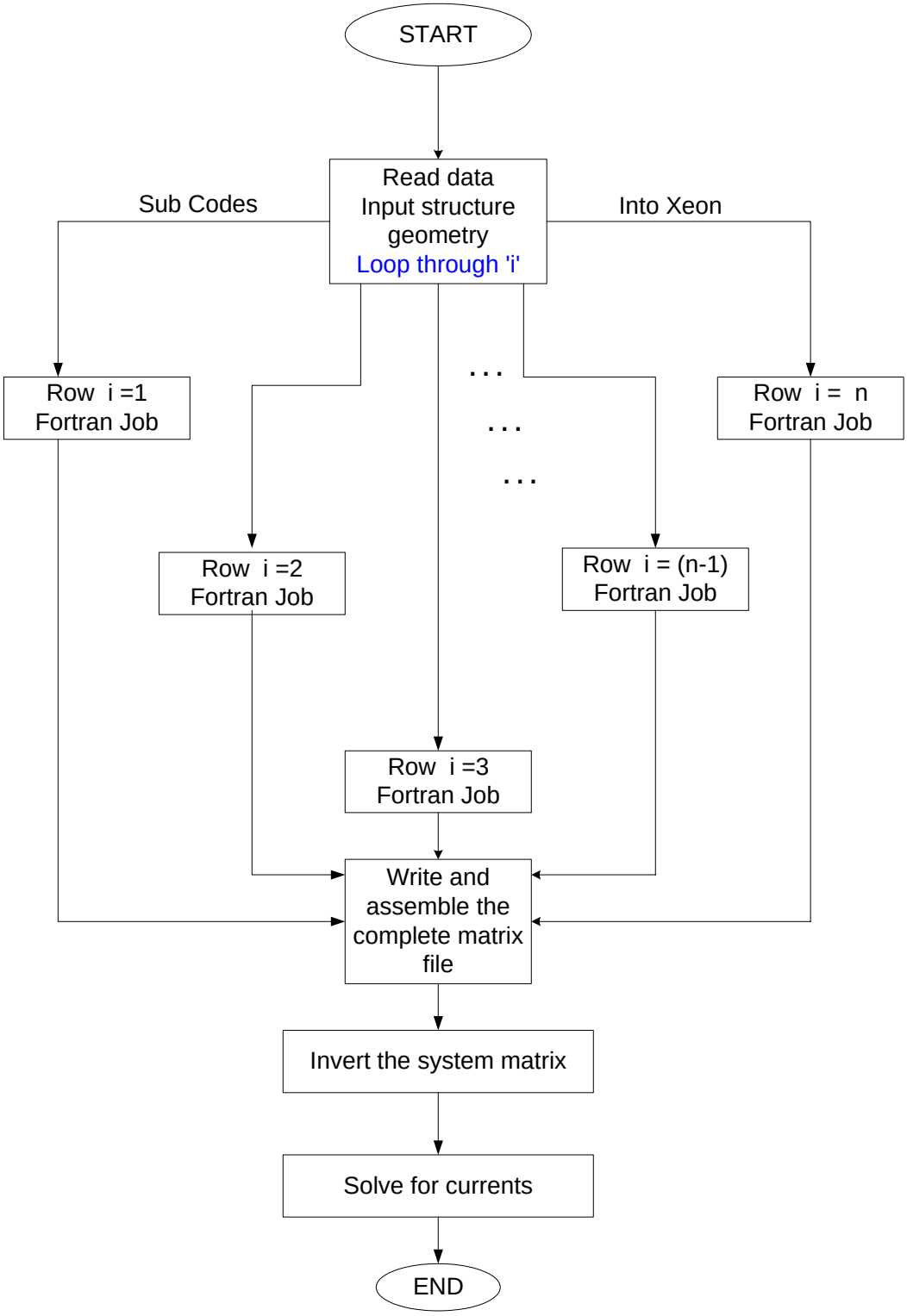

Fig. 4-12. Farming of FORTRAN program across Xeon multi-processors

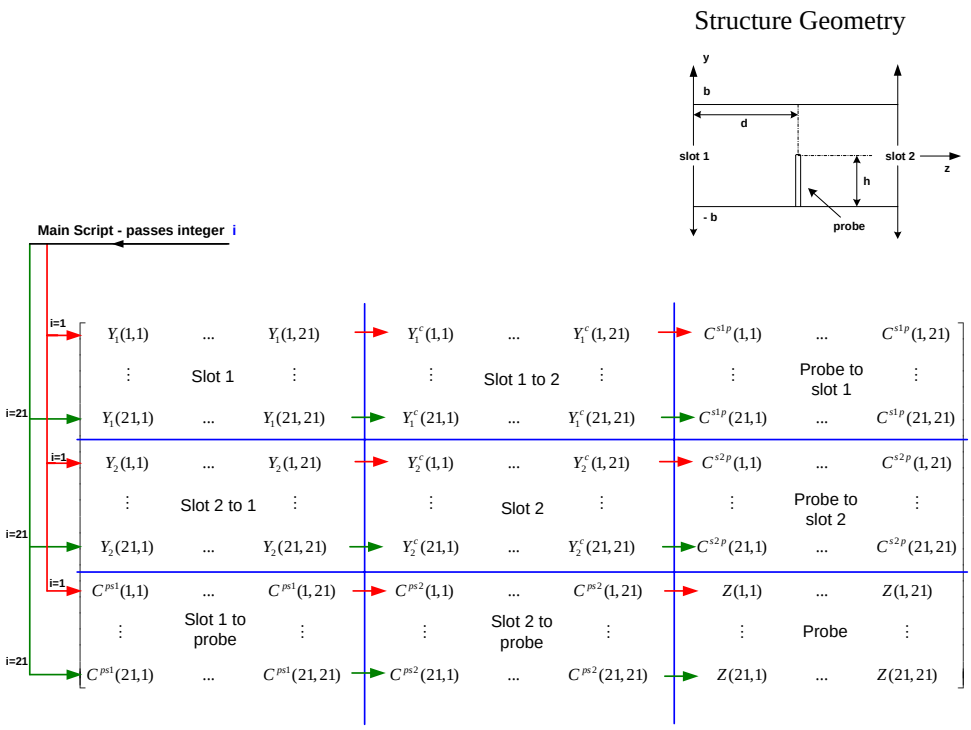

Fig. 4-13. Matrix fill mechanism for a single rectangular cavity with two slots and one probe.

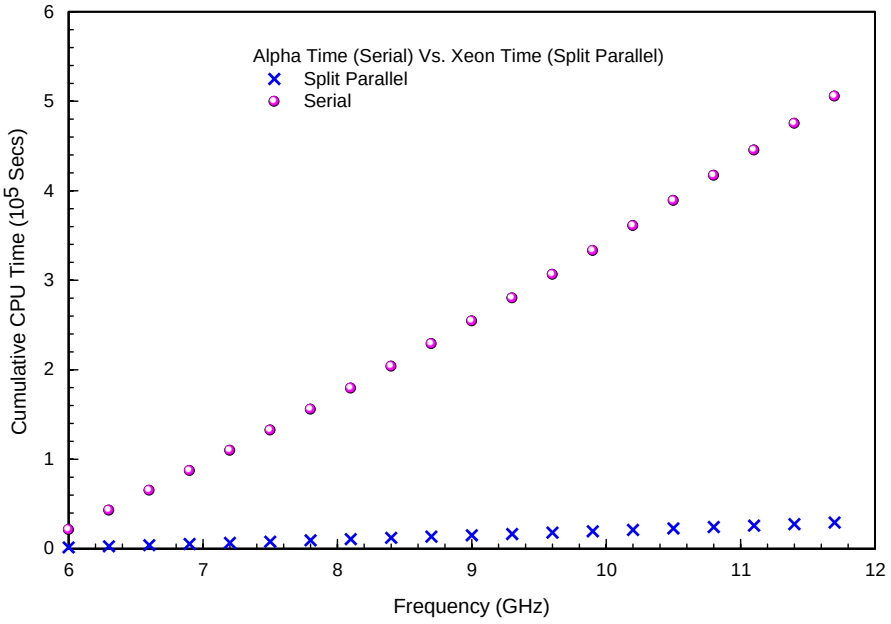

Fig. 4-14. Comparison of cumulative CPU time for Alphas and Xeon processors

REFERENCES

[1] K. L. Virga and Y. Rahmat-Samii, "Efficient Wide-Band Evaluation of Mobile Communications Antennas Using [Z] or [Y] Matrix Interpolation with Method of Moments," *IEEE Trans. Antennas Propagat*., vol. 47, pp. 65-76, Jan. 1999.

[2] K. L. Virga and Y. Rahmat-Samii, "Generation of wideband antenna performance by [Z] and [Y] matrix interpolation in the method of moments," in *Ultra-Wideband Short Pulse Electromagnetics III*. New York: Plenum, 1996.

[3] E. H. Newman, "Generation of wide-band data from the method of moments by interpolating the impedance matrix," *IEEE Trans. Antennas Propagat.*, 36, pp. 1820–1824, Dec. 1988.

[4] M. A. Jensen and Y. Rahmat-Samii, "Performance analysis of antennas for hand-held transceivers using FDTD," *IEEE Trans. Antennas Propagat.*, vol. 42, pp. 1106–1113, Aug. 1994.

[5] Y. Rahmat-Samii and M. A. Jensen, "Characterization of antennas for personal wireless communications applications," *Int. J. Wireless Inform. Networks*, vol. 1, pp. 165–175, 1994.

[6] S. M. Rao, D. R. Wilton, and A. W. Glisson, "Electromagnetic scattering by surfaces of arbitrary shape," *IEEE Trans. Antennas Propagat.*, vol. AP-30, pp. 409–418, May 1982.

[7] S. U. Wu and D. R. Wilton, "Electromagnetic scattering and radiation by arbitrary configurations of conducting bodies and wires," Tech. Document 1325, Appl. Electromagn. Lab., Dept. Elect. Eng., Univ. Houston, TX, Aug. 1988.

[8] R. E. Hodges and Y. Rahmat-Samii, "An iterative current-based hybrid method for complex structures," *IEEE Trans. Antennas Propagat.*, vol. 45, pp. 265–276, Feb. 1997.

[9] E. H. Newman and D. Forrai, "Scattering from a microstrip patch," *IEEE Trans. Antennas Propagat.*, vol. AP-35, pp. 245-251, Mar. 1987.

[10] R. L. Burden and J. D. Faires, *Numerical Analysis*, 5th ed. Boston, MA: PWS-Kent, 1988, ch. 8.

CHAPTER 5

NUMERICAL ANALYSIS OF SLOT-COUPLED CASCADED RECTANGULAR CAVITIES

Numerical results for signal propagation through cascaded rectangular cavities are presented in this chapter. The cascaded rectangular cavities are interconnected by narrow slots and have thin-wire probes/posts present in them. The input impedance at the center of the slot, input impedance at the base of the thin-wire probe and the electric field shielding (EFS) effectiveness [6] inside the rectangular cavity are calculated for single, double, and triply cascaded rectangular cavities.

1. INTRODUCTION

A numerical analysis of thin-wire probes inside slotted cascaded rectangular cavities is undertaken. The method of analysis is based on solving the coupled integral equations developed for the electric current on the probes and the equivalent magnetic current in the slots (see Chapter 2). The structure considered for investigation is a narrow slot in an infinite PEC screen backed by cascaded rectangular cavities that contain thin-wire probes/posts in them and which are interconnected by narrow slots. The analysis of this structure requires coupled integral equations which include the free-space periodic Green's function as part of their kernels. The coupled integral equations are solved by the method of moments [2].

The EFS [6] is calculated at the center of each rectangular cavity to evaluate the effect of the transmission path/environment on the entering transient signal and is defined as

$$EFS\ (dB) = -20\log\left|\frac{E_y(x,y,z)}{E_y^{inc}(x,y,z)}\right|, \tag{5.1}$$

where E_y is the amplitude of the electric field at a specified point in the presence of the enclosure and E_y^{inc} is the amplitude of the electric field at the same point with the enclosures removed. The field E_y^{inc} is given by

$$E_y^{inc} = V_0 e^{-jkz}, \tag{5.2}$$

where V_0 is the input voltage at the center of the slot and E_y is obtained from

$$\begin{aligned} E_y(x,y,z) = {} & \frac{1}{j4\pi\omega\varepsilon}\left(\frac{d^2}{dy^2}+\beta^2\right)\int_{-h}^{h} I(y')K(y,y')dy' \\ & + \frac{1}{2\pi}\int_{-L_s}^{L_s}\int_{-w}^{w} m(x')\frac{1/\pi}{\sqrt{w^2-y^2}}G_d^s(y,x',y')dy'dx', \end{aligned} \tag{5.3}$$

where $m(x)$ is the axial variation of the magnetic current on the slot and $I(y)$ is the electric current on the thin-wire probe. The term $K(y,y')$ is similar to $K_{cv_j}^{p_j}(y,y')$ in (2.35) and $G_d^s(y,x',y')$ is similar to $G_d^{s_j}(y,x',y')$ in (2.25). Equation (5.3) is applicable for a rectangular cavity with a single slot and probe. If the rectangular cavity has two slots, then

$$E_y(x,y,z)=\frac{1}{j4\pi\omega\varepsilon}\left(\frac{d^2}{dy^2}+\beta^2\right)\int_{-h}^{h} I_1(y')K_{cv}^{P}(y,y')dy' + \frac{1}{2\pi}\int_{-L_1}^{L_1}\int_{-w}^{w} m_1(x')\frac{1/\pi}{\sqrt{w^2-y^2}}G_d^{s1}(y,x',y')dy'dx' - \frac{1}{4\pi}\int_{-L_2}^{L_2}\int_{-w}^{w} m_2(x')\frac{1/\pi}{\sqrt{w^2-y^2}}G_d^{s2}(y,x',y')dy'dx' \quad (5.4)$$

where $m_1(x)$ and $m_2(x)$ are the axial variations of the magnetic currents on slot 1 and slot 2 and $K_{cv}^{P}(y,y')$, $G_d^{s1}(y,x',y')$ and $G_d^{s2}(y,x',y')$ are similar to terms defined in (2.19).

The expression for the electric field on the non-illuminated side (Fig. 5-1) of the final cavity screen is given below. The magnetic current in the last slot is determined by the use of the MoM solution procedure and one can compute the electric field, E_y, behind the final cavity screen from

$$E_y(x,y,z)=\frac{1}{2\pi}\int_{-L_n}^{L_n} m_n(x')\int_{y'=-w}^{y'=w}\frac{1/\pi}{\sqrt{w^2-y'^2}}\left[-z\frac{e^{-j\beta R}}{R^3}(j\beta R+1)\right]dy'dx', \quad (5.5)$$

where 'n' is the index of the slot current on the end wall. By expanding $m_n(x)$ in pulse basis functions, one can write E_y as

$$E_y(x,y,z)\approx\frac{1}{2\pi}\sum_{p=1}^{N} m_n^p(x')\int_{x_p-\Delta_s/2}^{x_p+\Delta_s/2}\int_{y'=-w}^{w}\frac{1/\pi}{\sqrt{w^2-y'^2}}\left[-z\frac{e^{-j\beta R}}{R^3}(j\beta R+1)\right]dy'dx'. \quad (5.6)$$

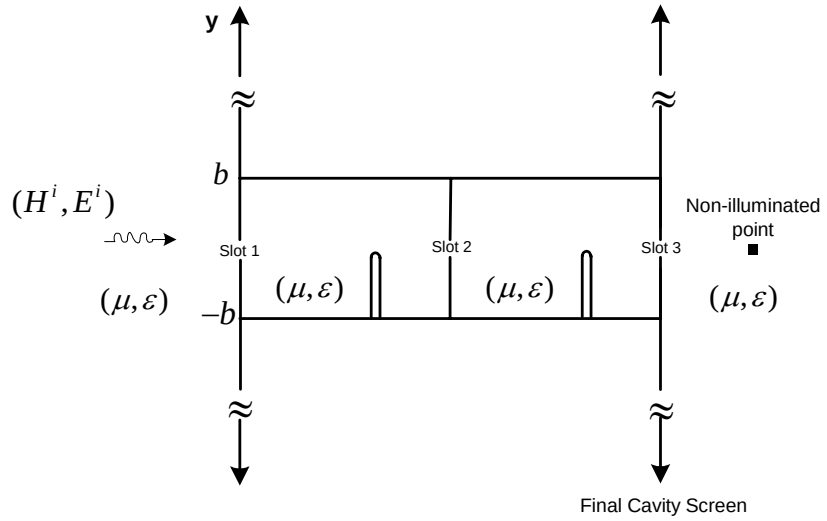

Fig. 5-1. Two cascaded rectangular cavities showing the non-illuminated point behind the last cavity screen.

As an investigation of the method devised to calculate EFS of a shielded enclosure, the shielding effectiveness of a single rectangular cavity with a narrow slot excited by a plane-wave source was computed and EFS plotted at the center of the cavity for a frequency range of 100 to 1000 MHz. The EFS plot was checked against results in [4] and [6] and found to agree well. A circuital approach to predict the field distributions on rectangular apertures backed by rectangular cavities is discussed by Azaro in [4] and the multilevel fast multipole method (MLFMM) algorithm is used for the computation of the EFS parameters by Volakis in [6].

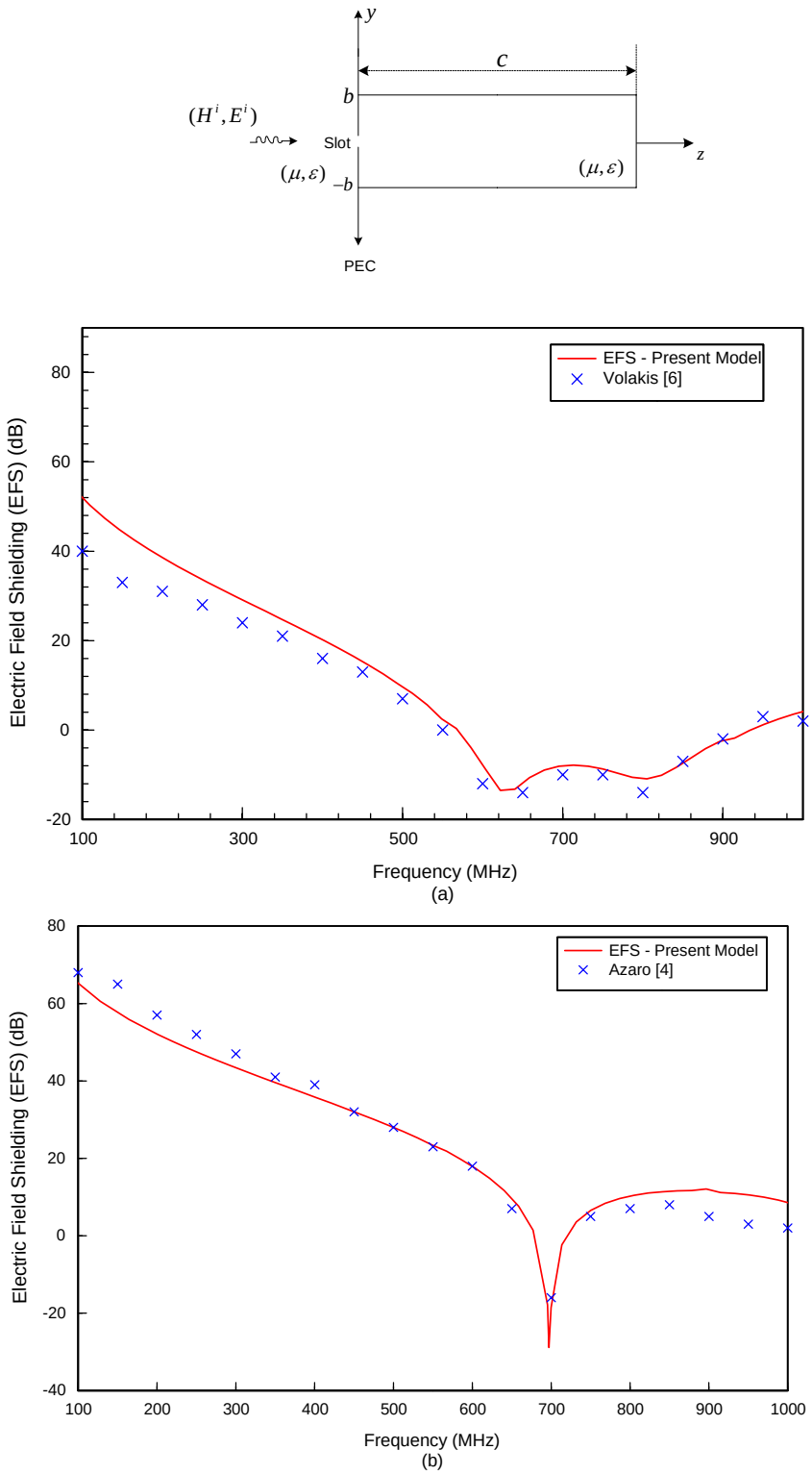

Fig. 5-2. Shielding effectiveness at the center of the rectangular cavity. Enclosure dimensions: 30 x 12 x 30 (cm). (a) Aperture dimensions: 20 x 3.0 (cm) (b) Aperture dimensions: 10 x 0.5 (cm)

The excitation used to illuminate the slot is shown in Fig. 5-3(a). It is a differentiated Gaussian pulse and its Fourier transform is shown in Fig. 5-3(b). The energy is centered around 1 GHz and only the positive frequencies are shown in the figure.

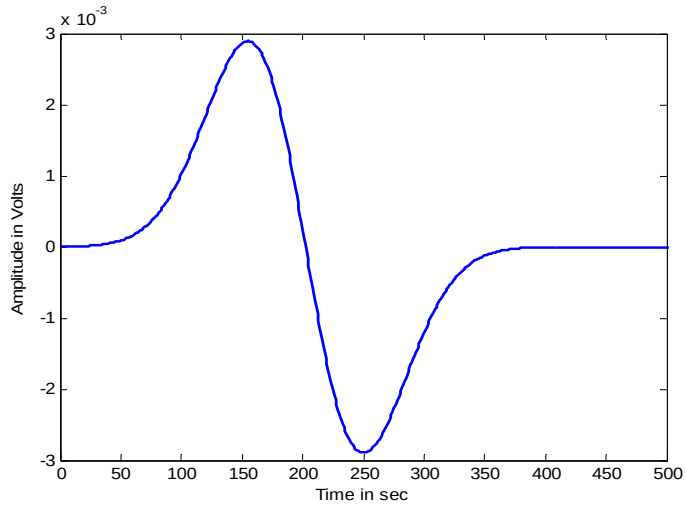

(a)

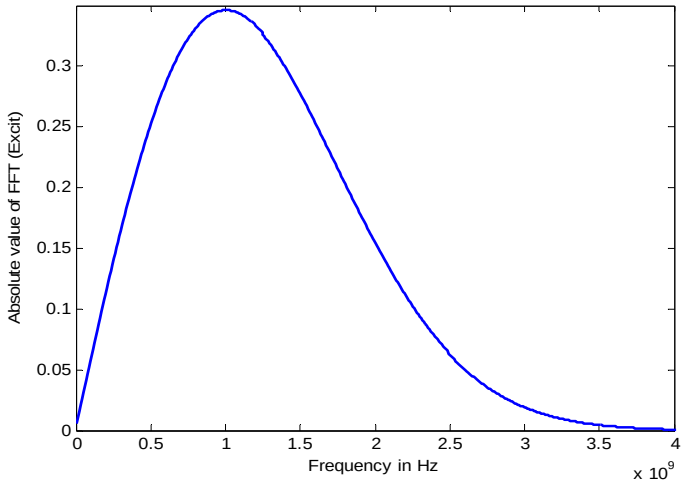

(b)

Fig. 5-3. (a) Differentiated Gaussian pulse excitation: $(n-n_0)\exp(-\left(\frac{n-n_o}{\tau}\right)^2)$ with $\tau = 67.45$ secs and $n_o = 3\tau$. (b) FFT spectrum (magnitude) of the differentiated Gaussian pulse with its energy centered around 1 GHz.

2. SINGLE RECTANGULAR CAVITY WITH A THIN-WIRE PROBE AND A NARROW SLOT

As shown in Fig. 5-4(a), the structure under examination is a narrow slot in an infinite PEC screen backed by a rectangular cavity with a thin-wire probe/post in it. The side view of the structure is illustrated in Fig. 5-4(b). As seen from the figure, it is a single rectangular cavity where the length of the thin-wire probe is h with its radius specified as r. The probe axis is located in the yz plane with d representing its displacement from the $z = 0$ plane. The slot length is $2L$ and the width is $2w$. The width, height, and depth of the cavity shown in the figure is $2a$, $2b$ and c, respectively. The medium inside and in the left half-space is characterized by (μ, ε).

The numerical results in the following pages show the input impedance of the slot and the probe for different structures. The input impedance is calculated from the magnetic currents and the electric currents which are obtained by solving the matrix equation as given in (2.37). The orientation of the thin-wire probe in the cavity and the orientation of the slot in the cavity do not allow the TE_{20p} and TE_{01p} modes to be excited in the cavity. One can find the modes excited by calculating the resonant frequency or the wavelength of each mode and examining the currents [5]. One finds that the TE_{101} mode is the lowest-order mode excited for each structure.

The real and imaginary parts of the input impedance at the center of the slot for Structure A are shown in Fig. 5-5. The upper limit of the frequency spectrum is 5 GHz. In the figure, one can see that the lowest-order TE_{101} mode is excited at about 3.78 GHz which is very close to the resonant frequency of this mode (3.40 GHz), as shown in Table 5.2. The resonance associated with the thin-wire probe is seen at about 2.58 GHz,

which is close to the resonance associated with the quarter-wave monopole (3.125 GHz), with a zero crossing in the imaginary part of the input impedance. The narrow-slot resonance is seen at about 4.19 GHz which is very close to the calculated resonance of 4.28 GHz.

Fig. 5-6 shows the real and imaginary parts of the input impedance computed at the center of the slot for Structure B with an upper frequency limit of 5 GHz. Examining the figure reveals that the lowest-order TE_{101} mode is excited at about 3.27 GHz which is very close to the resonant frequency of this mode (3.40 GHz) as shown in Table 5.2. The figure also shows that the resonance associated with the narrow slot is seen at about 4.37 GHz which is close to the calculated resonance of 4.28 GHz.

Table 5.3 shows parameters for Structure C for which the input impedance at the center of the slot and at the base of the thin-wire probe is computed by driving them separately. The slot is excited with the frequency spectrum obtained from the FFT of a differentiated Gaussian pulse as described in Fig. 5-3(b) and the probe is fed with a 1.0 V source at its base. The EFS for the structure is computed at the center of the cavity using (5.1). In the Fig. 5-7, one can see that the lowest-order mode, TE_{101}, is excited at about 3.41 GHz, which is very close to the resonant frequency of this mode (3.40 GHz), as shown in Table 5.4. The resonance associated with the thin-wire probe is seen at about 2.44 GHz, which is close to the resonance associated with the quarter-wave monopole (2.67 GHz), with a zero crossing in the imaginary part of the input impedance. The narrow-slot resonance is seen at about 4.29 GHz which is extremely close to the calculated resonance of 4.28 GHz. The input impedance at the base of the probe is shown in Fig. 5-8. The resonances associated with the cavity, slot and the probe are very

clearly defined at the same frequencies as seen for the slot impedance. The EFS is computed at the center of the cavity using (5.1). The plot (Fig. 5-9) shows that EFS decreases in the neighborhood of the resonances as expected.

Fig. 5-10 shows the real and imaginary parts of the input impedance computed at the center of the slot for Structure D with an upper frequency limit of $5\ \text{GHz}$. The same driving mechanism is used as described in the previous section. As the figure shows, the lowest-order mode, TE_{101}, is excited at about $4.22\ \text{GHz}$ which is close to the resonant frequency of this mode ($3.86\ \text{GHz}$), as shown in Table 5.4. The figure also shows that the resonance associated with the narrow slot is seen at about $3.01\ \text{GHz}$ which is extremely close to the calculated resonance of $3.0\ \text{GHz}$. The resonance associated with the thin-wire probe is seen at about $1.84\ \text{GHz}$, which is close to the resonance associated with the quarter-wave monopole ($2.08\ \text{GHz}$). The EFS plot (Fig. 5-11) shows that the shielding effectiveness decreases near $1.84\ \text{GHz}$, $3.11\ \text{GHz}$, and $4.24\ \text{GHz}$ which corresponds to the three resonances captured in the impedance plots.

TABLE 5.1
STRUCTURE PARAMETERS

Parameter*	**Structure A**	**Structure B**
Cavity width, $2a$	60.0	60.0
Cavity height, $2b$	34.0	32.0
Cavity depth, c	65.0	65.0
Slot length, $2L$	35.0	35.0
Slot width, $2w$	0.5	0.5
Probe length, h	24.0	12.0
Probe radius, r	0.25	0.25
Probe position, d	20.0	20.0

*All parameters are in millimeters

TABLE 5.2
RESONANT FREQUENCIES**

	Structure A	**Structure B**
TE_{101}	3.40	3.40
TE_{102}	5.25	5.25
TE_{103}	7.36	7.36
TE_{201}	5.5	5.5
TE_{104}	9.56	9.56
Probe half-wave resonance	3.125	6.25
Slot half-wave resonance	4.28	4.28

*All frequencies are in GHz.

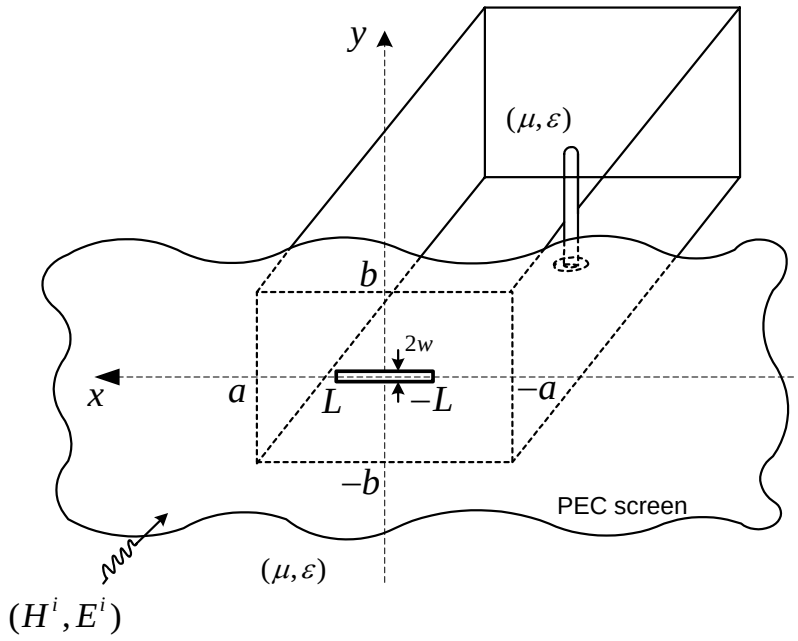

(a)

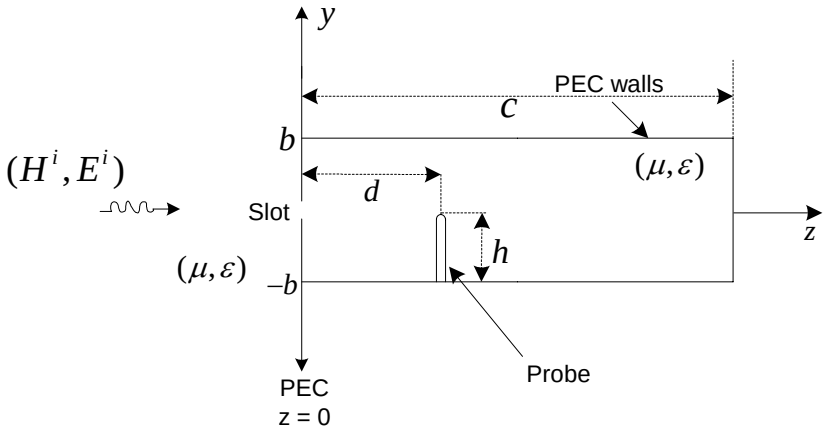

(b)

Fig. 5-4. A narrow slot in an infinite PEC screen backed by a rectangular cavity with a thin-wire probe in it. (a) perspective view (b) side view

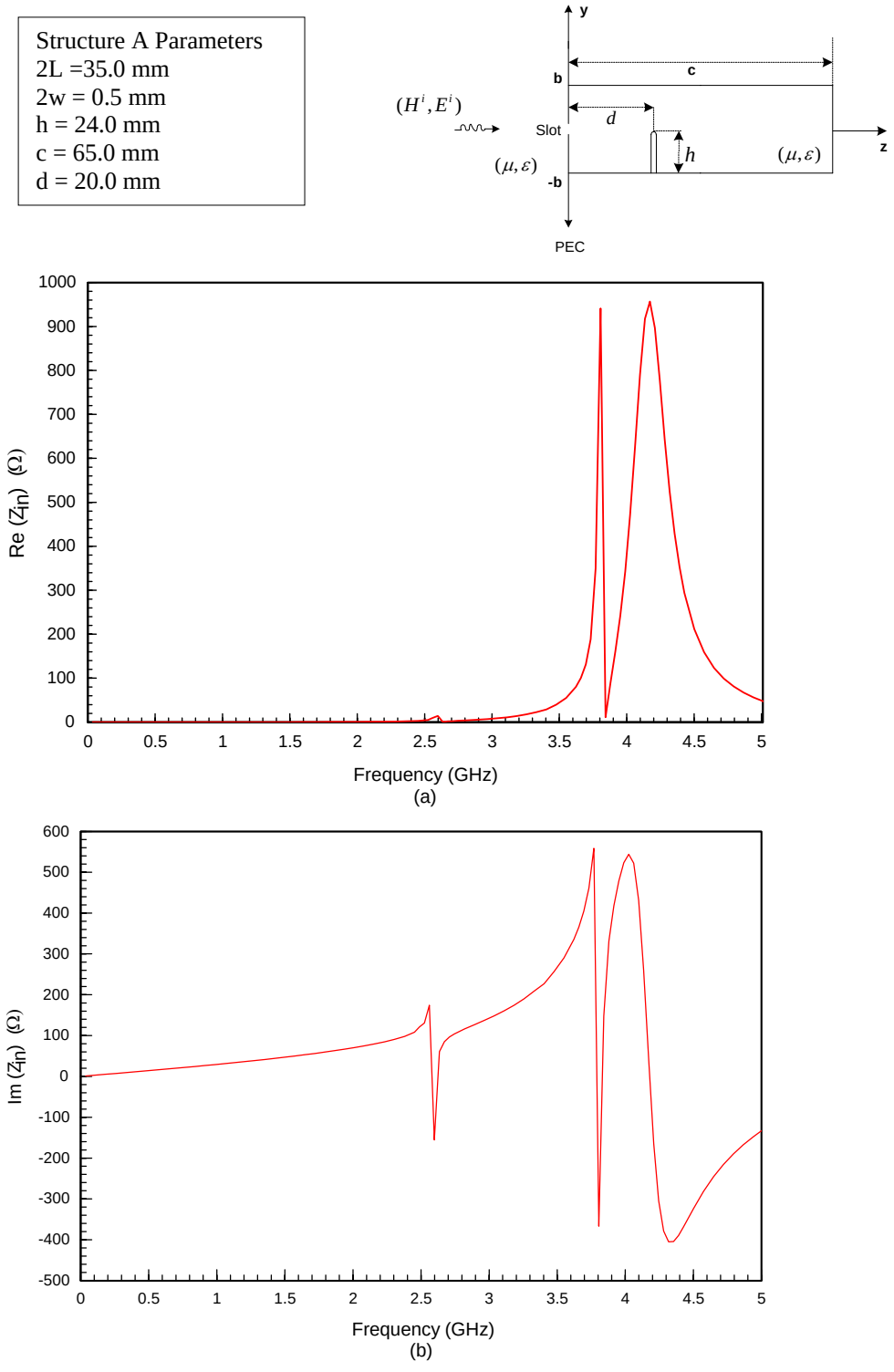

Fig. 5-5. Input impedance at the center of the slot. (a) Real part of impedance. (b) Imaginary part of impedance.

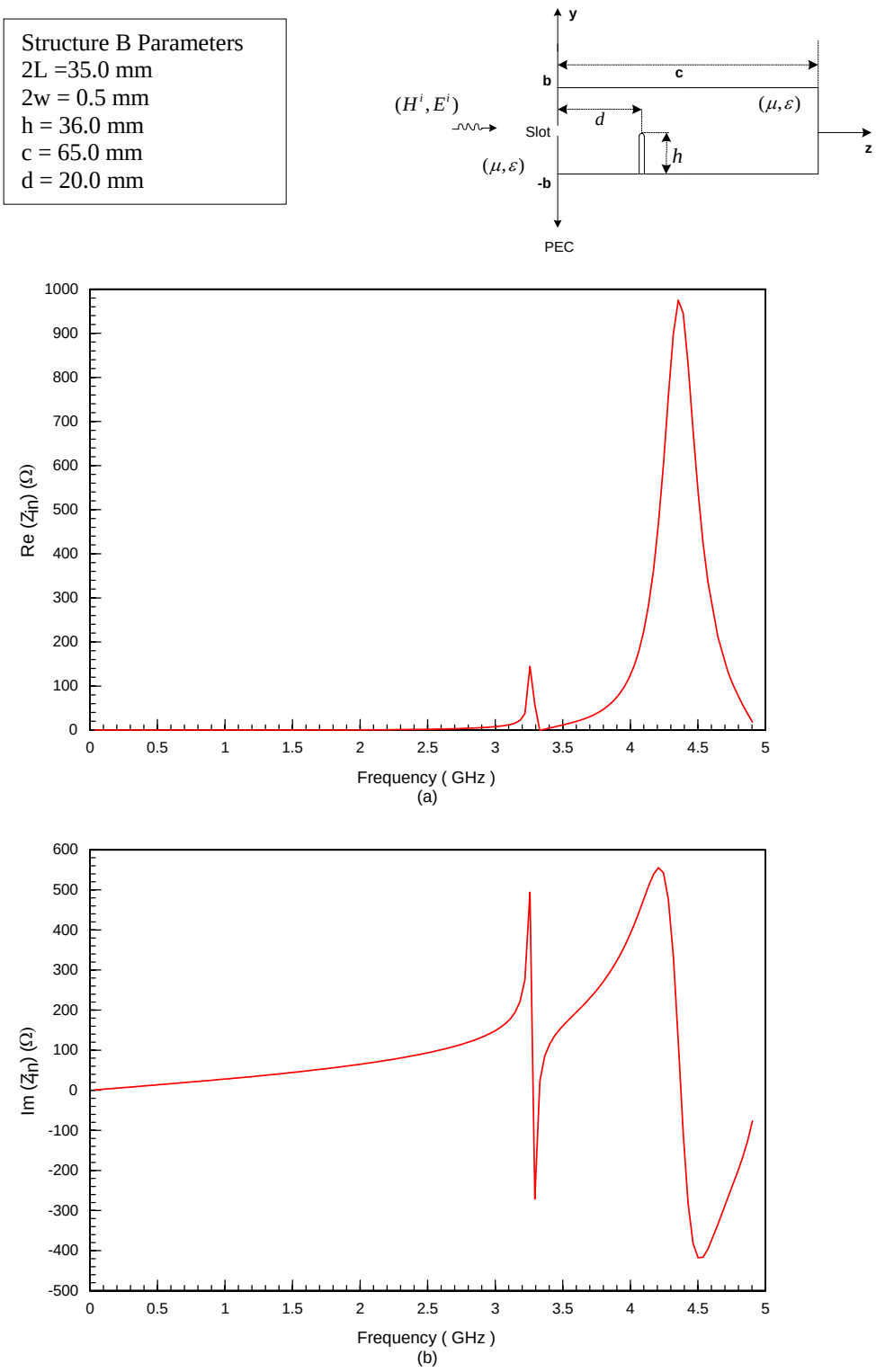

Fig. 5-6. Input impedance at the center of the slot. (a) Real part of impedance. (b) Imaginary part of impedance.

TABLE 5.3
STRUCTURE PARAMETERS

Parameter	Structure C (mm)	Structure D (mm)
Cavity width, $2a$	60.0	53.0
Cavity height, $2b$	34.0	40.0
Cavity depth, c	65.0	58.0
Slot length, $2L$	35.0	50.0
Slot width, $2w$	0.5	0.5
Probe length, h	28.0	36.0
Probe radius, r	0.25	0.25
Probe position, d	4.0	20.0

TABLE 5.4
RESONANT FREQUENCIES**

	Structure C	Structure D
TE_{101}	3.40	3.86
TE_{102}	5.25	5.87
TE_{103}	7.36	7.36
TE_{201}	5.5	5.5
TE_{104}	9.56	9.56
Probe half-wave resonance	2.67	2.08
Slot half-wave resonance	4.28	3.00

** All Frequencies are in GHz

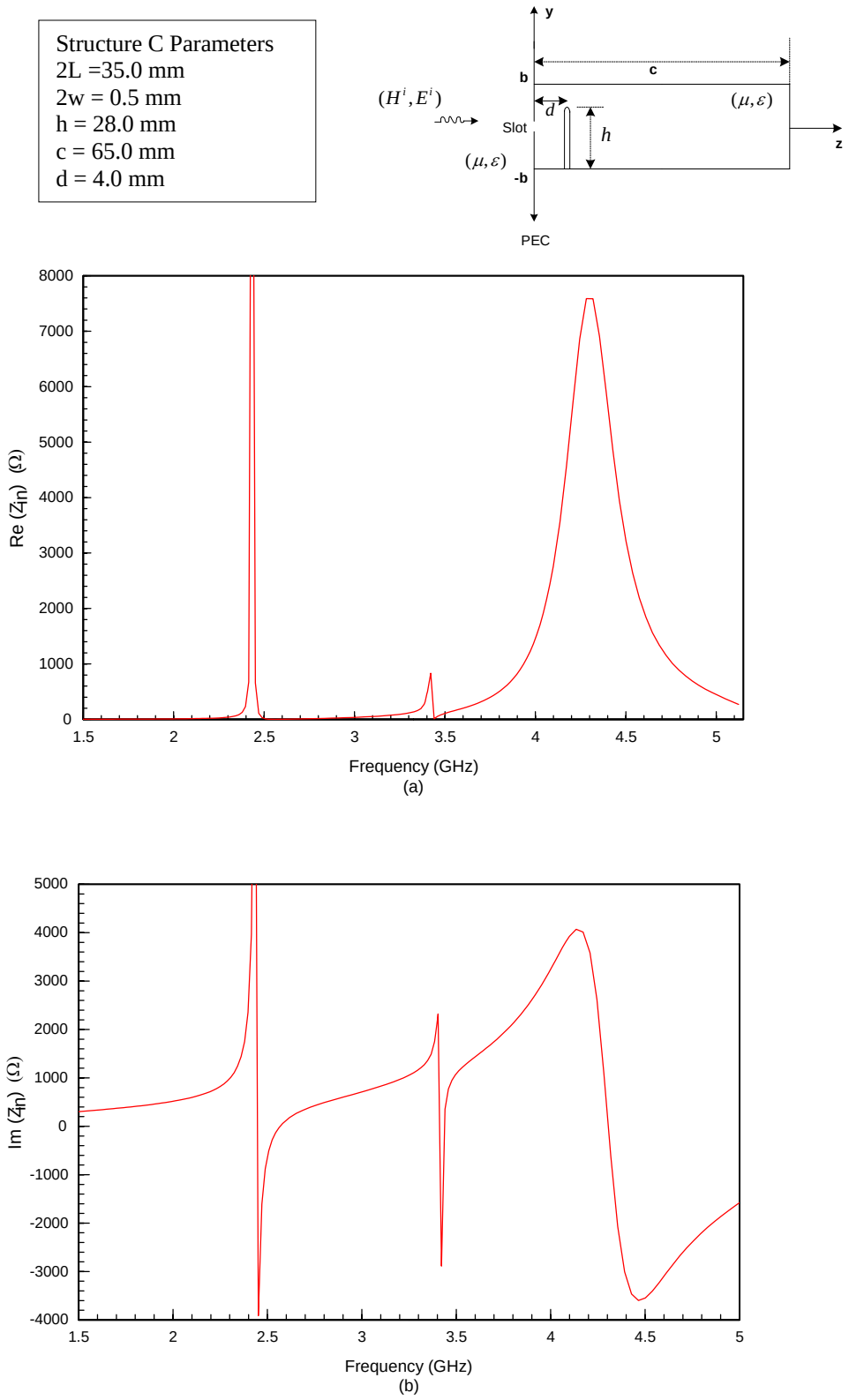

Fig. 5-7. Input impedance at the center of the slot. (a) Real part of impedance. (b) Imaginary part of impedance.

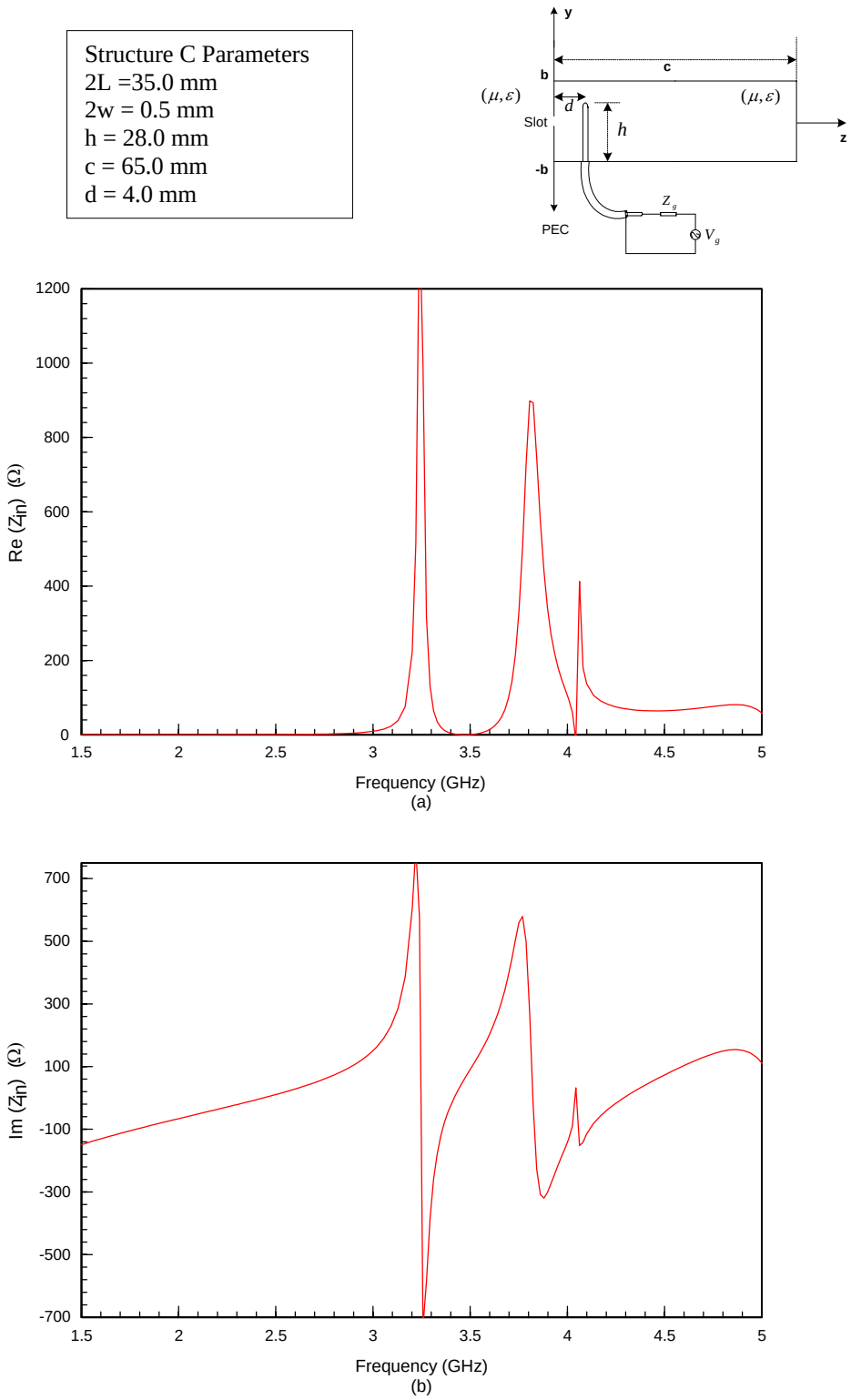

Fig. 5-8. Input impedance at the base of the probe. (a) Real part of impedance (b) Imaginary part of impedance.

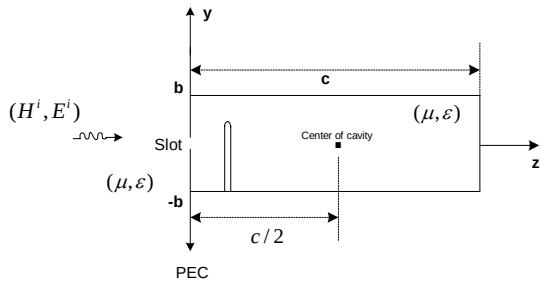

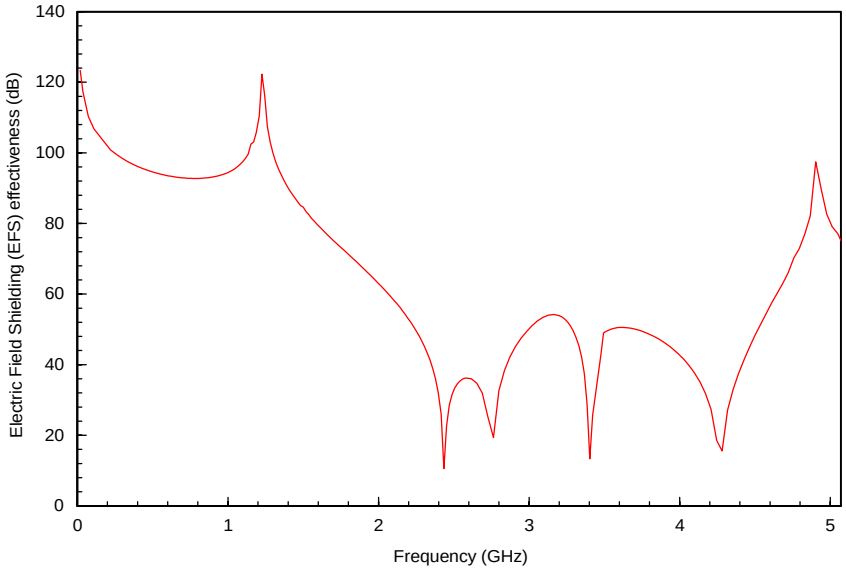

Fig. 5-9. EFS at the center of the rectangular cavity for Structure C.

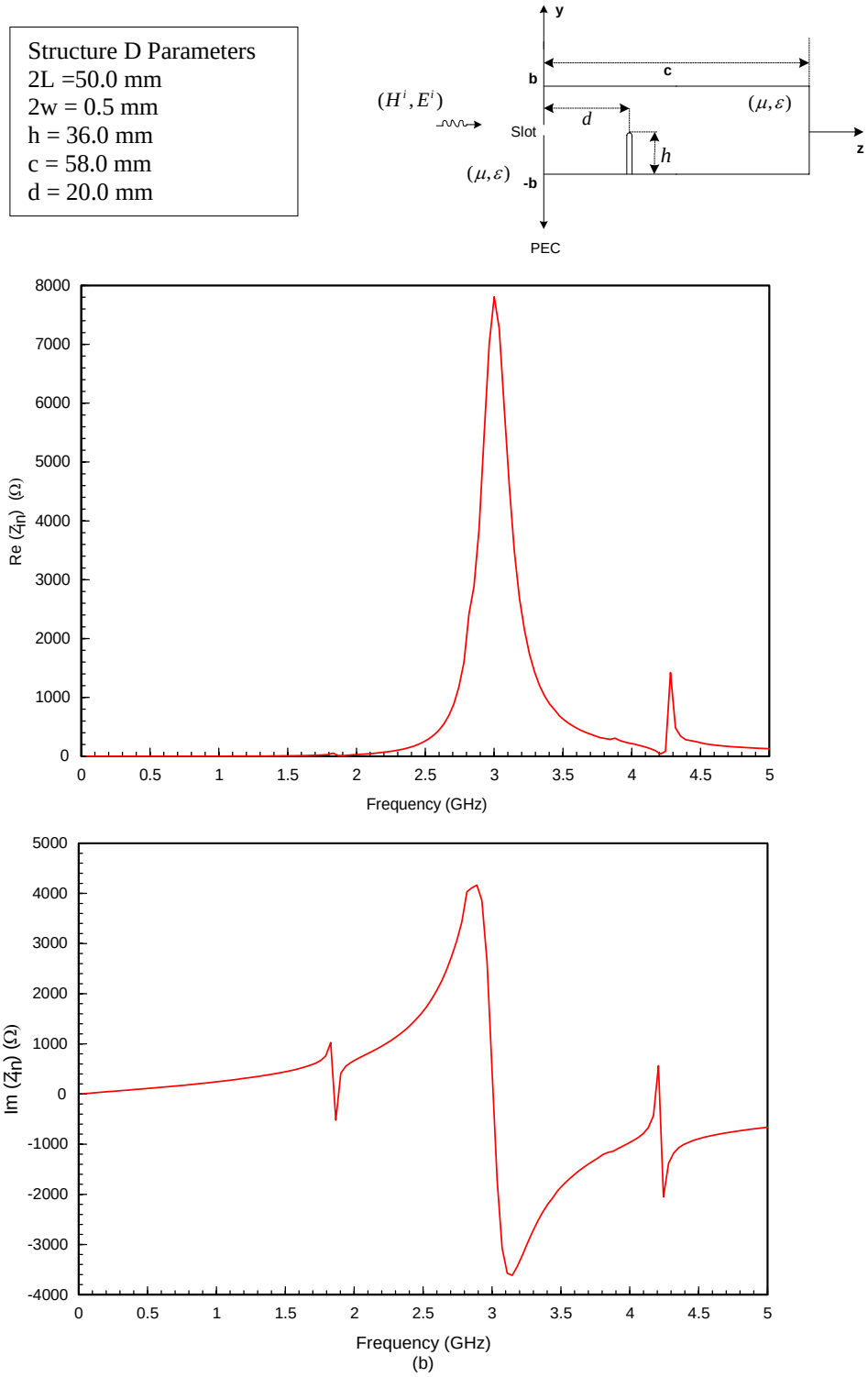

Fig. 5-10. Input impedance at the center of the slot. (a) Real part of impedance (b) Imaginary part of impedance.

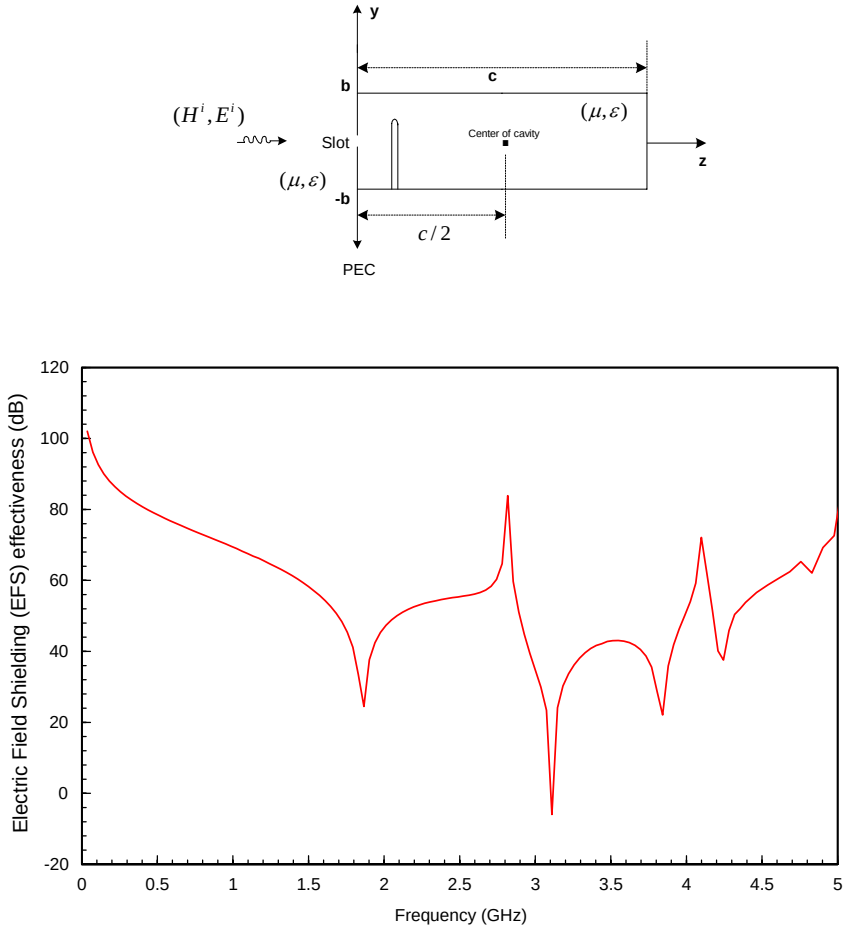

Fig. 5-11. EFS at the center of the rectangular cavity for Structure D.

3. Two Cascaded Rectangular Cavities Interconnected By A Narrow Slot With Thin-Wire Probes Inside

As shown in Fig. 5-12, the structure under examination is a narrow slot in an infinite PEC screen backed by two cascaded rectangular cavities each having a thin-wire probe/post inside and which are interconnected by a narrow slot. The lengths of the thin-wire probes are h_1 and h_2 with their radii specified as r. The probe axes are located in the yz plane with d_1 and $c+d_2$ representing their displacement from the $z=0$ plane. The slot lengths are $2L_1$, $2L_2$ and $2L_3$ respectively and their widths are $2w$ for all the slots. The width, height, and depth of each cavity shown in the figure is $2a$, $2b$ and c. The medium inside each cavity, in the left half-space where $z<0$ and in the right-half space where $z>2c$ is characterized by (μ,ε).

The numerical procedure was first tested by computing the electric and magnetic currents on the probes and the slots for a symmetrical structure which is excited at the second (middle) slot. The currents are shown in Fig. 5-13. The magnetic current on slot 1 and slot 3 and the electric current on probe 1 and probe 2 are plotted. From the figure it is seen that the agreement between the slot currents and the probe currents is very good at the given frequency, which is to be expected. Though this method is not a foolproof validation of the numerical process, it serves as a partial validation of the numerical results.

Table 5.4 shows parameters for Structure E for which input impedance at the center of slot 1 and at the base of probe 1 in the first cavity is computed by driving them separately. The frequency spectrum obtained from the FFT of a differentiated Gaussian pulse as defined in Fig. 5-3(b) is used to excite the narrow slot and the probe is fed with a

1.0 V source at its base. The EFS for the structure is computed at the center of each cavity using (5.1). In the Fig. 5-14, one can see that the lowest-order mode, TE_{101}, is excited at about $3.38\ \text{GHz}$ which is extremely close to the resonant frequency of this mode ($3.40\ \text{GHz}$), as shown in Table 5.4. The resonance associated with the thin-wire probe is seen at about $2.43\ \text{GHz}$, which is close to the resonance associated with the quarter-wave monopole ($2.67\ \text{GHz}$), where a zero crossing in the imaginary part of the input impedance is seen. The narrow-slot resonance is seen at about $4.26\ \text{GHz}$, which is extremely close to the calculated resonance of $4.28\ \text{GHz}$. The resonance of the second slot (slot 2) is seen at $4.41\ \text{GHz}$ and the resonance of the third slot (slot 3), though not properly excited, exists at around $4.58\ \text{GHz}$. The input impedance at the base of the probe is shown in Fig. 5-15. The resonances associated with the cavity, slot, and the probe are very clearly defined at the same frequencies as seen for the slot impedance. The EFS is computed at the center of each cavity ($z = c/2$, $z = 3c/2$ and $z = 5c/2$) using (5.1). Equation (5.6) is used to compute E_y at $z = 5c/2$. The plot shows that EFS (Fig. 5-16) decreases in the neighborhood of the resonances, as expected.

Fig. 5-17 shows the real and imaginary parts of the input impedance computed at the center of the slot for Structure F with an upper frequency limit of $5\ \text{GHz}$. Examining the figure reveals that the lowest-order mode, TE_{101}, is excited at about $4.22\ \text{GHz}$ which is close to the resonant frequency of this mode ($3.86\ \text{GHz}$), as shown in Table 5.4. The resonance of the second cavity is seen to be excited slightly at about $4.35\ \text{GHz}$. The figure also shows that the resonance associated with the narrow slot is seen at $3.01\ \text{GHz}$, which is extremely close to the calculated resonance of $3.0\ \text{GHz}$. The resonance of slot 2 is seen at $3.11\ \text{GHz}$. The resonance of slot 3 is not properly excited and hence is not seen

in the figure. The resonance associated with the thin-wire probe is seen at about 1.84 GHz, which is close to the resonance associated with the quarter-wave monopole (2.08 GHz). The EFS plot in Fig. 5-18 shows that the shielding effectiveness decreases near 1.84 GHz, 3.11 GHz, and 4.22 GHz, which corresponds to the three resonances captured in the impedance plots.

TABLE 5.3
STRUCTURE PARAMETERS

Parameter	Structure E (mm)	Structure F (mm)
Cavity width, $2a$	60.0	53.0
Cavity height, $2b$	34.0	40.0
Cavity depth, c	65.0	58.0
Slot length, $2L_1$, $2L_2$, $2L_3$	35.0	50.0
Slot width, $2w$	0.5	0.5
Probe length, h_1, h_2	28.0	36.0
Probe radius, r	0.25	0.25
Probe position, d_1, d_2	4.0	20.0

TABLE 5.4
RESONANT FREQUENCIES**

	Structure E	Structure F
TE_{101}	3.40	3.86
TE_{102}	5.25	5.87
TE_{103}	7.36	7.36
TE_{201}	5.5	5.5
TE_{104}	9.56	9.56
Probe half-wave resonance	2.67	2.08
Slot half-wave resonance	4.28	3.00

** All Frequencies are in GHz

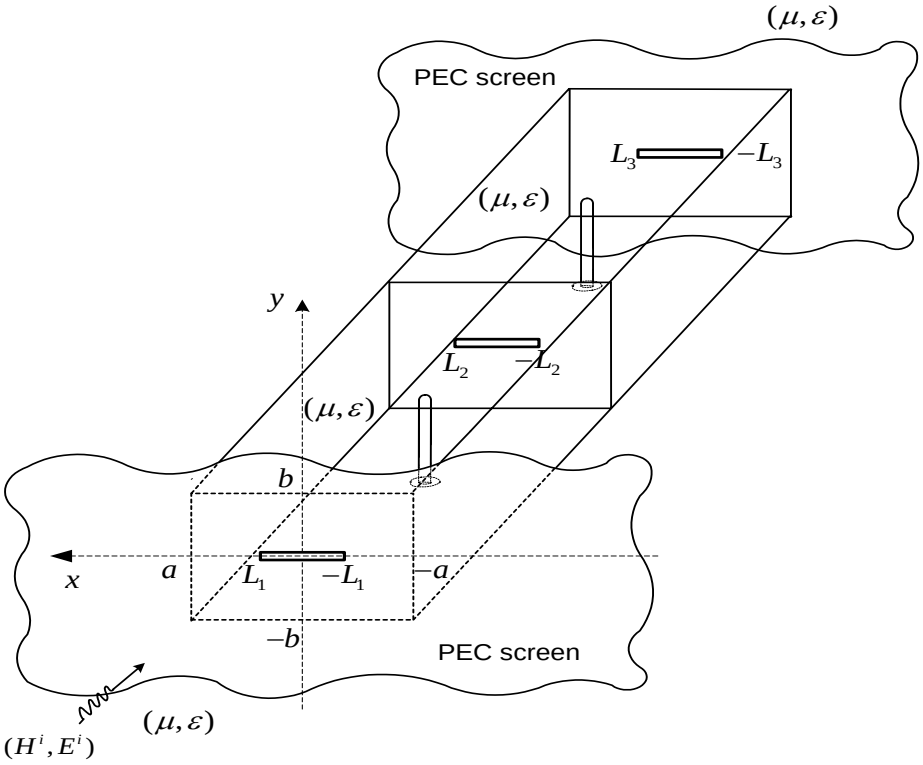

(a)

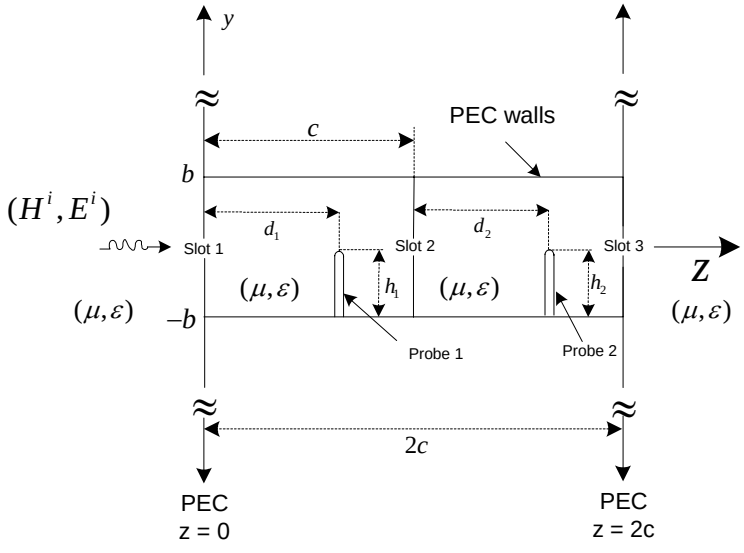

(b)

Fig. 5-12. Two cascaded rectangular cavities interconnected by a narrow slot and with thin-wire probes in them. (a) perspective view. (b) side view.

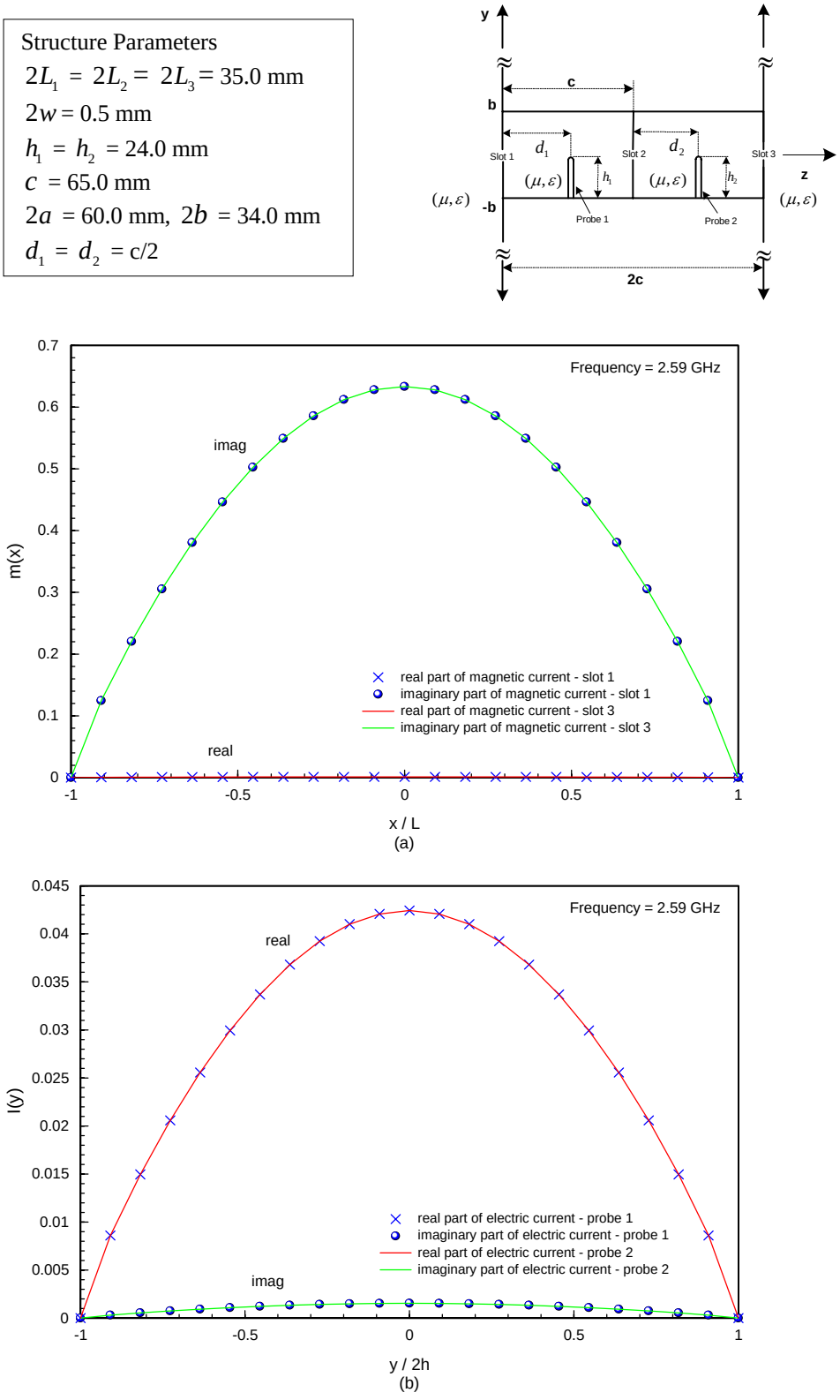

Fig. 5-13. Magnetic currents in the slots and electric currents on the probes due to a 1.0 V excitation on slot 2 (a) Magnetic currents in slot 1 and slot 3 (b) Electric currents on probe 1 and probe 2.

Structure E Parameters

$2L_1 = 2L_2 = 2L_3 = 35.0$ mm

$2w = 0.5$ mm

$h_1 = h_2 = 28.0$ mm

c = 65.0 mm

$d_1 = d_2 = 4.0$ mm

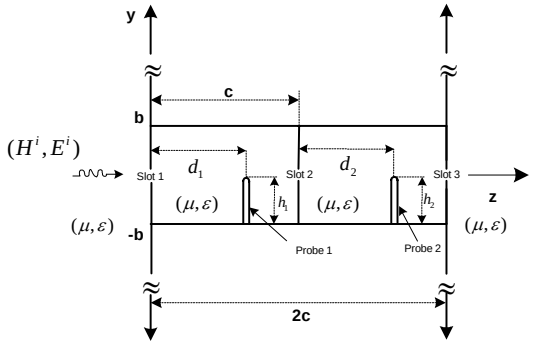

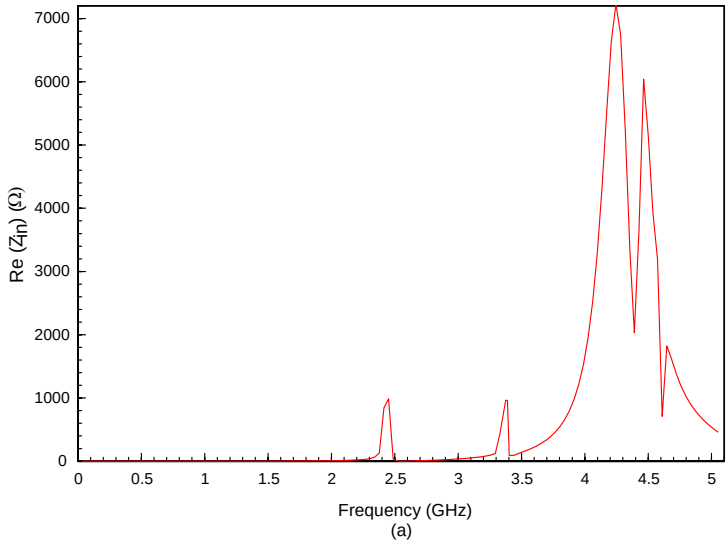

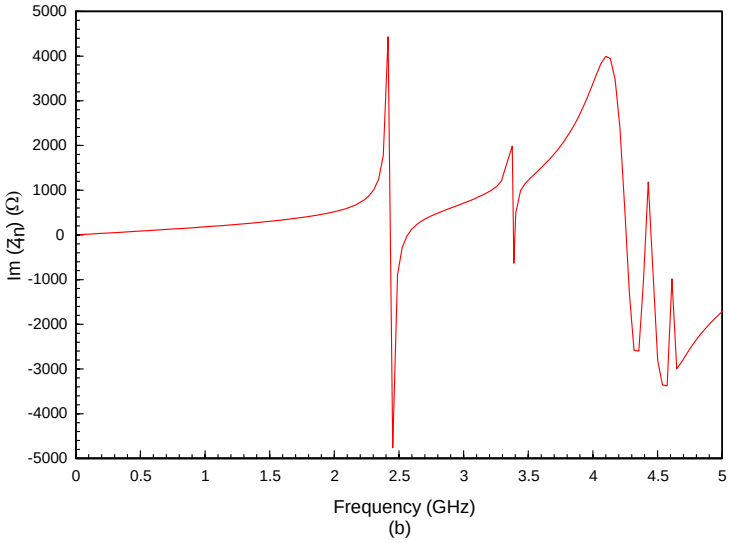

Fig. 5-14. Input impedance at the center of slot 1. (a) Real part of impedance. (b) Imaginary part of impedance.

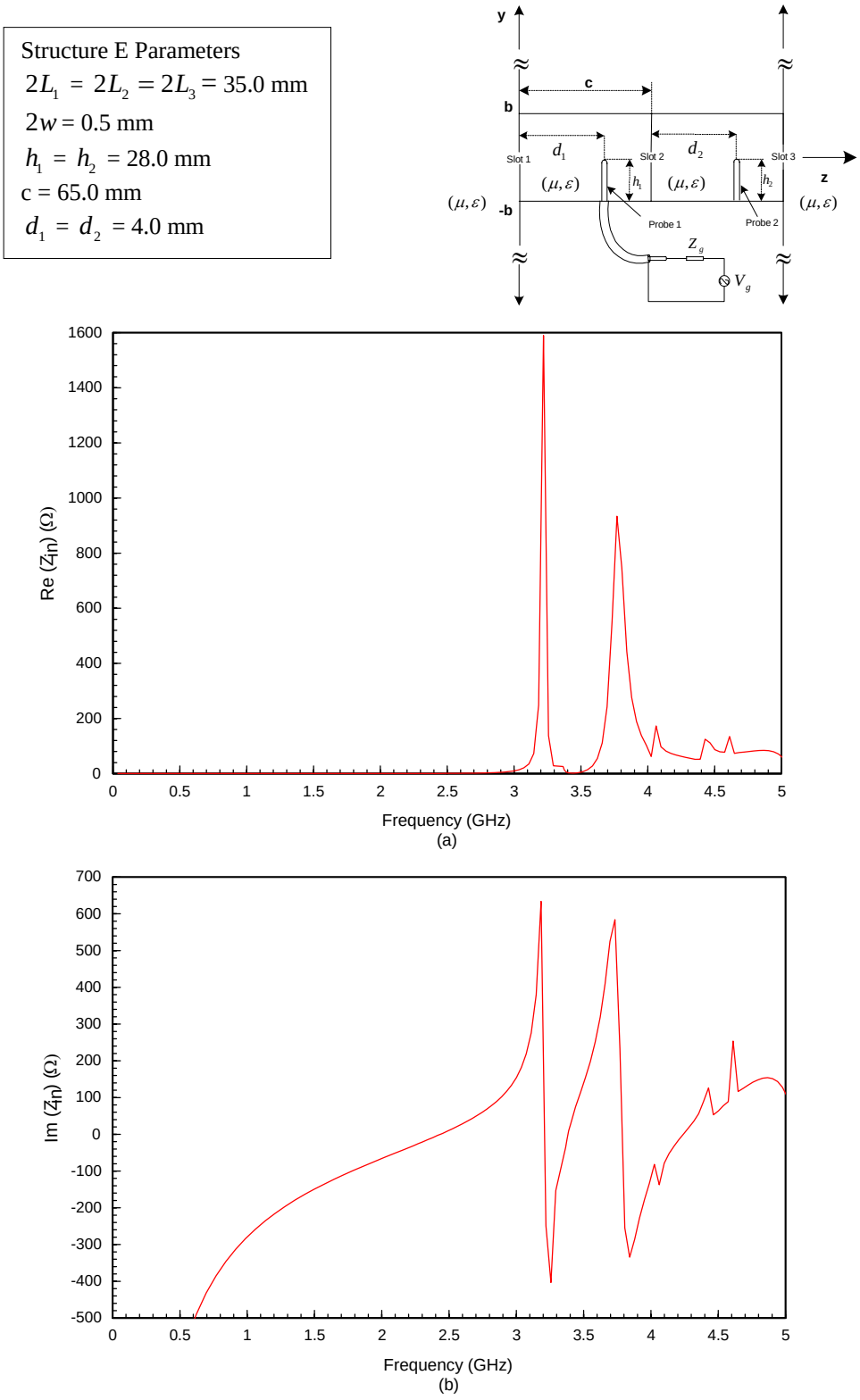

Fig. 5-15. Input impedance at the base of probe 1. (a) Real part of impedance. (b) Imaginary part of impedance.

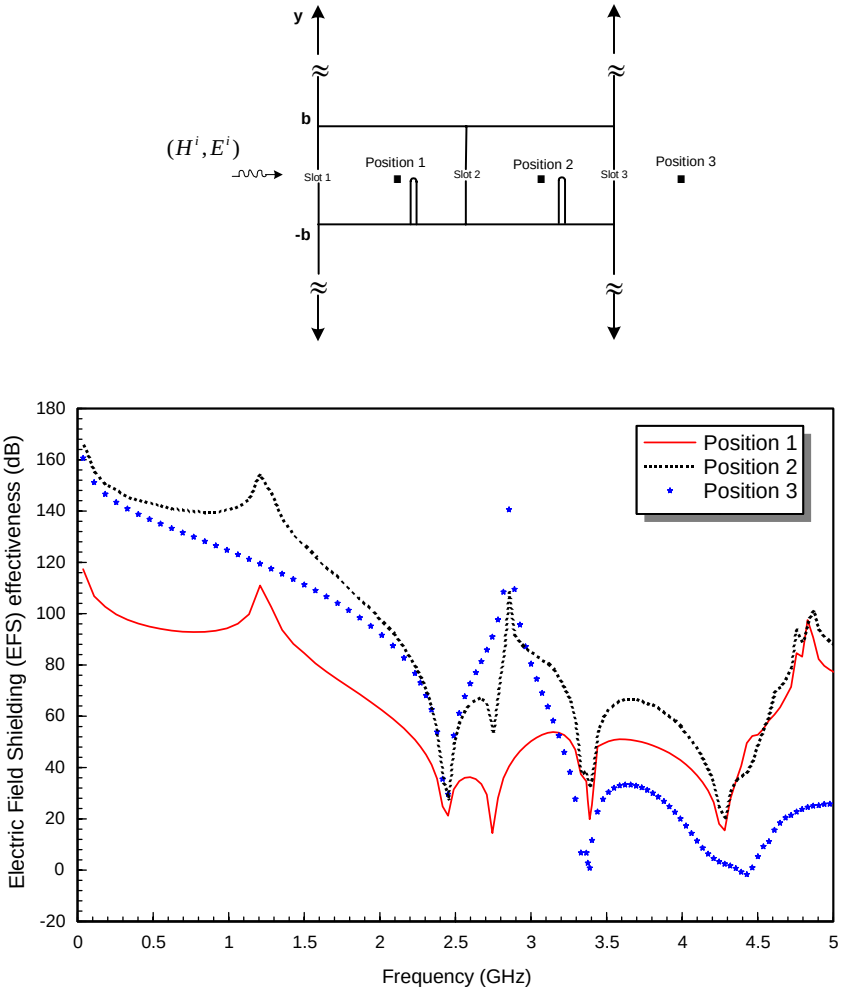

Fig. 5-16. EFS for Structure E.

Structure F Parameters

$2L_1 = 2L_2 = 2L_3 = 50.0$ mm

$2w = 0.5$ mm

$h_1 = h_2 = 36.0$ mm

c = 58.0 mm

$d_1 = d_2 = 20.0$ mm

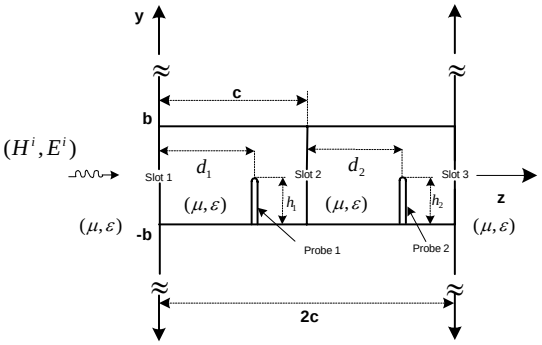

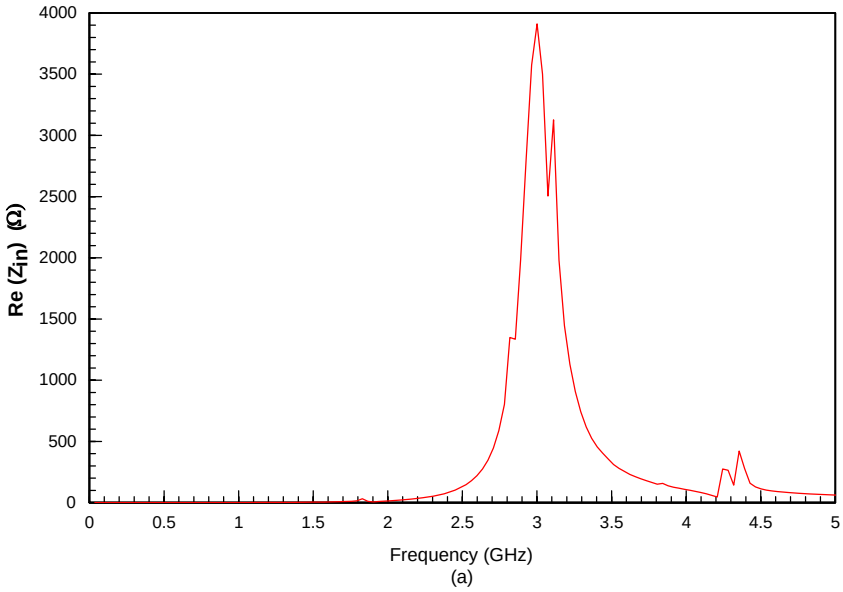

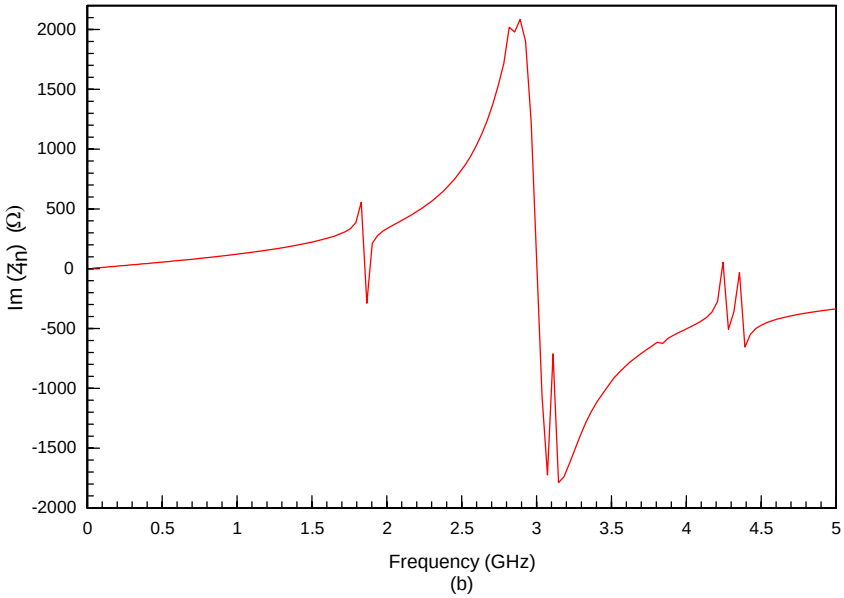

Fig. 5-17. Input impedance at the center of slot 1. (a) Real part of impedance. (b) Imaginary part of impedance.

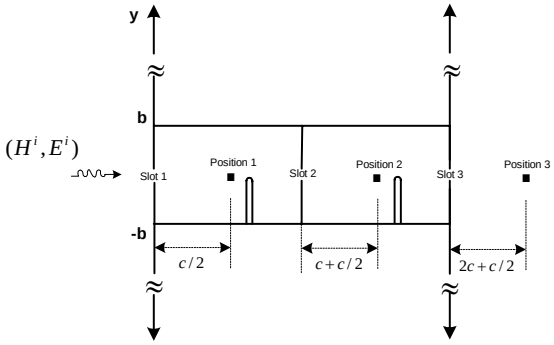

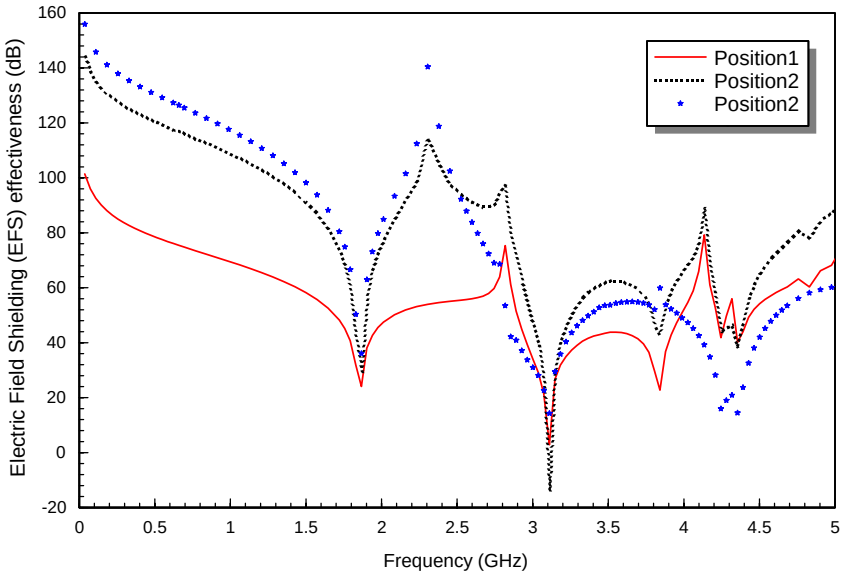

Fig. 5-18. EFS for Structure F.

4. THREE CASCADED RECTANGULAR CAVITIES INTERCONNECTED BY NARROW SLOTS WITH THIN-WIRE PROBES INSIDE

As shown in Fig. 5-19, the structure under examination is a narrow slot in an infinite PEC screen backed by triply cascaded rectangular cavities, each with a thin-wire probe/post in it and which are interconnected by narrow slots. As seen from the figure, the structure is a triply cascaded rectangular cavity where the lengths of the thin-wire probes are h_1, h_2 and h_3 with their radii specified as r. The probe axes are located in the yz plane with d_1, $c+d_2$ and $2c+d_3$ representing their displacement from the $z=0$ plane. The slot lengths are $2L_1$, $2L_2$, $2L_3$ and $2L_4$ respectively and their widths are $2w$ for all the slots. The width, height, and depth of each of the cavity shown in the figure is $2a$, $2b$ and c, respectively. The medium inside each cavity, in the left half-space and in the right-half space, is characterized by (μ,ε).

The numerical procedure was first tested by computing the electric and magnetic currents on the probes and the slots for a symmetrical structure which was excited at the second (middle) probe. The currents are shown in Fig. 5-20. The equivalent magnetic currents in slot 1 and slot 4 are plotted in Fig. 5-20(a) and in slot 2 and slot 3 are plotted in Fig. 5-20(b). The electric currents on probe 1 and probe 3 are plotted in Fig. 5-20(c). From the figure it is seen that the agreement between the slot currents and the probe currents is very good at the given frequency which is to be expected. As stated earlier, this method enables us to partially validate the numerical results even if not completely endorsing it.

Table 5.5 shows parameters for Structure G for which input impedance at the center of slot 1 and at the base of probe 2 in the second cavity is computed by driving

them separately. The slot is excited by the frequency spectrum obtained from the FFT of the differentiated Gaussian pulse (Fig. 5-3(b)) and the probe is driven by a 1.0 V source applied at its base. The EFS for the structure is computed at the center of each cavity to predict the influence of the transmission path on the transient signal. One can see from the Fig. 5-21 that the lowest-order mode, TE_{101}, is excited at about $3.38\ \text{GHz}$ which is extremely close to the resonant frequency of this mode ($3.40\ \text{GHz}$), as shown in Table 5.6. Also, the thin-wire probe resonance is seen at about $2.43\ \text{GHz}$, which is close to the theoretically [5] calculated value of $2.67\ \text{GHz}$. Examining the figure, the resonances of the different slots are seen near 4.48 GHz, which is the calculated value. The resonance of slot 1 is seen at $4.22\ \text{GHz}$, the resonance of slot 2 is seen at $4.37\ \text{GHz}$, the resonance associated with slot 3 exists at about $4.48\ \text{GHz}$ and the resonance of slot 4 occurs at $4.59\ \text{GHz}$. The input impedance at the base of the probe is shown in Fig. 5-22. The resonances associated with the cavity, slot and the probe are very clearly defined at the same frequencies as seen for the slot impedance. The EFS (Fig. 5-23) is computed at the center of each cavity ($z = c/2$, $z = 3c/2$, $z = 5c/2$ and $z = 7c/2$) using (5.1). The equation (5.6) is used to compute E_y at $z = 7c/2$. The plot shows that EFS decreases in the neighborhood of the resonances as expected. The EFS decreases near the vicinity of $2.41\ \text{GHz}$, $3.40\ \text{GHz}$, and $4.31\ \text{GHz}$ corresponding to the calculated resonances.

The real and imaginary parts of the input impedance at the center of slot 1 and base of probe 2 for Structure H in the frequency range between 6 GHz and 12 GHz are computed by following the same driving mechanism as explained in the previous section. Examining Fig. 5-24, the input impedance at the center of slot 1 is plotted and the TE_{101} mode is excited at around $4.20\ \text{GHz}$, which is close to the resonant frequency of this

mode ($3.86\,\text{GHz}$). One can also see a slight change in the input impedance at this frequency. It can also be seen from the figure that the resonance associated with the thin-wire probe occurs at about $1.84\,\text{GHz}$, which is close to the theoretical value of $2.08\,\text{GHz}$. The resonance associated with slot 1 occurs at about $3.02\,\text{GHz}$ which is extremely close to the calculated resonance of $3.0\,\text{GHz}$. The resonance of the second slot is seen at $3.07\,\text{GHz}$ while the resonances associated with slot 3 and slot 4 are not properly excited in this structure. The input impedance at the base of the probe is shown in Fig. 5-25 for a 1.0 V excitation at its base. The resonances associated with the cavity, slot, and the probe are very clearly defined at the same frequencies as seen for the slot impedance. The EFS (Fig. 5-26) is computed at the center of each cavity ($z = c/2$, $z = 3c/2$, $z = 5c/2$ and $z = 7c/2$) using (5.1) for Structure H. Again, equation (5.6) is used to compute E_y at $z = 7c/2$. The plot shows that EFS decreases in the neighborhood of the resonances, as expected.

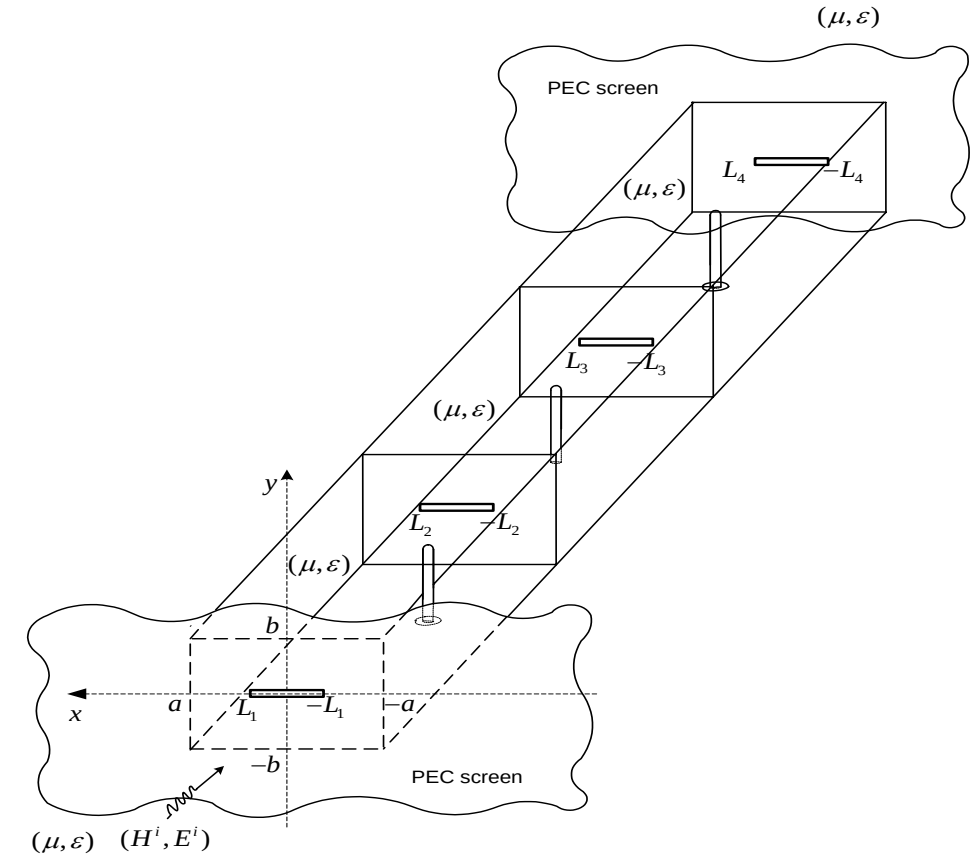

(a)

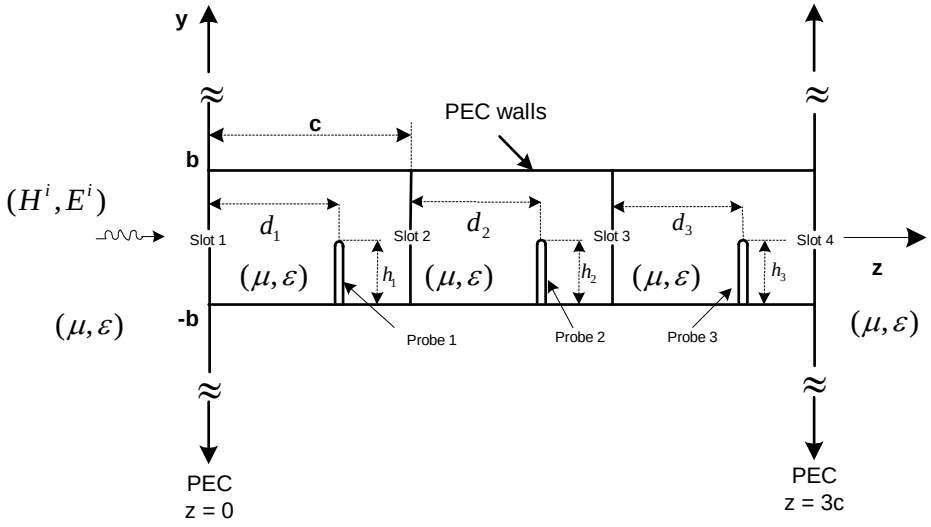

(b)

Fig. 5-19. Three cascaded rectangular cavities interconnected by narrow slots and with thin-wire probes in them. (a) perspective view. (b) side view.

TABLE 5.5
STRUCTURE PARAMETERS

Parameter	Structure G (mm)	Structure H (mm)
Cavity width, $2a$	60.0	53.0
Cavity height, $2b$	34.0	40.0
Cavity depth, c	65.0	58.0
Slot lengths, $2L_1$, $2L_2$, $2L_3$, $2L_4$	35.0	50.0
Slot width, $2w$	0.5	0.5
Probe lengths, h_1, h_2, h_3	28.0	36.0
Probe radius, r	0.25	0.25
Probe position, d_1, d_2, d_3	4.0	20.0

TABLE 5.6
RESONANT FREQUENCIES**

	Structure G	Structure H
TE_{101}	3.40	3.86
TE_{102}	5.25	5.87
TE_{103}	7.36	7.36
TE_{201}	5.5	5.5
TE_{104}	9.56	9.56
Probe half-wave resonance	2.67	2.08
Slot half-wave resonance	4.28	3.00

** All Frequencies are in GHz

Structure Parameters

$2L_1 = 2L_2 = 2L_3 = 2L_4 = 35.0$ mm

$2w = 0.5$ mm

$h_1 = h_2 = h_3 = 24.0$ mm

$c = 65.0$ mm

$2a = 60.0$ mm, $2b = 34.0$ mm

$d_1 = d_2 = d_3 = c/2$

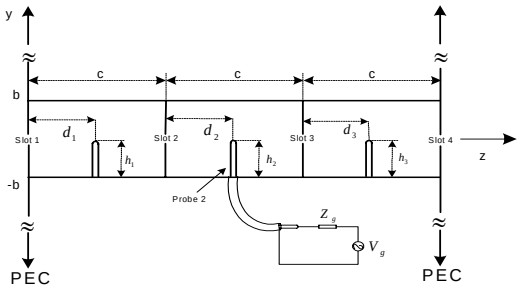

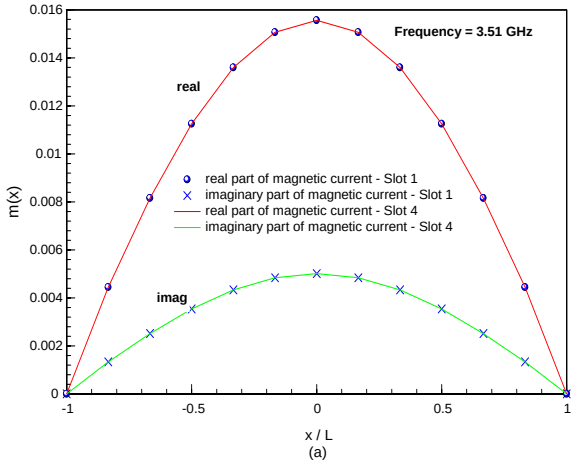

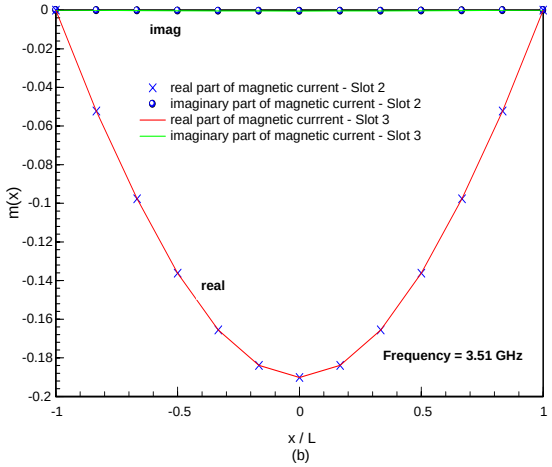

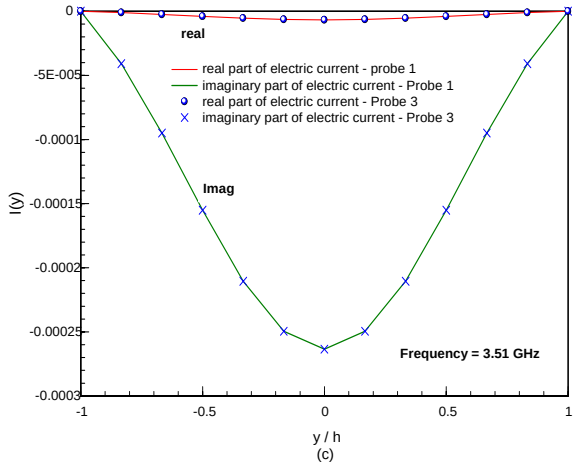

Fig. 5-20. Magnetic currents in the slots and electric currents on the probes due to a 1.0 V excitation on probe 2 (a) Magnetic currents in slot 1 and slot 4. (b) Magnetic currents in slot 2 and slot 3. (c) Electric currents on probe 1 and probe 3.

Structure G Parameters

$2L_1 = 2L_2 = 2L_3 = 2L_4 = 35.0$ mm

$2w = 0.5$ mm

$h_1 = h_2 = h_3 = 28.0$ mm

c = 65.0 mm

$d_1 = d_2 = d_3 = 4.0$ mm

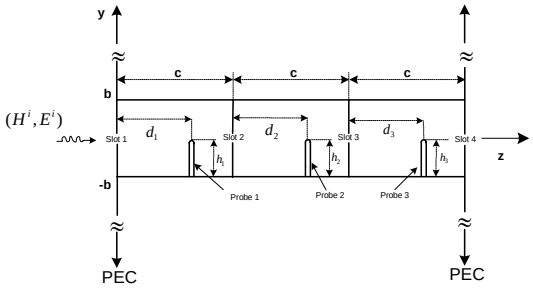

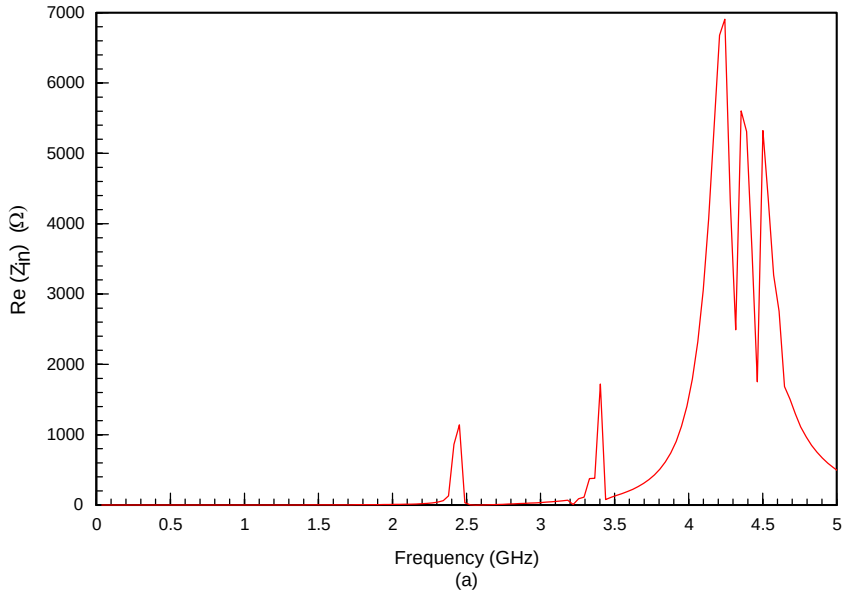

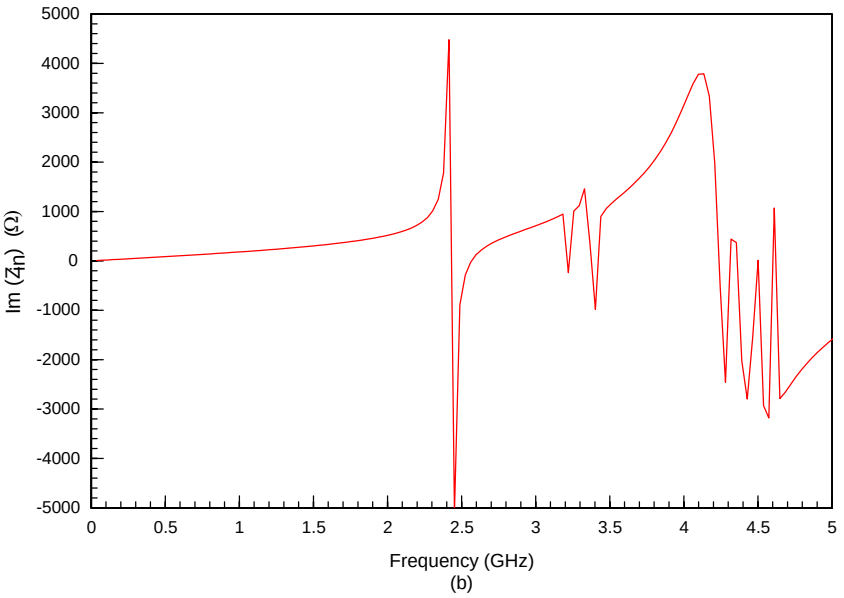

Fig. 5-21. Input impedance at the center of slot 1. (a) Real part of impedance. (b) Imaginary part of impedance.

Structure G Parameters

$2L_1 = 2L_2 = 2L_3 = 2L_4 = 35.0$ mm

$2w = 0.5$ mm

$h_1 = h_2 = h_3 = 28.0$ mm

c = 65.0 mm

$d_1 = d_2 = d_3 = 4.0$ mm

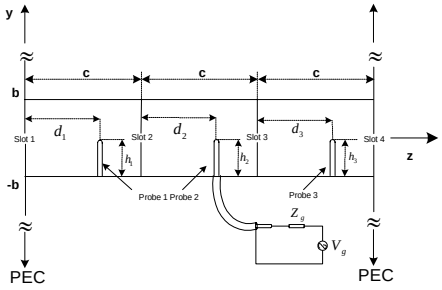

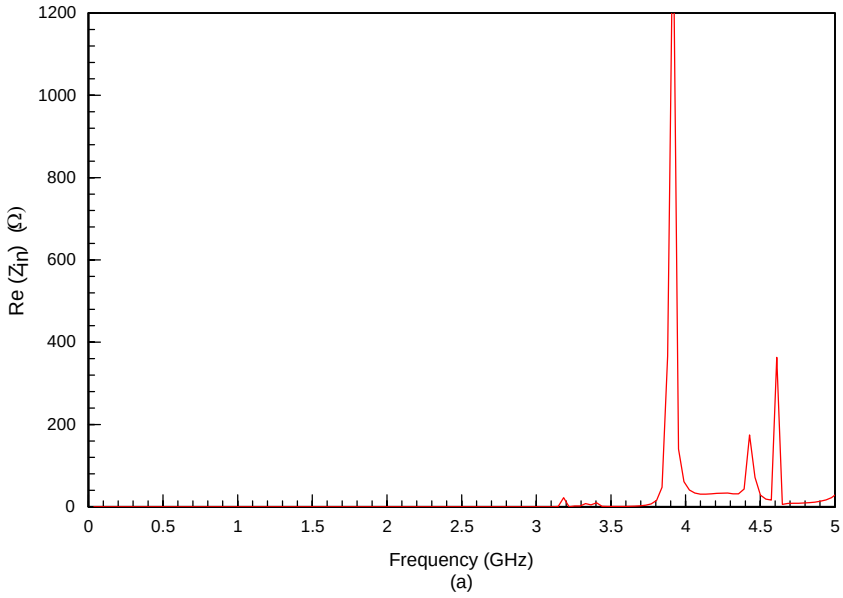

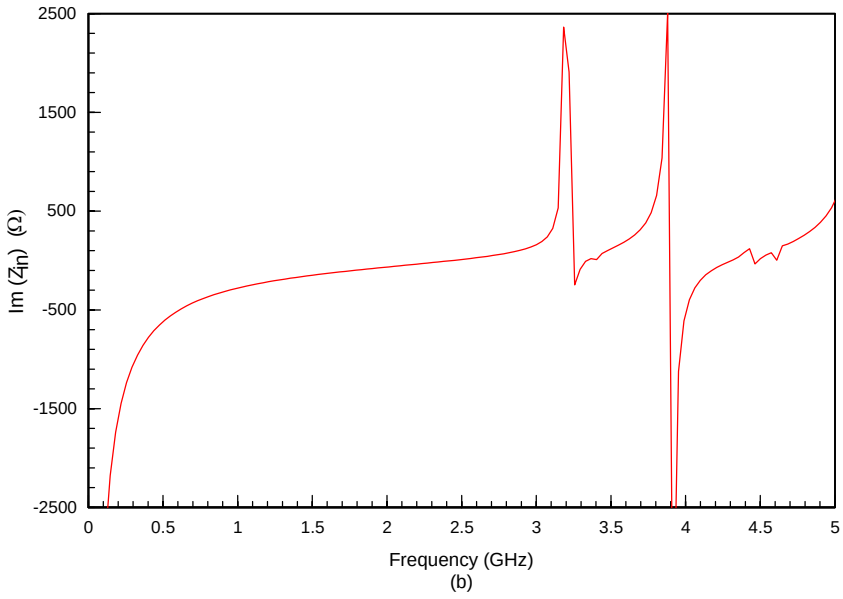

Fig. 5-22. Input impedance at the base of probe 2. (a) Real part of impedance. (b) Imaginary part of impedance.

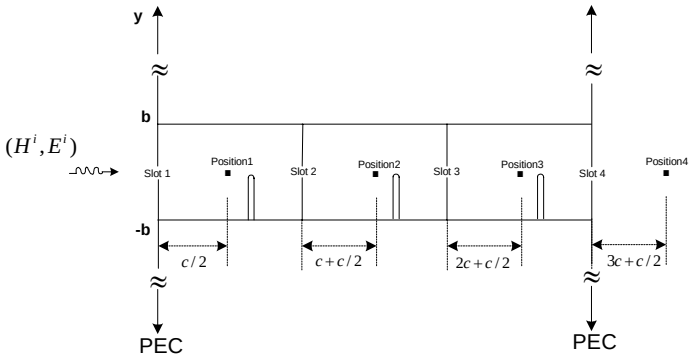

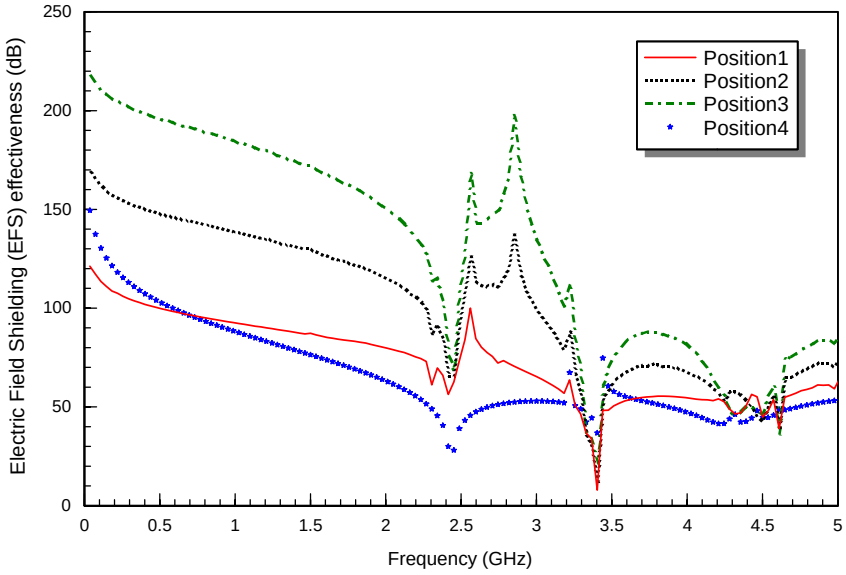

Fig. 5-23. EFS for Structure G.

Structure H Parameters

$2L_1 = 2L_2 = 2L_3 = 2L_4 = 50.0$ mm

$2w = 0.5$ mm

$h_1 = h_2 = h_3 = 36.0$ mm

c = 58.0 mm

$d_1 = d_2 = d_3 = 20.0$ mm

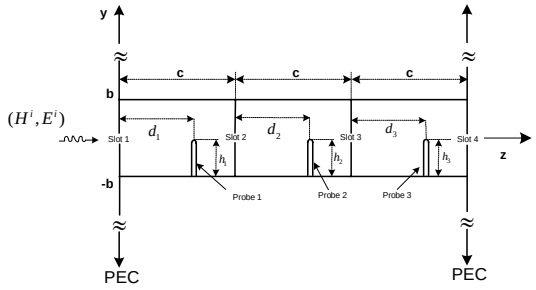

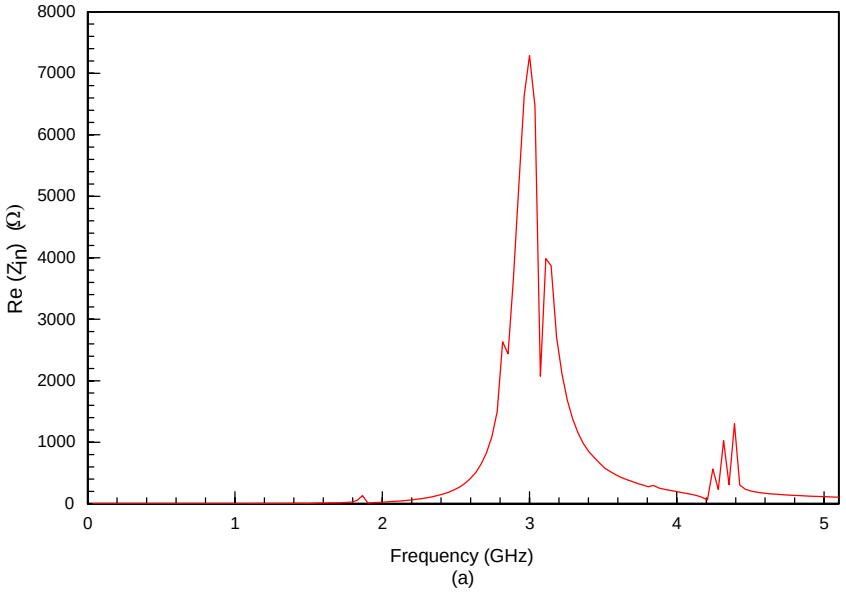

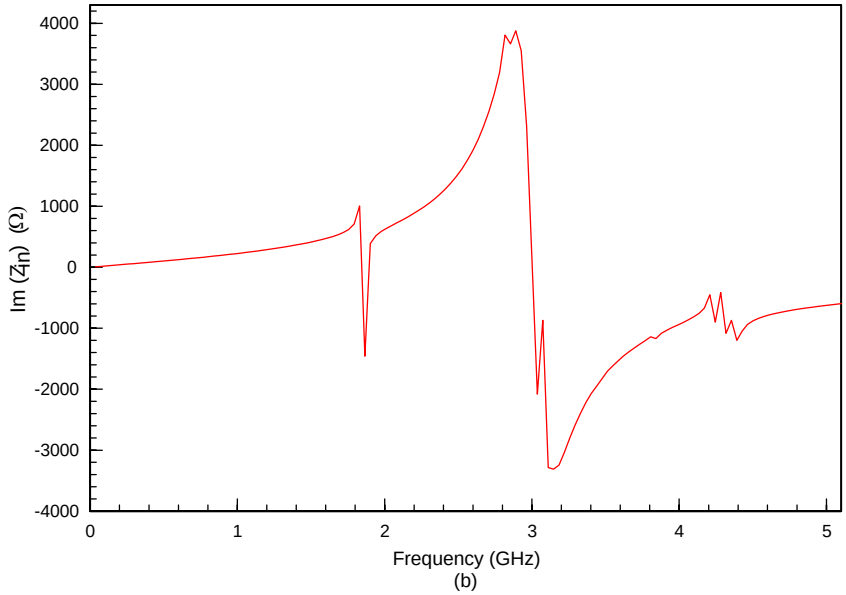

Fig. 5-24. Input impedance at the center of slot 1. (a) Real part of impedance. (b) Imaginary part of impedance.

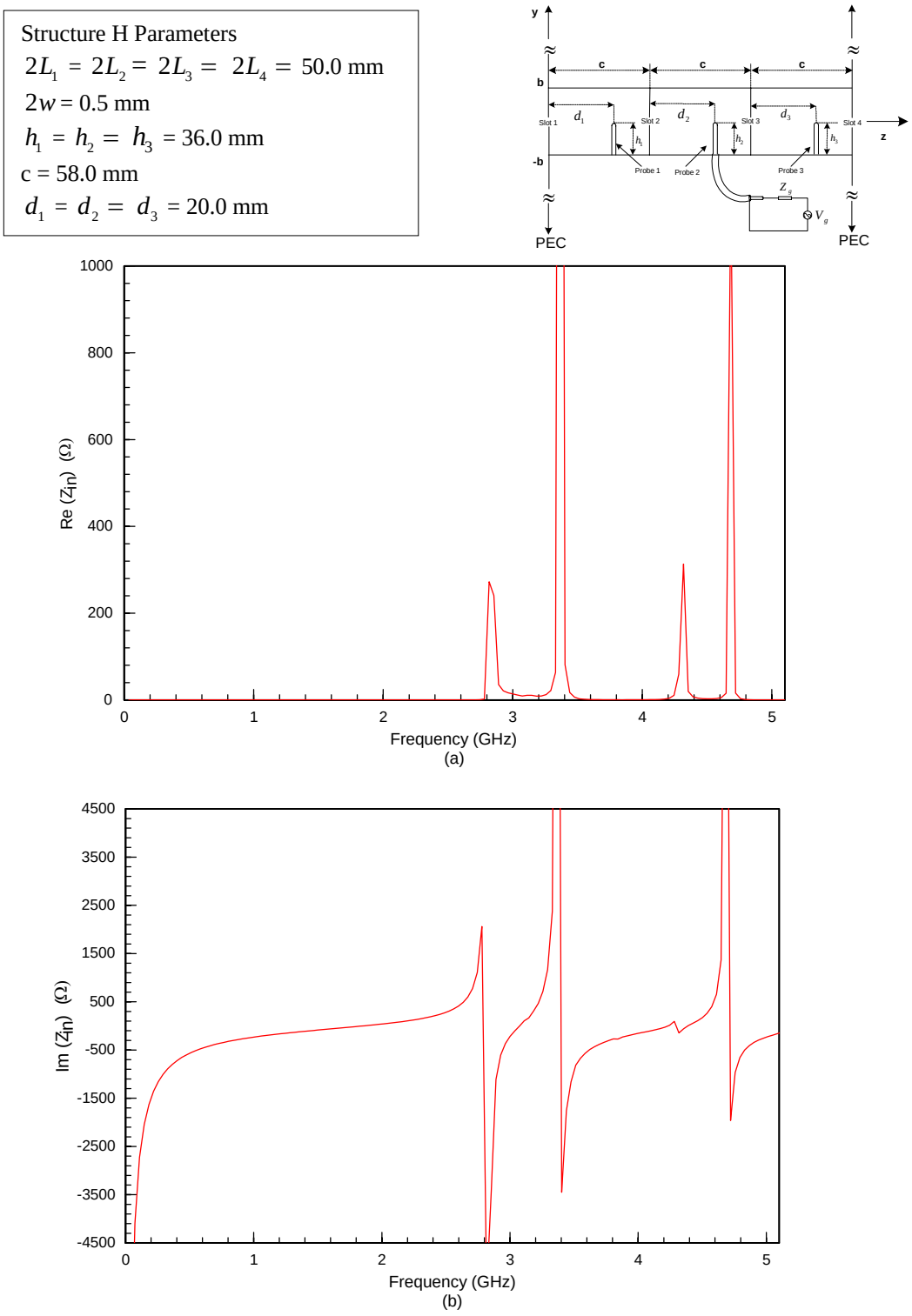

Fig. 5-25. Input impedance at the base of probe 2. (a) Real part of impedance. (b) Imaginary part of impedance.

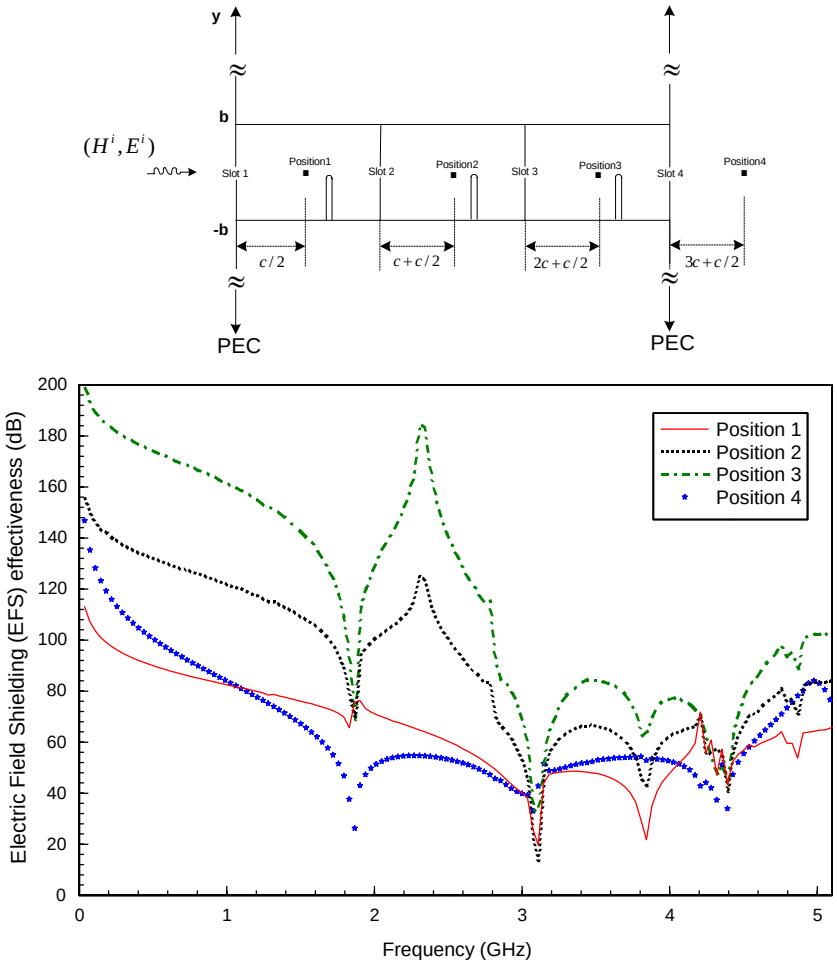

Fig. 5-26. EFS for Structure H.

5. CONCLUSIONS

In this study, an analysis of thin-wire probes inside slotted rectangular cavities has been undertaken. The method of analysis is based on solving the coupled integral equations developed for the electric current on the probe and the equivalent magnetic current in the slot. Input impedance at the center of the slot and at the base of the probe is calculated for single, double, and triply cascaded rectangular cavities. The EFS is calculated at various positions in the cavity to predict the effect of the transmission path/environment on the entering transient signal. The theoretical calculations of resonances are compared to the numerical results and are found to be in good agreement.

REFERENCES

[1] A. Kustepeli, "Analysis and Implementation of the Ewald Method for Waveguide and Cavity Structures," Clemson University, Dissertation, December 1999.

[2] C. M. Butler and K. R. Umashankar, "Electromagnetic Excitation of a Wire Through an Aperture-Perforated Conducting Screen," *IEEE Trans. Antennas Propagat.*, vol. 24, pp. 456-462, July 1976.

[3] D. R. Wilton and C. M. Butler, "Effective Methods for Solving Integral and Integro-Differential Equations," Electromagnetics, vol. 1, pp. 289-308, July-Sept. 1981.

[4] R. Azaro, S. Caorsi, M. Donelli, and G. L. Gragnani, "A Circuital Approach to Evaluating the Electromagnetic Field on Rectangular Apertures Backed by Rectangular Cavities," *IEEE Trans. Microwave Theory and Techniques*, vol. 50, pp.2259-2266, Oct. 2002.

[5] R. E Collin, Field Theory of Guided Waves (IEEE Press, New York, 1991).

[6] E.S. Siah, V. V. Leipa, K. Sertel and J.L. Volakis, "Coupling Studies and Shielding Techniques for Electromagnetic Penetration Through Apertures on Complex Cavities and Vehicular Platforms," *IEEE Trans. Electromagnetic Compatibility*, vol. 45, pp. 245-256, May 2003.